Immunometabolism *cum grano salis*: Investigation into the effect of high salt on early M(LPS) and M(IL4+IL13) macrophage metabolism

Inaugural-Dissertation

to obtain the academic degree

Doctor rerum naturalium (Dr. rer. nat.)

submitted to the

Department of Biology, Chemistry, Pharmacy

of

Freie Universität Berlin

by

Sabrina Yasmin Geisberger

2020

1. Advisor: Prof. Dr. Dominik N. Müller

2. Advisor: Prof. Dr. Oliver Daumke

Date of disputation: 24.06.2020

Abstract

In order to fulfill their function immune cells tightly regulate their central carbon metabolism depending on the microenvironment they encounter. Fully activated *classic* M1 macrophages are known to increase glycolysis and pentose phosphate pathway, while repurposing their tricarboxylic acid (TCA) cycle and electron transport chain (ETC), away from energy production towards the generation of pro-inflammatory mediators. On the other hand, fully-activated *alternative* M2 macrophages highly depend on intact TCA cycling and oxidative phosphorylation (OXPHOS). One important factor of local microenvironment is sodium. Dietary salt, local infection and aging can induce accumulation of high amounts of sodium (without concomitant water retention) in tissues. Immune cells residing or invading such hypertonic saline compartments are differentially regulated and exhibit an altered function. Interestingly, it has been shown that HS boosts macrophage bacterial killing capacity after only 4h, a time point rarely studied in regards to immune cell metabolism.

Based on these data, we hypothesized that high extracellular sodium affects the central carbon metabolism of murine and human mononuclear phagocyte cells. Here we show that upon stimulation, M(LPS) and M(IL4+IL13) macrophages very quickly show an induction of respective pro-inflammatory and anti-inflammatory marker genes, which only partially further increase over time. Furthermore, activation under hypertonic saline (+40mM NaCl, HS) conditions had immediate effects on marker gene expression. Surprisingly, anaerobic glycolysis, the main M1-associated energy source, was not affected by HS at this early stage of activation. We therefore analyzed TCA cycle and OXPHOS by pulsed stable isotope resolved metabolomics (pSIRM) and Seahorse technology. At 3h of activation, glucose- and glutamine-derived label incorporation into the TCA cycle were not affected by HS. Only the conversion of succinate into fumarate was inhibited upon HS in both M(LPS) and M(IL4+IL13). By contrast, Seahorse analysis revealed a significant decrease in basal and maximal oxygen consumption rate (OCR) under HS in both M(LPS) and M(IL4+IL13). This reduction was accompanied by a decrease in ATP

production and mitochondrial membrane potential after only 3h of activation. These data suggest a mitochondrial dysfunction and metabolic uncoupling of TCA cycle and mitochondrial respiration under HS. We could show that HS inhibited ETC complex III and that pharmacologic inhibition of complex III as well as pharmacologic uncoupling mimicked the HS effect on macrophage phenotype. In a translational approach in healthy individuals, we demonstrated that dietary salt intake resulted in a significant increase in plasma sodium. Strikingly, this increase correlated with a decrease in mitochondrial function in peripheral blood-derived monocytes. Taken together, we suggest that HS induces a mitochondrial dysfunction in murine macrophages and human monocytes. This could constitute a novel mechanism by which HS modulates murine and human immune cell function.

Zusammenfassung

Um ihre Funktion zu erfüllen, regulieren Immunzellen ihren zentralen Kohlenstoff-Stoffwechsel in Abhängigkeit des Mikromillieus, auf das sie treffen. Vollständig aktivierte *klassische* M1-Makrophagen steigern ihre Glykolyse und ihren Pentosephosphatweg, während ihr Tricarbonsäure (TCA)-Zyklus und ihre Elektronentransportkette (ETC) weg von Energieproduktion hin zur Erzeugung pro-inflammatorischer Mediatoren umfunktioniert werden. Dagegen sind voll aktivierte *alternative* M2-Makrophagen in hohem Maße von einem intakten TCA-Zyklus und oxidativer Phosphorylierung (OXPHOS) abhängig. Ein wichtiger Faktor lokalen Mikromillieus ist Natrium. Salzhaltige Ernährung, lokale Infektionen und steigendes Alter können zu einer Akkumulation hoher Mengen an Natrium (ohne gleichzeitige Wassereinlagerung) in Geweben führen. Immunzellen, welche sich in solchen hypertonen Salzkompartimenten befinden oder in sie einwandern werden differenziell reguliert und weisen eine veränderte Funktion auf. Interessanterweise wurde gezeigt, dass HS die Bakterienabtötung in Makrophagen bereits nach 4 Stunden verstärkt, ein selten untersuchter Zeitpunkt in Bezug auf Immunzell-Stoffwechsel.

Basierend auf diesen Daten haben wir die Hypothese aufgestellt, dass ein hoher extrazellulärer Natriumgehalt den zentralen Kohlenstoff-Stoffwechsel muriner und humaner mononukleärer Phagozytenzellen beeinflusst. Hier zeigen wir, dass nach Stimulation M(LPS) und M(IL4+IL13)-Makrophagen sehr schnell eine Induktion respektiver pro- und anti-inflammatorischer Markergene aufweisen, welche nur teilweise im Laufe der Zeit weiter zunehmen. Des Weiteren zeigte die Aktivierung unter hypertonen Hochsalz (+40mM NaCl, HS)-Bedingungen unmittelbare Auswirkungen auf die Expression von Makrophagen Markergenen. Überraschenderweise, war die anaerobe Glykolyse, die wichtigste M1-assoziierte Energiequelle, in diesem frühen Stadium der Aktivierung nicht von HS betroffen. Wir analysierten daher den TCA-Zyklus und OXPHOS mittels *pulsed stable isotope-resolved metabolomics* (pSIRM) und Seahorse-Technologie. Nach dreistündiger Aktivierung, waren die Glukose- und

Glutamin-abstammenden Markierungsinkorporationen in den TCA-Zyklus nicht durch HS beeinträchtigt. Lediglich die Umwandlung von Succinat zu Fumarat wurde unter HS in M(LPS) und M(IL4+IL13) inhibiert. Im Gegensatz dazu zeigte die Seahorse-Analyse eine signifikante Abnahme der basalen und maximalen Sauerstoffverbrauchsrate (OCR) unter HS in M(LPS) und M(IL4+IL13). Diese Reduktion ging mit einem Rückgang der ATP-Produktion und des mitochondrialen Membranpotentials nach nur dreistündiger Aktivierung einher. Diese Daten deuten auf eine mitochondriale Dysfunktion und metabolische Entkopplung des TCA-Zyklus und der mitochondrialen Atmung unter HS hin. Wir konnten zeigen, dass HS den ETC-Komplex III hemmte und dass eine pharmakologische Hemmung von Komplex III, sowie eine pharmakologische Entkopplung den HS-Effekt auf den Makrophagen-Phänotyp nachahmten. In einem translationalen Ansatz in gesunden Probanden konnten wir zeigen, dass eine ernährungsbedingte Salzaufnahme zu einem signifikanten Anstieg des Plasmanatriums führte. Eindrucksvollerweise, korrelierte dieser Anstieg mit einer Abnahme der mitochondrialen Funktion in Monozyten peripheren Blutes. Zusammengefasst konnten wir zeigen, dass HS eine mitochondriale Dysfunktion in murinen Makrophagen und humanen Monozyten induziert. Dies könnte ein neuartiger Mechanismus sein, durch welchen HS die Funktion muriner und humaner Immunzellen moduliert.

Acknowledgements

At this point I wish to express my gratitude to all those who have supported me in the completion of my dissertation.

Dominik, you know I was hesitant about starting my PhD without Katrina. But she was right, you're a great mentor. Thank you for throwing me in at the deep, thank you for giving me a lot of freedom in order to learn what science means, thank you for nevertheless guiding me through. I've learnt so much from you and from this phase of my life. I couldn't have asked for more.

To all my lab… It's been four and a half years now since I started sprinkling salt on those intriguing cells. Four and a half years that you were my company through ups and downs. You all supported me establishing new protocols, asking new questions, finding out new caveats, starting all over again. You laughed with me when I didn't want to cry. But equally you were there and cheered with me when I was acting like a gummibear because everything was coming together. You were there during our cooking sessions, having a cocktail in the kitchen or a sangría on the balcony.
Matze, you helped me figuring out where to start and although you might not believe this, but during your last and my first months I would have been lost without you. In honor to you goes the title of this piece of paper. And I will forever look at a watch and think "es ist ja schon fast wieder vier…", no matter what time it is.
Urša, you've been an incredible friend and I really miss you. You said I was your lighthouse in a sea of men. Hearing how you've gone your path and where you're at, I cannot but give you back that compliment.
Hendrik, you started as a quirky med student, unable of pipetting a PCR with your shaking hands. Well you've kept your shaky hands, you're filthy and sometimes a little too confident… but you're the best and you know it :). Thank you for always brainstorming with me, thank you for making me feel competent and clever, thank you for helping me out, even if it meant getting to the lab way too early in the morning.

Following Matze and you, I would like to cite John (19:28): I thirst. I hope we'll stay in touch and maybe, just maybe, really start our AG Geisberger/Bartolomaeus (not the other way around ;)).
Jana, it's been 696 PCRs. Yes, I counted them. And now I know why sometimes you must have thought I was crazy. Thank you for all your help. Thank you for being the kind and honest person you are. You were the best *behind the scenes* colleague I possibly could have had.
Andras, I guess you're not expecting this… but you're my role model. I am not talking about your deep knowledge about basically everything, which you undoubtfully have. I am talking about the responsibility you take in life, your social courage, your environmental consciousness, your kindness, and how you treat people. Hearing your thoughts made me grow as an adult person, outside the lab :)
To all the others, in no particular order, Ralf, Gabi, Jule, Lukasz, Lajos, Ellen, Samuel, Nicola, Nadine, Kristin, Florian, Michaela, Anna, Anika, Franzi, Sarah, Olivia, Ilona, Frau Gerhardt, May-Britt, Jutta, Franziska, Ronja, Jacqui, Nancy, Max, Eve, Meriban, Sina… it was great working with you all and getting to know you!

Furthermore, this thesis would not have been possible without Stefan Kempa and his team. Thank you, Stefan, for all your invaluable support. It's been a great pleasure, the three of us sitting together trying to understand what we now know and trying to imagine what we still don't. Christin and Fardad, you guided me, practically and theoretically, through pSIRM. Thank you both very much!

My thanks also go to Patrick Neubert and Jonathan Jantsch for the interesting meetings, their amazing input and technical support. Also, Thomas Bartolomaeus, thank you for your weekends in the lab and all your great work.
Finally, I also want to thank Prof. Dr. Oliver Daumke from the FU for being my second referee.

To all the people, in- and outside the lab: Thank you!

Contents

I. Introduction

I.1. Macrophages: Activation, Plasticity and Function

Macrophages are a heterogeneous immune cell population, discovered in the 19th century by the Russian zoologist Élie Metchnikoff [1]. They fulfill a plethora of very diverse functions, as they are able to rapidly change their transcriptional, metabolic and functional profile, depending on the microenvironment they encounter [2–8]. Their origin was at first believed to lie in differentiated monocytes that had migrated from the bloodstream into tissue during inflammation. However, it is now established that there are two main subsets: tissue invaded and tissue resident macrophages. While tissue-invading monocyte-derived macrophages mature in the bone marrow by definitive (fetal and adult) hematopoiesis and are terminally differentiated [9], the latter derive from yolk sac and fetal liver during primitive (embryonic) and definitive hematopoiesis and retain their self-renewal potential [10].

The above mentioned adaptational process of macrophages to the local surrounding is referred to as polarization or activation. Due to their plasticity, it is difficult to clearly categorize these activation states. However, based on secreted cytokines, genetic and cell surface markers, and metabolic adaptations they can be classified into two over-simplified extremes: pro-inflammatory *classic* M1 [11, 12] and anti-inflammatory/pro-resolving *alternative* M2 [13, 14] macrophages.
Pro-inflammatory macrophages are activated by microbial products, such as lipopolysaccharide (LPS), or by cytokines secreted by type 1 T helper (T_H-1) lymphocytes, such as interferon gamma (IFNγ) and tumor necrosis factor (TNF). M1 macrophages are able to start and sustain an inflammatory response. They can kill pathogens (by producing high amounts of nitric oxide and reactive oxygen species), secrete pro-inflammatory cytokines (such as TNF, interleukin (IL) 1β, IL2, IL6, and IL12), activate endothelial cells, and recruit other immune cells into the inflamed tissue [4, 8]. Major transcription factors regulating these processes are nuclear factor kappa-light-chain enhancer of

B-cells (NF-κB) [15, 16], signal transducer and activator of transcription (STAT) 1 and 3 [17–19], IFNγ regulatory factor (IRF) 4 and IRF5 [20], hypoxia-inducible factor 1 alpha (HIF1α), and activator protein 1 (AP1) [21] (Figure 1).

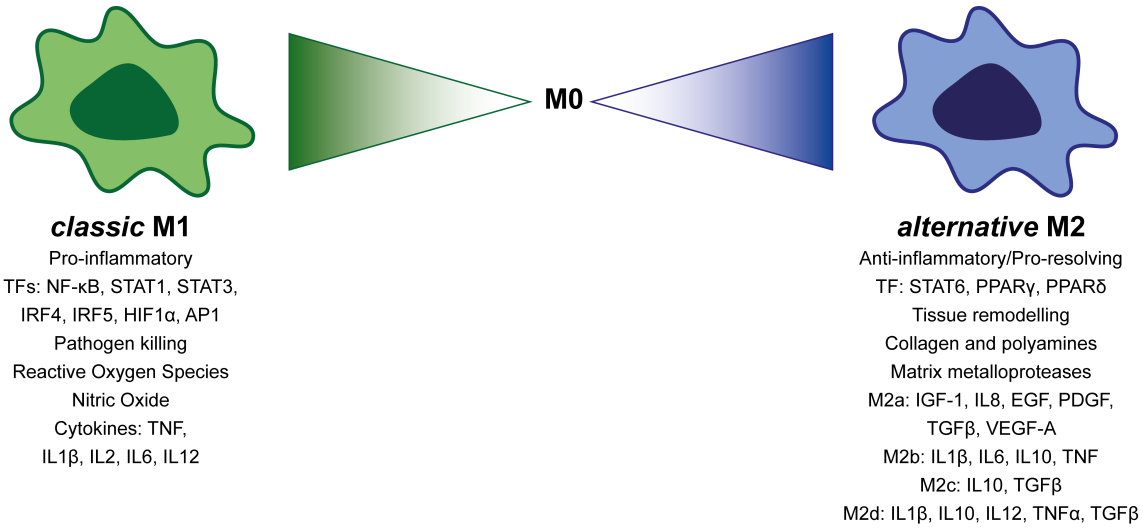

Figure 1: Pictogram of M1 and M2 macrophage activation characteristics. *Classic* M1 macrophages (in green) are pro-inflammatory, kill pathogens, produce reactive oxygen species, nitric oxide, and cytokines such as TNF, IL1β, IL2, IL6, and IL12. Their major transcription factors (TFs) are NF-κB, STAT1, STAT3, IRF4, IRF5, HIF1α, and AP1. *Alternative* M2 macrophages (in blue) are anti-inflammatory/pro-resolving. For tissue remodeling and induction of angiogenesis and lymphangiogenesis, they produce collagen, polyamines, metalloproteases, growth factors such as IGF-1, VEGF-A, EGF, and PDGF, and cytokines such as IL1β, IL6, IL8, IL10, IL12, TGFβ, and TNFα. Their major TFs are STAT6, PPARγ and PPARδ.

Anti-inflammatory M2 macrophages are activated by IL4 and/or IL13, secreted by innate and adaptive immune cells, such as mast cells, basophil granulocytes, and T_H-2 lymphocytes [13, 14]. They are also termed *alternative* or *alternatively activated* macrophages, as in the early 1990s IL4 was described to induce differential effects compared to IFNγ [13]. These cells are characterized by a specific transcriptional profile that enables them to resolve inflammation and induce tissue repair [2]. They express high levels of mannose receptor, produce pro-fibrotic factors (such as transforming growth factor beta (TGFβ) and insulin-like growth factor 1 (IGF-1) [22]), display increased matrix metalloproteases (MMPs) and arginase 1 (ARG1) activity [23], and produce polyamines and collagen, favoring tissue remodeling and wound healing [22]. Furthermore, they induce angiogenesis and lymphangiogenesis with vascular endothelial growth factor

A (VEGF-A), endothelial growth factor (EGF), platelet-derived growth factor (PDGF), and IL8 [24]. In addition to this so-called M2a phenotype induced by IL4 and/or IL13, other stimulants, such as Toll-like receptor (TLR) ligands and immune complexes, glucocorticoids and IL10, as well as IL6 and A2 adenosine receptor (A2R) agonists induce the subsets M2b, M2c and M2d (also called tumor associated macrophages) [25], respectively (Figure 1).

These briefly summarized variants of macrophage activation statuses are the most used in *in vitro* experiments. Although complex enough already, considering the dynamic, multi-dimensional and tissue-specific nature of the local microenvironment paired with the plasticity of macrophages, they are not able to fully describe macrophage activation *in vivo*. However, in order to report exact macrophage cultivation and activation and retract inconsistent and confusing terminology, in 2014 a group of macrophage biologists around Peter Murray suggested new nomenclature guidelines for *in vitro* experiments [26]. Instead of relying on the adjectives *classic* or *altenative* or the terms M1, M2, M2a, M2b, etc. they suggest the exact annotation of all post-differentiation (i.e. after the generation of macrophages with colony stimulating factor (CSF)-1 from murine bone marrow cells or human peripheral blood cluster of differentiation (CD) 14^+ monocytes) stimulants used, e.g. M(IL4) or M(IFNγ). Within this thesis, we followed the same approach, differentiating macrophages from bone marrow cells with CSF-1 and activating these macrophages with LPS or IL4 and IL13 in order to generate M(LPS) and M(IL4+IL13).

I.2. Immunometabolism: Metabolic Reprogramming during Macrophage Activation

In order to fulfill their function, immune cells undergo a so-called metabolic reprogramming, i.e. they tightly regulate their energy, biomass, and “signaling” intermediates producing machinery [2, 7, 27, 28]. The most important metabolic pathways are encom-

passed in the central carbon metabolism (CCM). According to the Kyoto Encyclopedia of Genes and Genomes (KEGG), the central carbon metabolism "is the most basic aspect of life". It includes all enzymatic reactions within glycolysis and gluconeogenesis, pentose phosphate pathway (PPP), tricarboxylic acid (TCA) cycle and oxidative phosphorylation (OXPHOS), amino acid and nucleotide metabolism pathways [29]. Additionally, the CCM includes six known carbon fixation pathways (reductive pentose phosphate cycle (Calvin cycle), reductive citrate cycle, 3-hydroxypropionate bi-cycle, two variants of 4-hydroxybutyrate pathway, and reductive acetyl-coenzyme A (CoA) pathway) as well as some pathways of methane metabolism, all not relevant in animal cells [29].

Glycolysis is one of the simplest and fastest ways to generate energy. Within the cytosol, glucose is converted to pyruvate, generating two molecules of adenosine triphosphate (ATP) per unit of glucose. Besides this relatively inefficient ATP production, during glycolysis other metabolic intermediates are being generated. These are necessary for the synthesis of, for instance, ribose (a precursor of nucleotides), amino acids or fatty acids in order to adapt intracellular processes to new demands. Furthermore, glycolysis supplies the PPP, during which nicotinamide adenine dinucleotide phosphate (NADPH) is produced [2, 30]. NADPH is crucial for M1 macrophages, as it is used by the NADPH oxidase for the production of reactive oxygen species (ROS) to kill pathogens and during fatty acid biosynthesis, required for prostaglandin production [2, 27, 31]. Several pro-inflammatory cytokines, as well as pathogen recognition through pattern recognition receptors (PRRs) converge in the activation of NF-κB [8, 32, 33]. As mentioned above, NF-κB is considered the master regulator of pro-inflammatory macrophage function, regulating the expression of several genes, such as *Tnf*, *Il1b* and *Hif1a* [34][35]. HIF1α in turn regulates the expression of glycolytic enzymes, such as the glucose transporter GLUT1, lactate dehydrogenase (LDHA), and pyruvate dehydrogenase kinase 1 (PDK1) [36–40]. On one hand, the up-regulation of GLUT1 facilitates rapid glucose uptake [28]. On the other hand, LDHA produces lactate from pyruvate and PDK1 inactivates pyruvate dehydrogenase, thereby inhibiting pyruvate entry into the TCA cycle [41]. In order to maintain flux through the glycolytic pathway, during glycolysis reduced nicotinamide adenine dinucleotide (NADH) needs to be oxidized again to NAD^+. M2

macrophages restore NAD^+ at the electron transport chain (ETC) [42], described below. However, OXPHOS is inhibited in M1 macrophages and therefore this conversion of pyruvate into lactate is essential to restore oxidized NAD^+ [2, 27, 28, 31]. The role of glycolysis in M2 macrophages is more controversial. Several studies have shown that glycolysis is active and that its inhibition inhibits M2 activation [20, 43]. Oppositely, there is data showing that M2 macrophages can compensate a loss of glycolytic flux by fueling their TCA cycle with glutamine and acetyl-CoA from fatty acid oxidation [44, 45]. This suggests that these cells are metabolically more flexible, as long as their OXPHOS remains intact.

Besides becoming converted into lactate, pyruvate can also enter the TCA cycle in the mitochondria via its conversion into acetyl-CoA by the pyruvate dehydrogenase (PDHA) or into oxaloacetate by the pyruvate carboxylase (PC) [30]. During the continuous flux via the TCA cycle, NAD^+ and flavin adenine dinucleotide (FAD) are being reduced to NADH and $FADH_2$, respectively [2, 30]. These are then oxidized at the ETC, where under the consumption of oxygen, ATP is being generated [30, 46]. The ETC (Figure 2) is composed of four transmembrane protein complexes, the freely mobile electron transfer carriers ubiquinone and cytochrome c, and the F_1F_O-ATP synthase (also called complex V) [47]. Complex I (CI) is also called NADH-ubiquinone oxidoreductase. As the name describes, CI transfers electrons from reduced NADH to ubiquinone/coenzyme Q (CoQ). The electrons from NADH are first transferred to iron sulfur (FeS) clusters within CI and then CoQ, reducing it to ubiquinol (QH_2). The energy released by this reaction induces the pumping of four protons from the mitochondrial matrix into the mitochondrial intermembrane space (IMS). Complex II (CII) or succinate dehydrogenase, is a component of both the TCA cycle and the ETC. CII catalyzes the oxidation of succinate to fumarate. During this reaction, FAD is reduced to $FADH_2$ after receiving electrons from succinate. These electrons are transferred, similar to CI, to FeS clusters and then to CoQ. Electron transport in CII is not accompanied by the translocation of protons into the IMS. Complex III (CIII) is a coenzyme Q-cytochrome c oxidoreductase and transfers the electrons carried by QH_2 to cytochrome c. Four protons are released during this reaction. Complex IV (CIV), also known as cytochrome c oxidase, transfers

electrons from cytochrome c to the terminal electron acceptor O_2 (reducing it to H_2O). From the eight protons removed from the mitochondrial matrix during this reaction, four are used to form two molecules of H_2O, whereas the other four are pumped across the inner mitochondrial membrane into the IMS. Finally, the protons pass from the IMS to the matrix through the F_O subunit of complex V (CV). The energy created by the proton electrochemical gradient across the inner mitochondrial membrane causes a conformational change in CV, leading to the phosphorylation of adenosine diphosphate (ADP) to ATP [47]. As mentioned above, with only two molecules of ATP per molecule of glucose, the amount of energy released by anaerobic glycolysis is relatively low. During oxidative phosphorylation at CV, however, between thirty and thirty-six molecules of ATP per molecule of glucose are produced [46].

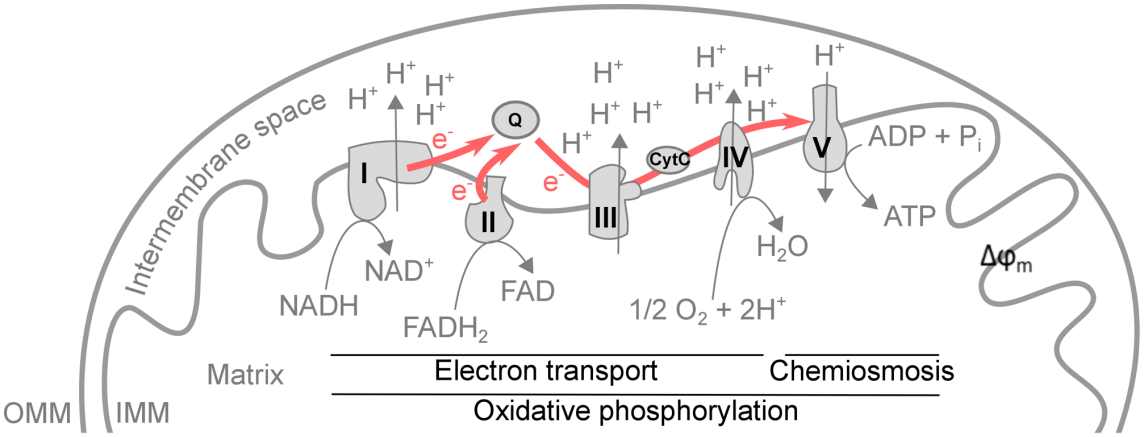

Figure 2: Pictogram of the ETC, composed of four transmembrane protein complexes (I-IV), ubiquinone (Q), cytochrome c (CytC), and the F_1F_O-ATP synthase (V). Complex I (I) transfers electrons from reduced NADH to Q. Complex II (II) oxidizes succinate to fumarate, reducing FAD to $FADH_2$. The latter is then oxidized and electrons (e^-) transfered to Q. Complex III (III) transfers the e^- to CytC. Complex IV (IV) transfers e^- from CytC to oxygen (O_2), reducing it to H_2O. During this e^- transfer, protons (H^+) are beeing pumped into the intermembrane space, creating an electrochemical gradient and membrane potential ($\Delta\Psi_m$) across the inner mitochondrial membrane. These H^+ then pass through complex V (V) in a process called chemiosmosis, leading to the production of ATP. The overall process of electron transfer and chemiosmosis is referred to as oxidative phosphorylation.

M2 macrophages need a functional TCA cycle and OXPHOS (Figure 3 and Figure 4), in order to meet the high energetic demand for the glycosylation of their lectin and mannose receptors [48]. In contrast, M1 macrophages repurpose their TCA cycle and ETC in order to sustain an inflammatory response (Figure 3 and Figure 4) [5, 31, 42, 49, 50]. Within the TCA cycle of a pro-inflammatory macrophage isocitrate dehydrogenase (IDH) and succinate dehydrogenase (SDHA) are inhibited, leading to the accumulation of citrate and succinate, respectively. Again NF-κB plays a central role, leading to the up-regulation of the mitochondrial citrate carrier (CIC) and the ATP-citrate lyase (ACLY) [51–54]. Subsequently, citrate is exported from the mitochondria and broken down into acetyl-CoA and oxaloacetate. Oxaloacetate is then used for the production of nitric oxide, ROS, and prostaglandins. Additionally, via acetyl-CoA, cytosolic citrate positively regulates protein and histone acetylation [51, 55, 56]. Within the TCA cycle citrate can also be metabolized into the bactericidal metabolite itaconate via cis-aconitate by the aconitate decarboxylase 1 (ACOD1), originally called immune-responsive gene 1 protein (IRG1) [51, 57, 58]. Furthermore, itaconate was shown to inhibit SDHA activity, leading to an accumulation of succinate [59]. Accumulating succinate is transported into the cytosol by the solute carrier family 25 member 10 (SLC25A10) [60]. Cytosolic succinate inhibits prolyl hydroxylases and subsequently blocks HIF1α degradation [2, 59, 61]. Besides, succinate can be transported to the extracellular space and bind to G-protein–coupled receptor (GPR) 91. Interestingly, macrophages themselves express GPR91 and sustain a pro-inflammatory response by autocrine signaling [62, 63]. Another metabolic repurposing by pro-inflammatory macrophages was found recently by the group around Luke O'Neill. Under non-inflammatory circumstances, the oxidation of NADH and $FADH_2$ at the ETC is coupled, as stated before, to the production of ATP. However, succinate can still be oxidized into fumarate by the SDHA in CII of the ETC without subsequent ATP production [64]. In this case, the electrons released during this reaction do not follow the so-called *forward electron flow* to CIII, but rather travel to CI in a process named *reverse electron flow* (RET). This associates to a significant release of ROS. It is thus believed, that M1 macrophages can repurpose their mitochondria, away from ATP and towards ROS production [2, 42, 64].

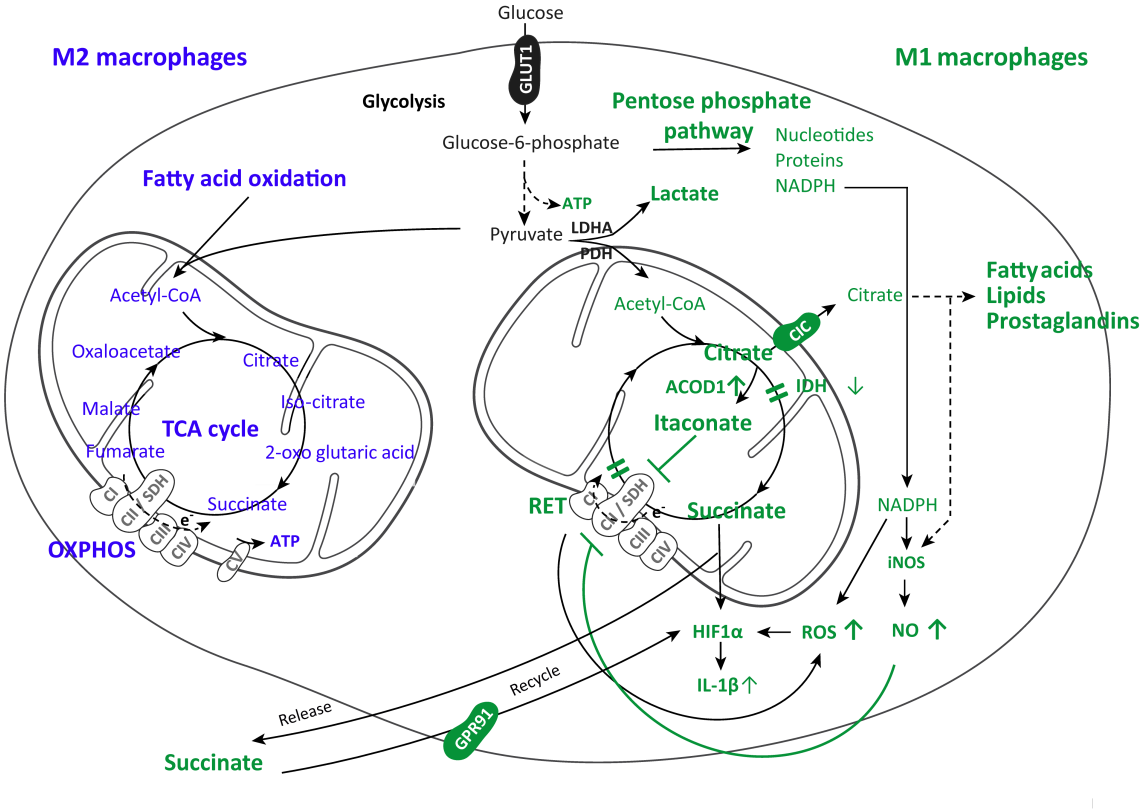

Figure 3: Pictogram of central carbon metabolism in M1 and M2 macrophages, adapted from [27]. M2 macrophages (in blue) have an intact TCA cycle, wich they replenish with glucose and FAO, resulting in increased OXPHOS and sustained ATP production. M1 macrophages (in green) display high glycolytic rates (for ATP and lactate production), an increased PPP (for NADPH, ROS, and NO production), and a disturbed TCA cycle. The first break at IDH results in the accumulation of citrate, used for fatty acid synthesis, membrane biosynthesis, and prostaglandin production. It also supports NO production and generates itaconate, inhibiting SDH activity. This second break at SDH leads to an accumulation of succinate. Succinate stabilizes HIF1α, and its ATP-independent oxidation provokes ROS-inducing RET. The succinate receptor GPR91 senses extracellular succinate released by inflammatory macrophages and induces a feedforward loop of inflammatory macrophage activation.

With respect to M2 macrophages, ACLY is also up-regulated (although by the protein kinase B (PKB or Akt)/ mechanistic target of Rapamycin complex 1 (mTORC1) pathway), leading to histone acetylation and induction of several M2 genes, such as *Mgl2*, *Arg1* and *Retnla1* [65]. Nevertheless, as already mentioned above, the main metabolic pathway in M2 macrophages is the highly efficient mitochondrial respiration. These cells need a functional TCA cycle, which they fuel - at a fully activated state – with the acetyl-CoA derived from fatty acid oxidation (FAO) [44]. During this process, besides acetyl-CoA, NADH and $FADH_2$ are being produced. One classic inducer of FAO used in *in vitro* experiments is palmitate, which e.g. leads to the production of more than one

hundred molecules of ATP per molecule of palmitate [42].

Upon IL4 and/or IL13 binding to their respective receptors, receptor-bound Janus kinases (JAKs) phosphorylate signal transducer and activator of transcription 6 (STAT6) [8, 66–69]. STAT6 is, opposed to NF-κB, the master regulator of M2 activation. Additionally, activation of the nuclear receptors peroxisome proliferator-activated receptor (PPAR) γ and δ is necessary for the full implementation of the M2 program [70]. In response to STAT6 and PPARδ activation peroxisome proliferator-activated receptor gamma coactivator 1-beta (PPARGC1B or PGC-1β) and AMP-activated protein kinase (AMPK) boost FAO [42]. However, there is controversial data about the effect of FAO inhibition with the carnitine palmitoyltransferase 1 (CPT1) inhibitor etomoxir on M2 activation. The group around Edward and Erika Pearce demonstrated a reduced M2 activation under etomoxir treatment [44]. In contrast, at an earlier time point during activation, etomoxir seems to have no effect on the expression of *Arg1*, *Retnla1*, *Chil3* or *Mrc1* [43]. This pinpoints to a dynamic adaption of cellular metabolism during the course of activation, where TCA cycle is at first fueled by the oxidation of glucose and FAO is required at a later stage for the sustained induction and survival of M2 macrophages (Figure 4).

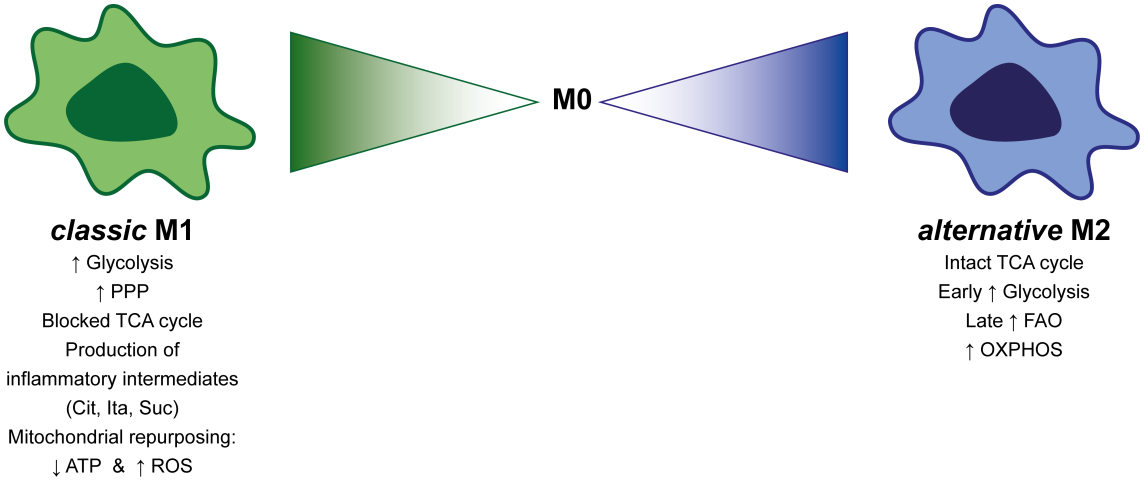

Figure 4: Pictogram of M1 and M2 macrophage metabolic features. M1 macrophages (in green) display high rates of glycolysis and PPP. Furthermore they repurpose their TCA cycle and ETC in order to produce pro-inflammatory intermediates and ROS. M2 macrophages (in blue) have an intact TCA cycle, increased glycolysis and FAO, resulting in increased OXPHOS and sustained ATP production.

I.3. Microenvironment: High Salt and Immune Cells

One important factor of local microenvironment is sodium. With 140 mM sodium is the major extracellular cation and exerts osmotic pressure [71]. Changes in its concentration alter this osmotic pressure, leading to swelling or shrinking of surrounding cells and subsequently altering cellular function [72]. Thus, the accepted textbook theory in electrolyte and fluid physiology was that changes in extracellular sodium concentration must be prevented and that cells are embedded in interstitial fluid compartments of constant tonicity [73]. However, long-term sodium balance studies and sodium magnetic resonance imaging (both in humans) show that sodium can indeed accumulate in tissues without compelling commensurate water retention [74–81]. The group around Jens Titze demonstrated that 24 h sodium excretion rarely matched the same day's sodium intake and that, when sodium intake was fixed over a period of several weeks and months, sodium excretion fluctuated considerably from day to day [74]. Furthermore, Titze showed that sodium was retained or excreted without changes in body weight and body fluid content [75]. Much later, sodium magnetic resonance imaging (^{23}Na-MRI) allowed the visualization of sodium content in tissues. So far, brain [76, 77], muscle [78, 79] and skin [79, 80] have been identified to accumulate sodium independently of water, which was estimated with conventional MRI. This sodium retention was greatly dependent on age and sex [78, 79]. Interestingly, disease [79, 81] and local inflammation [80] are further variants that induce hypertonic sodium retention in these tissues (Figure 5).

Immune cells residing or invading such hypertonic saline compartments are differentially regulated and exhibit an altered function. Pro-inflammatory IL17A-producing T_H-17 cells cultivated under high salt conditions displayed a stronger activation compared to normal salt control cells, up-regulating pro-inflammatory cytokines and worsening the outcome of experimental autoimmune encephalomyelitis (an animal model of multiple sclerosis) [82] as well as bone density in an osteoporosis animal model [83]. Interestingly, also T_H-2 cells are shown to be boosted under high salt conditions,

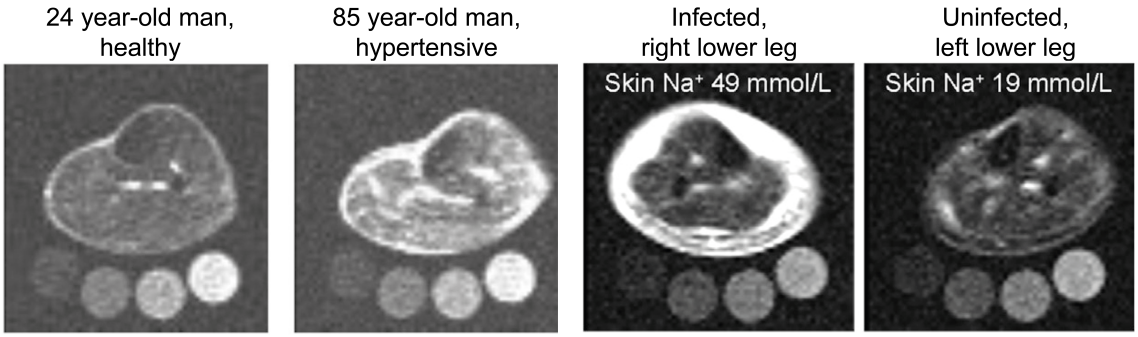

(a) Representative ^{23}Na-MRI from the lower leg of a 24-year old normotensive and a 85-year old hypertensive man.

(b) Representative ^{23}Na-MRI from a bacterially infected and contralateral uninfected lower leg of a male patient.

Figure 5: Representative ^{23}Na-MRI adapted from [79] and [80]

displaying increased production of IL4 and IL13. Additionally, T_H-2 program was induced by high salt even in the absence of T_H-2-polarizing cytokines [84]. In contrast, FOXP3$^+$ regulatory T cells cultivated under high salt conditions displayed an impaired suppressive function against CD4$^+$ naive effector T cells with increased secretion of pro-inflammatory IFNγ [85]. Similar findings could be found in the innate immune system. Activation of pro-inflammatory M(LPS) macrophages under high sodium chloride concentrations resulted in an elevated nitric oxide production and improved bacterial and parasitic killing capacity [80, 86]. Anti-inflammatory M(IL4+IL13) macrophages, on the other hand, displayed an inhibited expression of M2 marker genes and reduced T cell suppressive capacity. Furthermore, mice on a high salt diet exhibited worsened wound healing when compared to the normal fed controls [87]. One suggested mechanism for this differential regulation upon high salt is the up-regulation of the osmoprotective transcription factor tonicity enhancer binding protein (TonEBP or NFAT5) and downstream signaling via the serum/glucocorticoid-regulated kinase 1 (SGK1). Gene silencing or chemical inhibition of SGK1 or NFAT5 abrogated the high salt-induced effect in T_H-17 [82] and M(LPS) [80]. However, both SGK1 and NFAT5 were barely induced in M(IL4+IL13) under high salt conditions. Furthermore, the changes seen in M(LPS) killing as well as M(IL4+IL13) gene expression were independent of tonicity, as shown by equivalent, non-ionic hypertonic treatment with urea or mannitol [87].

I.4. Hypothesis and Aims

As described above, fully activated classic M1 macrophages are known to increase glycolysis and pentose phosphate pathway, while repurposing their mitochondria from ATP to ROS production. In contrast, late-phase alternative M2 macrophages highly depend on fatty acid oxidation and oxidative phosphorylation. These, however, are data from late time points of macrophage activation (24h post-activation), where a full pro- or anti-inflammatory phenotype is adopted. There is hardly any data available covering the early metabolic pathways engaged during macrophage polarization. Interestingly, the functional impact of a high salt treatment is already present much earlier [86]. Neubert *et al.* showed increased bacterial killing capacity after only 4h of activation under high salt conditions. At this early time point the proteome has not fully shifted yet. We thus hypothesize that sodium chloride has immediate effects on metabolic pathways essential for early macrophage activation. We ask if and how the early metabolic commitment is modulated by high salt treatment in both M(LPS) and M(IL4+IL13) macrophages.

To test our hypothesis we generated murine bone marrow-derived macrophages and activated them towards M(LPS) or M(IL4+IL13) in the presence or absence of additional 40 mM sodium chloride in the culture medium for different time points. Subsequently we adressed several major research questions:

- gene expression analyses of M1 and M2 marker genes in order to dissect the impact of high salt on early and late macrophage activation.

- metabolic tracing of glucose and glutamine breakdown via pulsed stable isotope-resolved metabolomics, in order to analyze glycolytic and TCA cycle flux under normal and high salt conditions, as well as gene expression analysis of key metabolic enzymes, in order to detect any transcriptional regulation by high salt.

- evaluation of real-time mitochondrial oxygen consumption rate, NAD/NADH and ATP statuses, as well as mitochondrial membrane potential and ETC complex activities in order to fully evaluate mitochondrial function.

- assessment of mitochondrial morphology by transmission electron microscopy to detect any structural impact of a high salt treatment.

- selective pharmacologic treatment of discovered pathways affected by high salt in order to reproduce the high salt effect in M(LPS) and M(IL4+IL13).

Technically, the metabolomic analyses were performed in cooperation with the group of Dr. Stefan Kempa at the proteomics/metabolomics platform from the Berlin Institute for Medical Systems Biology (BIMSB). Furthermore, the mitochondrial morphology was analysed together with Prof. Dr. Thomas Bartolomaeus from the Institute for Evolutionary Biology and Ecology (IEZ) at the university of Bonn and macrophage killing capacity was assessed in cooperation with Prof. Dr. Jonathan Jantsch from the Institute for Microbiology and Hygiene at the University of Regensburg (IMHR).

Lastly, in order to translate our findings into humans, we:

- isolated blood-derived monocytes from healthy volunteers and studied the impact of high salt treatment on mitochondrial function.

- analysed mitochondrial function in blood-derived monocytes from a salt-intervention study (previously performed in our laboratory by Dr. Nicola Wilck), in order to evaluate the effect of a high salt diet on monocyte metabolism.

II. Materials

II.1. Bone Marrow-Derived Macrophages

Primary macrophages were generated from the bone marrow of male, 9 to 12 week old, wild type C57BL/6J mice (purchased from Harlan Laboratories and bred at the animal facility from the Max-Delbrück Center Berlin). Mice were housed under standard light-dark cycled (12h/12h) and specific pathogen free conditions. They were fed a normal chow diet (V1124-300 from Ssniff® Spezialdiäten GmbH) and tap water *ad libitum*.

II.2. Cell Lines

Cell line	Cell type	Provider
L929	NCTC clone 929 (strain C3H/An) derived from murine subcutaneous areolar and adipose connective tissue	ATCC® by LGC Standards

II.3. Blood-Derived Monocytes

Blood-derived monocytes were isolated out of peripheral blood mononucleated cells as described below (see III.3 and III.4). Whole blood was drawn by Dr. Andras Balogh and Dr. Hendrik Bartolomaeus from healthy volunteers in accordance with the ethical standards of the institutional review board of the Charité University Medicine Berlin (ethical approval EA2/046/17) and written informed consent was obtained from all participants before study entry. Subjects were recruited locally from the Campus Berlin-Buch of the Charité University Medicine Berlin and from the Max-Delbrück-Center for Molecular Medicine.

The salt-intervention study re-analysed within this thesis was previously performed in our laboratory by Dr. Nicola Wilck in cooperation with Dr. Michael Boschmann and Dr. Anja Mähler from the Experimental & Clinical Research Center Berlin-Buch. The institutional review board of Charité University Medicine Berlin approved the study (EA1/138/15) and written informed consent was obtained from all participants before study entry. The study was conducted in accordance with the Declaration of Helsinki in its currently applicable version, the guidelines of the International Conference on Harmonization of Good Clinical Practice (ICH-GCP) and applicable German laws. The study was registered at ClinicalTrials.gov (NCT02509962).

II.4. Cell Culture

Material	**Manufacturer**	**Catalogue ID**
Adult horse serum	Cell Concepts	S-HEU03-I
Beta-mercaptoethanol	Sigma® by Merck	M3148
DMEM, high glucose, with sodium pyruvate and L-glutamine	Gibco™ by Thermo Fisher Scientific	41966-029
DMEM, without glucose and sodium pyruvate, with L-glutamine	Gibco™ by Thermo Fisher Scientific	11966-025
DMEM, without glucose, L-glutamine and sodium pyruvate	Gibco™ by Thermo Fisher Scientific	A14430-01
DMSO	Sigma® by Merck	D4540
Fetal bovine serum (FBS)	Biochrom by Merck	S0615
Glucose (D(+)-)	Carl Roth®	X997.2
Glucose (U-13C6 D-)	Cambridge Isotope Laboratories	CLM-1396-PK

Glutamine (L-)	Gibco™ by Thermo Fisher Scientific	25030-081
Glutamine (13C5 L-)	Cambridge Isotope Laboratories	CLM-1822-H-PK
HEPES 1M	Gibco™ by Thermo Fisher Scientific	15630-056
LPS from E. coli o111:B4	Sigma® by Merck	L3024
Mouse IL-4	R&D Systems™ by bio-techne®	404-ML-010
Mouse IL-13	Invitrogen™ by Thermo Fisher Scientific	PMC0134
Non-essential amino acids	Sigma® by Merck	M7145
PBS without $CaCl_2$ and $MgCl_2$	Sigma® by Merck	D8537
Penicillin/ Streptomycin	Gibco™ by Thermo Fisher Scientific	15140-122
Seahorse XF base medium	Agilent	102363-100
Sodium chloride (NaCl)	Carl Roth®	9265.1
Sodium pyruvate (100 mM)	Gibco™ by Thermo Fisher Scientific	11360070
Trypan blue 0.5%	PromoCell	PK-CA902-1209
Trypsin/ EDTA	Sigma® by Merck	59417C

II.5. Kits

Kit	Manufacturer	Catalogue ID
ATPlite Luminescence Assay System	PerkinElmer	6016941
Complex I Enzyme Activity Microplate Assay Kit	Abcam	ab109721
EMbed-812 Kit	Science Services	E14121
High Capacity cDNA Reverse Transcription Kit	Applied Biosystems™ by Thermo Fisher Scientific	4368813
Mitochondria Isolation Kit	Miltenyi Biotec	130-096-946
MitoTox Complex II + III OXPHOS Activity Assay Kit	Abcam	ab109905
NAD/NADH Assay Kit (Colorimetric)	Abcam	ab65348
Pan Monocyte Isolation Kit human	Miltenyi Biotec	130-096-537
RNase-free DNase Set	Qiagen	79254
RNeasy® Mini Kit	Qiagen	74106
Seahorse XFe96 FluxPak	Agilent	102416-100

II.6. Primers and Probes for qPCR

All primers (forward *F* and reverse *R*) and probes (*P*) for qPCR were designed to be species specific for mouse and purchased from BioTeZ Berlin-Buch GmbH.

Gene	Sequence (5′ - 3′)	Encoding
18S	F: ACATCCAAGGAAGGCAGCAG R: TTTTCGTCACTACCTCCCCG P: CGCGCAAATTACCCACTCCCGAC	18 Svedberg units ribosomal RNA
Arg1	F: CCACAGTCTGGCAGTTGGAA R: GCATCCACCCAAATGACACA P: TGGCCACGCCAGGGTCCAC	Arginase 1
Ccl5	F: GCAGTCGTGTTTGTCACTCGAA R: GATGTATTCTTGAACCCACTTCTTCTC P: AACCGCCAAGTGTGTGCCAACCC	C-C motif chemokine ligand 5
Chil3	F: TCCTACTGGAAGGACCATGGAGCA R: TCCTGGTGGGCCAGTACTAATTGT	Chitinase-like protein 3
Cox2	F: CAGGTCATTGGTGGAGAGGTGTA R: GGATGTGAGGAGGGTAGATCATCT P: CCCCCCACAGTCAAAGACACTCAGGT	Cyclooxygenase 2
Irf4	F: CGGGCAAGCAGGACTACAA R: TCGGAACTTGCCTTTAAACAATG	Interferon regulatory factor 4
Irf5	F: CTTGGCCCATGGCTCCTGCC R: AGCAACCGGGCTGCAACAGG	Interferon regulatory factor 5
Ldha	F: ATGAAGGACTTGGCGGATGA R: ATCTCGCCCTTGAGTTTGTCTT	Lactate dehydrogenase
Mgl2	F: GAGACAGACTTGAAGGCCTTGAC R: GCCACTTCCGAGCCATTG	Macrophage galactose N-acetyl-galactosamine specific lectin 2

Mrc1	F: AATACCTTGAACCCATTTATCATTCC R: GCATAGGGCCACCACTGATT P: CGATGTGCCTACCGGCTGCCC	Mannose receptor C-type 1
Nlrp3	F: GGAGTCTAGCAGACCTGATTGTCA R: GGCTTGCGCAGGATCTTG P: CTGCTGGCCTGACCCAAACCCA	NLR Family Pyrin Domain Containing 3
Nos2	F: GGGCAGCCTGTGAGACCTT R: TGCATTGGAAGTGAAGCGTTT P: TCCGAAGCAAACATCACATTCAGATCCC	Nitric oxide synthase 2
Pcx	F: TTGCCAAGCAGGTAGGCTAT R: TGGATCTGAGCATGGACCAG	Pyruvate carboxylase
Pdha1	F: ATGGTGCTGCTAATCAGGGT R: CATGCCATAGCGGTTGTTCT	Pyruvate dehydrogenase E1α1
Retnla1	F: CGTGGAGAATAAGGTCAAGGAACT R: CACTAGTGCAAGAGAGAGTCTTCGTT P: TTGCCAATCCAGCTAACTATCCCTC-CACTG	Resistin like α
Slamf1	F: TGGCTAATGGATCCCAAAGGA R: CCATCACACCTCCACCTGTT	Signaling lymphocytic activation molecule family member 1
Sdha	F: TGCCTTGCCAGGACTTAGAA R: GCAACAGGTGCGTATCTCTC	Succinate dehydrogenase complex flavoprotein subunit A
Tnf	F: GGTCCCCAAAGGGATGAGAA R: TGAGGGTCTGGGCCATAGAA P: TTCCCAAATGGCCTCCCTCTCATCA	Tumor necrosis factor

II.7. Antibodies and Probes for Flow Cytometry

Antigen	Conjugation	Manufacturer	Catalogue ID
CD11b (anti-mouse)	Fluorescein isothiocyanate (FITC)	BD Biosciences	553310
CD14 (anti-human)	Phycoerythrin (PE)-Vio 770	Miltenyi biotec	130-110-579
CD16 (anti-human)	Fluorescein isothiocyanate (FITC)	Miltenyi biotec	130-106-703
F4/80 (anti-mouse)	Pacific Blue (PB)	eBioscience by Thermo Fisher Scientific	48-4801-80

Probe	Manufacturer	Catalogue ID
bisBenzimide H 33342 trihydrochloride (Hoechst)	Sigma® by Merck	B2261
LIVE/DEAD™ Fixable Aqua Dead Cell Stain Kit for 405nm excitation	Invitrogen™ by Thermo Fisher Scientific	L34966
MitoTracker™ Green FM	Invitrogen™ by Thermo Fisher Scientific	M7514
Tetramethylrhodamine ethyl ester perchlorate (TMRE)	Invitrogen™ by Thermo Fisher Scientific	T669

II.8. Chemicals and Reagents

Chemical	Manufacturer	Catalogue ID
ADP	Sigma® by Merck	A5285
Antimycin A	Sigma® by Merck	A8674
BD FACSClean	BD Biosciences	340345
BD FACSFlow	BD Biosciences	342003
BD FACSRinse	BD Biosciences	340346
BD FACSSheath solution	BD Biosciences	336911
BD FACSShutdown solution	BD Biosciences	334224
Carbonyl cyanide 4-(trifluoromethoxy)phenylhydrazone (FCCP)	Sigma® by Merck	C2920
Chloroform	Merck	102445
Complete protease inhibitor cocktail	Roche Diagnostics GmbH	1836145
Ethylenediaminetetraacetic acid (EDTA)	Sigma® by Merck	E-4884
Fast SYBR™ Green Master Mix	Applied Biosystems™ by Thermo Fisher Scientific	4385614
Glutaraldehyde	Sigma® by Merck	G5882
Isofluran CP	cp-pharma	1214
Lead citrate	Science Services	E17810
Malic acid	Sigma® by Merck	46940-U
Methanol	Carl Roth®	HN41.2
Methoxyamine hydrochloride	Sigma® by Merck	M6524
N^5,N^6-bis(2-fluorophenyl)-[1,2,5]oxadiazolo[3,4-b]pyrazine-5,6-diamine (BAM15)	Sigma® by Merck	SML1760-5MG

N-methyl-N-trimethylsilyl-trifluoroacetamide (MSTFA)	Macherey-Nagel	701270.201
Oligomycin A	Sigma® by Merck	75351
Osmium tetroxide	Sigma® by Merck	201030
Phenylmethylsulfonyl fluoride (PMSF)	Sigma® by Merck	P7626
Phosphatase inhibitory cocktail	Sigma® by Merck	P0044
Potassium 2-oxo-glutaric acid	Sigma® by Merck	K2000
Potassium carbonate	Sigma® by Merck	P5833
Potassium chloride	Carl Roth®	6781.1
Potassium citrate	Sigma® by Merck	1548225
Potassium lactate	Sigma® by Merck	60389
Potassium phosphate	Sigma® by Merck	P5629
Pyridine	Carl Roth®	9729.3
QIAzol Lysis Reagent	Qiagen	79306
Rotenone	Sigma® by Merck	R8875
Sodium chloride	Carl Roth®	9265.1
Sodium Dodecylsulfate (SDS)	Sigma® by Merck	L4509
Sodium fumarate	Sigma® by Merck	8205840100
Sodium succinate	Sigma® by Merck	W327700
Sucrose	Sigma® by Merck	S0389
TaqMan fast universal PCR master mix 2x	Applied Biosystems™ by Thermo Fisher Scientific	4367846
Trans-Cinnamic acid	Sigma® by Merck	133760
Tris	Carl Roth®	4855.2
Triton X-100	Sigma® by Merck	T9284
Uranyl acetate	Science Services	E22400
Water	Sigma® by Merck	95284

II.9. Consumables

Consumable	Manufacturer	Catalogue ID
Click counter	InFactory	PE-5653-919
Crimp neck glass vial ND11, wide opening, conical	Th. Geyer	7632401
Crimp seals ND11, aluminium	Th. Geyer	7618903
Filter tips 0.1-10 µl	Sarstedt	70.1130.210
Filter tips 100-1000 µl	Sarstedt	70.762.211
Filter tips 2-200 µl	Sarstedt	70.760.211
Flow cytometry tubes 5 mL, 75x12 mm, PS	Sarstedt	55.1579
Microcentrifuge tubes 1.5ml	Carl Roth®	4182.1
Microcentrifuge tubes 2ml	Carl Roth®	NA16.1
Microtubes 0.5ml	Carl Roth®	7060.1
Microtubes for PCR 0.2ml	Carl Roth®	XT87.1
Neubauer cell counting chamber 0.100 mm depth 0.0025 mm^2	VWR™	631-0696
Optical adhesive film (for qPCR)	G Kisker Biotech	G060/UC-RT
Quali-PCR plates	G Kisker Biotech	G060/H/1E-7500
Sterile cell culture dishes 100x20mm	Greiner Bio-One	664160
Sterile cell culture flask T25	Sarstedt	83.3910.002
Sterile cell culture flask T75	Sarstedt	83.3911.002
Sterile cell culture flask T175	Sarstedt	83.3912.002
Sterile cell culture plate 6 well	Greiner Bio-One	657160
Sterile cell culture plate 12 well	Greiner Bio-One	665180
Sterile cell culture plate 96 well (F-bottom)	Greiner Bio-One	655180
Sterile cell scraper M	TPP®	99003

Sterile cell spatula	TPP®	99010
Sterile disposable pasteur pipettes	Carl Roth®	EA66.1
Sterile filter	VWR	514-0342
Sterile needle 23G x 1” Nr. 16	Terumo Agani	NN-2325R
Sterile serological pipette 5 mL	Sarstedt	86.1253.001
Sterile serological pipette 10 mL	Sarstedt	86.1254.001
Sterile serological pipette 25 mL	Sarstedt	86.1685.001
Sterile solution basin 50mL	Carl Roth®	EKX0.1
Sterile syringe 10ml	B Braun Melsungen	4606108V
Sterile syringe 20ml	B. Braun Melsungen	4606205V
Sterile syringe 50ml	BD Plastipak	300865
Teflon film	DuPont/American Durafilm	FT FEP 100C
Tubes 15ml (sterile)	Greiner Bio-One	188271
Tubes 50ml (sterile)	Greiner Bio-One	227261

II.10. Hardware

Hardware	Manufacturer	Catalogue ID
AutoMACS® Pro Separator	Miltenyi Biotec	
Cell culture incubator	Heraeus by Thermo Fisher Scientific	Function line BB16
Cell culture incubator	Heraeus by Thermo Fisher Scientific	Function line BB6060 0_2
Centrifuge	Eppendorf	5424R
Centrifuge	Eppendorf	5417R
Centrifuge	Eppendorf	5810R
Centrifuge	Sigma Laborzentrifugen	4K10
Flow cytometer	BD Biosciences	BD FACSCanto II
Flow cytometer	BD Biosciences	BD Fortessa
High throughput flow cytometry sampler	BD Biosciences	BD HTS for FACSCanto II
High throughput flow cytometry sampler	BD Biosciences	BD HTS for LSRFortessa
High-throughput gas chromatography with time-of-flight mass spectrometer	LECO Corporation	Pegasus III GC-TOF-MS
Inverted microscope	Nikon	Eclipse TS100
pH meter	Knick	766 Calimatic
QuadroMACS™ Separator	Miltenyi Biotec	
Real-Time PCR System	Applied Biosystem™ by Thermo Fisher Scientific	QuantStudio 3
Spectrophotometer	Peqlab	ND-1000
TEM	ZEISS	EM10CR
TEM stainer	Boeckeler Instruments	QG-3100
Thermal cycler	Perkin Elmer	Cetus 480

Thermomixer	Eppendorf	ThermoMixer® C
Ultramicrotome	Leica Microsystems	UC6
Water bath	Köttermann	3047

II.11. Software

Software	**Manufacturer**
BD FACSDiva™	BD Biosciences
ChromaTOF® 5.0	LECO Corporation
Excel® 2013	Microsoft Office Home and Business 2013
FlowJo 10.5.3	Tree Star by BD Biosciences
gimp 2.8.16	GNU General Public License
Illustrator CC2017	Adobe
Inkscape 0.91 r13725	GNU General Public License
LaTeX	GNU General Public License
Maui-SILVIA	*in-house* (Proteomics and Metabolomics Platform, Max-Delbrück Center for Molecular Medicine Berlin)
Primer Express version 3.0	Applied Biosystems™ by Thermo Fisher Scientific
Prism Version 8	GraphPad
QuantStudio™ Design & Analysis Software v1.4.3	Applied Biosystems™ by Thermo Fisher Scientific
R 3.5.1	GNU General Public License
RStudio	GNU General Public License
TeXmaker	GNU General Public License
Wave 2.6.0.31	Agilent Technologies

III. Methods

III.1. Generation of Bone Marrow-Derived Macrophages

Primary macrophages were generated from the bone marrow of male, 9 to 12 week old, wild type C57BL/6J mice. Animals were euthanized by inhalative isoflurane anesthesia and subsequent cervical dislocation. Freshly isolated femur and tibia were cleaned with 70% ethanol and flushed with differentiation medium (DMEM containing 25 mM glucose, 1 mM sodium pyruvate, and 3.97 mM L-glutamine, supplemented with 10% (v/v) fetal bovine serum (FBS), 5% (v/v) adult horse serum, 1% (v/v) non-essential amino acids, and 50 µM ß-mercaptoethanol) under sterile conditions. For macrophage differentiation, $1x10^7$ bone marrow cells were cultivated in 50 ml differentiation medium (see above) supplemented with 20% (v/v) L929 conditioned medium in *in-house* sealed, hydrophobic Teflon®-coated bags at 37 °C and 10% CO_2. Differentiation was performed for 9 to 10 days, resulting in bone marrow-derived macrophages at a consistent purity of over 90% of $CD11b^+$ $F4/80^+$ cells (determined by flow cytometry) (Figure 6).

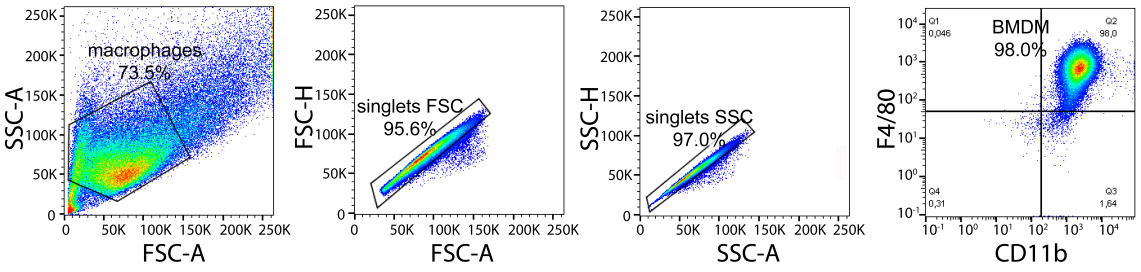

Figure 6: Gating strategy for BMDM. After isolating cells out of the Teflon®-coated bags they were stained with FITC-conjugated anti mouse CD11b and PB-conjugated anti mouse F4/80. After initial gating for macrophages and single cells, BMDM represent the $CD11b^+$ $F4/80^+$ population.

III.2. Generation of L929 Conditioned Media

L929 are a cell line producing CSF-1. Therefore, their supernatant can be used for the differentiation of macrophages as described before. For the generation of L929 conditioned medium cells were grown to confluency and cultured for 14 days in DMEM (containing 25 mM glucose, 1 mM sodium pyruvate, and 3.97 mM L-glutamine L-glutamine), supplemented with 10% (v/v) FBS, 1% (v/v) non-essential amino acids, 1% (v/v) HEPES, and 1% (v/v) penicillin-streptomycin, at 37 °C and 5% CO_2. Supernatants were filtered through a 70 µm cell strainer and aliquots stored at -20 °C until usage.

III.3. Isolation of Peripheral Blood Mononucleated Cells

Whole blood was drawn from healthy volunteers according the ethical approval EA2/046/17 in EDTA tubes. Peripheral blood mononucleated cells (PBMCs)-containing plasma was separated from erythrocytes by density gradient centrifugation, using isotonic Biocoll solution and SepMate tubes. After hypotone lysis of remaining erythrocytes with 155 mM NH_4Cl, 10 mM $NaHCO_3$ and 1 mM EDTA in water, cells were washed and frozen in medium, supplemented with 10% (v/v) fetal bovine serum and 10% (v/v) dimethylsulfoxide (DMSO).

III.4. Monocyte Isolation out of Peripheral Blood Mononucleated Cells

Total PBMCs were quickly thawed in warm DMEM medium. Cell number was determined and cells re-suspended in PBS, supplemented with 2mM of ethylenediaminetetraacetic acid (EDTA) and 0.5% (w/v) bovine serum albumin. Monocyte isolation was performed at 4°C, using the Pan Monocyte Isolation Kit human from Miltenyi Biotec and the autoMACS® Pro Separator (Miltenyi Biotec) according to the manufacturer's instructions. Purity of monocyte enrichment was determined by flow cytometric analysis (Figure 7). On average, 91.26 ±SD=6.40% of live cells were monocytes (Figure 8).

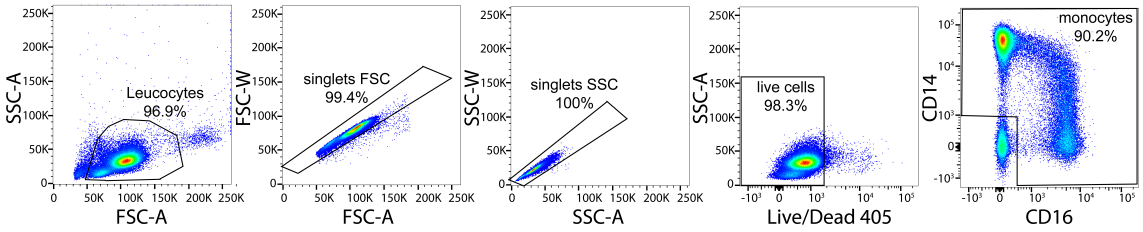

Figure 7: Gating strategy for human monocytes. After monocyte isolation cells were stained with PE Vio 770-conjugated anti human CD14 and FITC-conjugated anti human CD16, as well as LIVE/DEAD staining kit. After gating for leucocytes and single cells, monocytes represent the *classical* $CD14^{high}/CD16^{low}$, *intermediate* $CD14^{high}/CD16^{high}$, and *non-classical* $CD14^{low}/CD16^{high}$ populations of live cells.

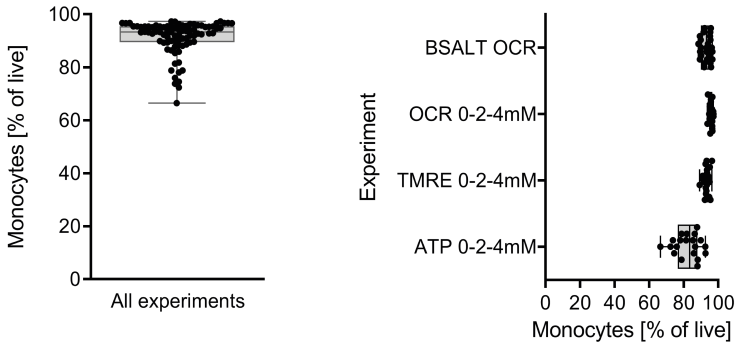

Figure 8: Percentage of human monocytes for all experiments performed (left panel, mean = 91.26 ±SD=6.40% of live cells) and for individual assays performed (right panel). BSALT OCR represents the Seahorse analyses for samples from the salt intervention study, OCR 0-2-4 mM represents the Seahorse analyses performed under *in vitro* salt treatment, TMRE 0-2-4 mM represents the mitochondrial membrane potential stainings performed under *in vitro* salt treatment, ATP 0-2-4 mM represents the ATP quantifications performed under *in vitro* salt treatment.

III.5. Macrophage Activation and Stimulation

After differentiating bone marrow cells into bone marrow-derived macrophages (BMDM) as described above, cells were harvested from the Teflon®-coated bags, pelleted and re-suspended in culture medium (DMEM with 10 mM glucose, 2 mM L-glutamine, 10% (v/v) FBS, 1% (v/v) penicillin-streptomycin, 1% (v/v) HEPES, and 50 µM ß-mercaptoethanol).

Cells were seeded at densities of $1x10^6$ cells / well of a 12-well plate or $2x10^6$ cells / well of a 6-well plate for gene expression analyses (see chapter III.6), $1x10^5$ cells / well of a 96-well plate for flow cytometric analyses (see chapter III.11), $8x10^4$ cells / well of a XFe96-well plate for Seahorse analyses (see chapter III.8), and $5x10^6$ cells / 10 cm dish for pulsed stable isotope-resolved metabolomic (pSIRM) analyses (see chapter III.7).

After a two hours incubation at 37 °C and 5% CO_2 for the cells to adhere, BMDM were activated towards an M1- (with 10 ng/mL lipopolysaccharide (LPS)) or M2- (with 10 ng/mL interleukin (IL) 4 and 10 ng/mL IL13) like phenotype. For the activation under high salt conditions, 40 mM sodium chloride (NaCl) were added to the medium. Pharmacologic inhibition of mitochondrial function was performed with Oligomycin A (Oligo), carbonyl cyanide 4-(trifluoromethoxy)phenylhydrazone (FCCP), N5,N6-bis(2-fluorophenyl)-[1,2,5]oxadiazolo[3,4-b]pyrazine-5,6-diamine (BAM15), or Antimycin A (AA) at concentrations of 10 µM, respectively. DMSO was included as solvent control if necessary.

Human blood-derived monocytes were seeded in 96-well plates at a concentration of $2x10^5$ cells / well in culture medium (DMEM with 10 mM glucose, 2 mM L-glutamine, 10% (v/v) FBS, 1% (v/v) penicillin-streptomycin, 1% (v/v) HEPES, and 50 µM β-mercapto-ethanol). For high salt treatment, 2 mM, 4 mM or 40 mM of NaCl were added for 3h.

III.6. RNA Purification, Preparation of cDNA and Quantitative Real-Time Polymerase Chain Reaction

Total messenger ribonucleic acid (mRNA) was isolated from 1-2x10^6 activated BMDM per well, grown and stimulated as described in chapter III.5, with QIAzol lysis reagent and the RNeasy® Mini Kit from QIAGEN. Samples were treated with DNase, according to the manufacturer's instructions, and eluted in RNase/DNase-free water. mRNA quality and concentration were measured with the NanoDrop Spectrophotometer ND-1000 from PeqLab. Samples were then diluted in RNase/DNase-free water to a final concentration of 500 ng mRNA / 10 µL.

The High Capacity cDNA Reverse Transcription Kit (Applied Biosystems™ by Thermo Fisher Scientific) was used to reverse transcribe 500 ng mRNA into respective 500 ng cDNA according to the manufacturer's protocol. cDNA was then diluted in RNase/DNase-free water to a final concentration of 10 ng cDNA / µL.

Quantitative real-time polymerase chain reaction (qPCR) (performed as TaqMan® assay with sequence specific DNA probes or as SYBR green assay) was used to quantify gene expression. Species specific primers (and probes) are listed in section II.6. Progression of qPCR was detected with the QuantStudio 3 Real-Time PCR System (Applied Biosystem™ by Thermo Fisher Scientific) and analysed with the QuantStudio™ Design & Analysis Software v1.4.3 (Applied Biosystems™ by Thermo Fisher Scientific). Gene expression was quantified using the relative standard curve method [88], where a cDNA mixture of all measured samples is used as standard curve, and normalized to expression levels of the ribosomal RNA gene 18 S.

III.7. Pulsed Stable Isotope-Resolved Metabolomics

BMDM were stimulated as indicated in chapter III.5. One hour prior the stimulatory end-point (i.e. after 2h and 23h), medium was changed to 13C-glucose or 13C-glutamine containing DMEM, supplemented with 10% (v/v) fetal bovine serum, 1% (v/v) penicillin-streptomycin, 1% (v/v) HEPES, 50 µM β-mercaptoethanol, 10mM glucose and 2mM glutamine (normal or 13C-labelled, depending on the experiment). After 1h of 13C-labelling (including the respective stimulants), cells were washed with a buffer containing 140mM NaCl, 5mM HEPES, and 4 mM KCl and lysed in methanol-chloroform-water (5:2:1 v/v/v), containing 2µg/mL cinnamic acid as internal control. For metabolite extraction, cell lysates were shaken for 60 min at 4°C and centrifuged for 15 min at 4°C and maximum speed. Polar phase was collected and dried under vacuum. Extracts were re-suspended in 20% methanol, shaken for 60 min at 4°C and polar phase again dried under vacuum. For derivatization, dried extracts were dissolved in 40mg/mL methoxyamine hydrochloride in pyridine and incubated for 90 min at 30°C. Subsequently, N-methyl-N-[trimethylsilyl]trifluoroacetamide (MSTFA) was added and incubated for 45 min at 37°C. A mixture of nine alkanes (n-decane, n-dodecane, n-pentadecane, n-octadecane, n-nonadecane, n-docosane, n-octacosane, n-dotriacontane, and n-hexatriacontane) dissolved in hexane, each at a concentration of 2 mg/mL, was added during derivatization to the MSTFA at a concentration of 2% (v/v). These served as retention index standard. Centrifuged extracts were aliquoted in glass vials for gas chromatography-mass spectrometry and measured on a gas chromatography coupled to time of flight mass spectrometer (Pegasus III- TOF-MS-System, LECO Corporation), complemented with an auto-sampler (MultiPurpose Sampler 2 XL, Gerstel). Measurement was performed in cooperation with Dr. Stefan Kempa at the Proteomics and Metabolomics Platform from the Berlin Institute of Medical Systems Biology.

In parallel to the samples a set of Ident and Quant mixes were extracted, derivatized and measured. The Ident mix is a combination of 102 compounds combined in 4 combi-

nations (A, B, C, D) in such a manner, that they are once measured without interfering compounds at similar retention indices, and once with interfering compounds. Thereby, compounds of similar retention indices can be distinguished more easily. The quant mix is composed of 63 compounds (stock concentrations 1 mg/mL). All compounds were combined 1:1 in a master mix, and then diluted in steps of 1:1, 1:2, 1:5, 1:10, 1:20, 1:50, 1:100 to 1:200. Thereby, quantification of detected metabolites was possible.

The samples and Ident/Quant standards were injected in split mode (split 1:5, injection volume 1 µL) in a temperature-controlled injector (CAS4, Gerstel) with a baffled glass liner (Gerstel). The following temperature program was applied during sample injection: initial temperature of 80°C for 30 s followed by a ramp with 12°C/min to 120°C and a second ramp with 7°C/min to 300°C and final hold for 2 min. Gas chromatographic separation was performed on an Agilent 6890 N, equipped with a VF-5 ms column of 30 m length, 250 µm inner diameter, and 0.25-µm film thickness (Varian). Helium was used as carrier gas with a flow rate of 1.2 ml/min. Gas chromatography was performed with the following temperature gradient: 2 min heating at 67.5°C, first temperature gradient with 5°C/min up to 120°C; subsequently, a second temperature increase of 7°C/min up to 200°C, 12°C/min up to 320°C and a hold of 6 min. The spectra were recorded in a mass range of 60 to 600 mass units with 10 spectra/s at a detector voltage of 1650 V.

The GC–MS chromatograms were initially pre-processed with ChromaTOF (Leco). Metabolite identification was performed with MAUI-SILVIA [89], a software developed by the Proteomics and Metabolomics Platform at the Max-Delbrück Center for Molecular Medicine (MDC), using the Ident mix and the Golm metabolome database. Absolute quantities were determined with the help of the Quant mix standards. Sample quantities were normalized to protein content (determined in parallel to the metabolite extraction), the internal control cinnamic acid, and the sum of all peak areas (as the total intensity should be consistent among samples). Measurement quality control, metabolite quantification and 13C-incorporation was performed using the MTX-QC R skript [90] developed by the Proteomics and Metabolomics Platform at the MDC.

III.8. Seahorse

During a Seahorse analysis the rate of change per minute of dissolved oxygen and pH in the media surrounding living cells is measured. A decrease in oxygen is measured as oxygen consumption rate (OCR) and serves as surrogate for mitochondrial respiration. An increase in pH is recorded as extracellular acidification rate (ECAR) and describes glycolytic activity.

Cells are grown (and stimulated) in XFe96 microplates as described in chapter III.5. However, during the assay an unbuffered medium needs to be used. Prior to the analysis, cells are therefore washed with unbuffered, DMEM-formulated Seahorse base medium (supplemented with 10 mM glucose and 2 mM L-glutamine as for the standard BMDM culture medium, see III.5) and incubated for 60 min at 37 °C, without CO_2 (in order to reduce the buffering capacity of CO_2 reacting with water in the medium and forming bicarbonate (HCO_3^-)). For the analysis, cells are then loaded onto the Seahorse XFe Analyzer (Agilent) together with a pre-calibrated disposable cartridge, placed into the microplate. The measurement of OCR and ECAR is performed in real-time, using optical fluorescent biosensors embedded in the cartridge.

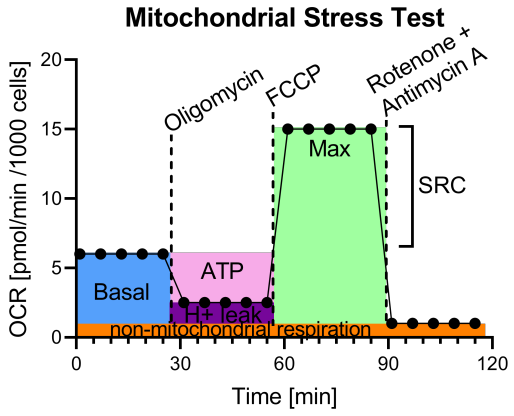

Figure 9: Pictogram of a Seahorse mitochondrial stress test. First, basal OCR is measured (blue phase). Oligomycin injection decreases OCR. ATP-coupled oxygen consumption (pink delta between basal OCR and oligomycin-reduced OCR) can be calculated from this phase. Injection of FCCP increases OCR maximally (green phase). Injection of rotenone and antimycin A inhibit mitochondrial respiration maximally, leaving residual non-mitochondrial respiration (orange OCR). The difference between non-mitochondrial respiration and post-oligomycin OCR constitutes proton leak-associated OCR (violet delta).

In order to analyse different aspects of mitochondrial respiration, a so-called mitochondrial stress test was performed. The assay was designed to repeat cycles of 3 minutes mixing followed by 3 minutes measuring. During a first phase, 5 cycles of basal

OCR were measured, followed by three injections of different mitochondrial inhibitors with 5 cycles per test phase (see Figure 9). Phase II consisted of the injection of 2µM oligomycin to inhibit mitochondrial ATPase and therefore decrease OCR. ATP-coupled oxygen consumption (i.e. the difference of basal OCR to oligomycin-reduced OCR) can be calculated based on this phase. During phase III, 1µM mitochondrial uncoupler and ionophore Carbonyl cyanide 4-(trifluoromethoxy)phenylhydrazone (FCCP) was added, in order to dissipate mitochondrial proton gradient. This chemically-induced proton leak induces a very high oxygen consumption. This phase therefore represents the maximal OCR and the difference of maximal OCR over basal OCR constitutes the spare respiratory capacity (SRC). During phase IV, rotenone and antimycin A are injected to inhibit ETC complexes I and III, respectively. Mitochondrial oxygen consumption is then fully inhibited, with the remaining OCR representing non-mitochondrial respiration. The difference between non-mitochondrial respiration and post-oligomycin OCR constitutes proton leak-associated OCR (see Figure 9).

After the assay, a nuclear staining with Hoechst was performed (1:1000 in cell culture medium for 45 min at 37 °C). Cells were then washed with PBS and detached with 2 mM EDTA in PBS for 10 min on ice. Cell number was then determined by flow cytometry in order to normalize OCR to cell count per well.

Human blood-derived monocytes were treated equally. However, as monocytes are non-adherent, cells needed to be centrifuged between washes (for 5 min at 300xg) and detaching was not necessary.

III.9. Transmission Electron Microscopy

BMDM were grown and stimulated as indicated in chapter III.5, washed with PBS, detached with 2mM EDTA in PBS and gentle scraping, and cell pellet fixed with 2.5% glutaraldehyde in PBS for 2h at 4°C. Tonicity during washes, detachment, and fixation was adjusted to +40mM NaCl for the respective high salt groups. The pellets were rinsed several times in the same buffer and postfixed in 1% osmium tetroxide buffered in the respective buffer (normal salt or high salt) for 30 min at 4°C. The material was subsequently dehydrated in an acetone series and embedded in epoxy resin using the EMbed-812 kit. Series of silver to grey interference color (50-65 nm) were made sectioned with a diamond knife in an ultramicrotome and kept in formvar covered single slot grids. The sections were stained with 2% uranyle acetate and 2.6% lead citrate after Reynolds in an automated TEM stainer and examined under a ZEISS EM10CR. Images were recorded on phosphate negatives (Ditabis). Series of 20 to 30 sections of a single cell from each sample were recorded at higher magnification (12500 to 20000 times) and used for partial reconstruction of the mitochondrium. Images were aligned using IMOD and IMOD-align (Boulder Laboratories). Aligned TEM images were then used to reconstruct the mitochondrial network within a $\pm$1.5 µm thick segment of each cell using the software Amira (6.5.0).
TEM was performed in cooperation with Prof. Dr. Thomas Bartolomaeus from the Institute for Evolutionary Biology and Ecology (IEZ) at the university of Bonn.

III.10. Determination of Intracellular ATP

Quantification of intracellular ATP of BMDM and human blood-derived monocytes was performed using the ATPlite Luminescence Assay System. Cell supernatant was discarded, cells lysed and luminescence measured according to the manufacturer’s protocol.

III.11. Determination of Mitochondrial Membrane Potential

Mitochondrial membrane potential was determined by flow cytometry using Tetramethylrhodamine ethyl ester perchlorate (TMRE), MitoTracker Green FM, and Hoechst nuclear staining.

Cells were activated as described earlier (see chapter III.5). During the last hour of stimulation, cells were incubated for 60 min at 37°C with MitoTracker Green FM and Hoechst, each at a concentration of 1:10000 into cell culture medium. TMRE staining was performed during the last 20 min at 37°C at a concentration of 1:25000. Cells were then washed with PBS, detached (in case of BMDM) with 2mM EDTA in PBS on ice and analysed via flow cytometry.

Mitochondrial membrane potential was also determined in isolated mitochondria. Therefore, BMDM were harvested from the Teflon®-coated bags and cell number adjusted to $1x10^7$ in the Miltenyi Biotec Mitochondrial Lysis buffer, supplemented with 5% (v/v) complete protease inhibitor cocktail. Cells were then lysed with a 30G needle on ice, magnetically labelled and mitochondria isolated using the Miltenyi Biotec Mitochondria Isolation Kit and the QuadroMacs Separator according to the manufacturer's instructions. Isolated mitochondria were re-suspended in a mitochondrial respiration buffer containing 180 mM sucrose, 0.1 mM EDTA, 60 mM KCl, 10 mM K_3PO_4, 12 mM $K_2CO_3$3, 2mM K-lactate, 2 mM Na-pyruvate, 2 mM K_3-citrate, 2mM K-2-oxo-glutaric acid, 1 mM Na_2-fumarate, 2 mM Na_2-succinate, 1 mM malate, 1 mM glutamine, 0.035 mM ADP, 1 mM glycine, 1 mM alanine, 1 mM asparagine, 1 mM aspartic acid, 1 mM glutamate, 1 mM proline, and 1 mM serine. They were then stained and analysed as described above for cells.

III.12. Determination of Intracellular NAD and NADH

Quantification of intracellular total NAD and NADH of BMDM was performed using the NAD/NADH colorimetric assay kit from Abcam. Cell supernatant was discarded, cells lysed and lysate split into two equal parts. One part was heated at 60°C for 30 min, in order to decompose all NAD^+. Absorbance of both parts (incubated with the provided reaction mix) was measured at 450 nm according to the manufacturer's protocol. The assay is based on the conversion of NAD^+ to NADH by the developer added. Thereby, NADH is detected in the heated half of the lysate (where no NAD^+ is present), whereas total NAD is detected in the untouched half. The amount of NAD^+ can be calculated as the difference between total NAD and NADH.

III.13. Electron Transport Chain Complex Assays

The activity of mitochondrial electron transport chain complexes can be detected with different kits.

Complex I activity was determined with the colorimetric Complex I Enzyme Activity Microplate Assay Kit. Cell supernatant was discarded, cells lysed with the supplied lysis buffer and protein concentration determined with the NanoDrop Spectrophotometer ND-1000 from PeqLab. Protein concentration was adjusted to 5mg/mL and 200 µL / well of the supplied 96-well plate were added and incubated for 3h at room temperature. Complex I NADH dehydrogenase was thereby bound to the plate. After thorough washing, the supplied reaction mix as well as increasing concentrations of NaCl (serial dilutions from 64mM to 0.0625mM NaCl) were added to the plate. Finally, NADH was added to the mix and absorbance at 450 nm was measured in kinetic mode.

Complex II/III activity was assessed using the MitoTox Complex II + III OXPHOS Activity Assay Kit according to the manufacturer's instructions. Activity solution was mixed

with increasing concentrations of NaCl (serial dilutions from 64mM to 0.0625mM NaCl) or Antimycin A as positive control (serial dilutions from 352nM to 0.3438nM). Bovine heart mitochondria were added and absorbance at 550 nm was measured in kinetic mode. Complex II/III activity was calculated relative to the solvent control (water or DMSO, respectively).

III.14. Bacterial infection

BMDM were seeded in 24-well culture plates, activated as described in chapter III.5, and infected with E. coli HB101 (MOI 100). One hour post-infection, cells were washed twice with PBS and incubated in medium containing 100 µg / mL gentamicin for two additional hours. Where indicated, 40 mM NaCl or mitochondrial inhibitors were added to the medium. Subsequently, the infected cells were lysed in PBS containing 0.1% Triton-X and 0.05% Tween 80. Bacterial survival was assessed by plating serial dilutions on Müller-Hinton-II agar plates and counting colony-forming units (CFUs) after one day of incubation. Bacterial infection assays were performed by Patrick Neubert (of Prof. Dr. Jonathan Jantsch's group from the Institute for Microbiology and Hygiene at the University of Regensburg (IMHR)).

III.15. Statistics

Statistical analyses were performed with GraphPad Prism Version 8.3.0. Data are expressed as mean ± SEM. Normality of the data was tested by Kolmogorov-Smirnov test. Significance between two groups was analysed by unpaired *t*-test (when normal distributed), Mann-Whitney test (when non-normal distributed) or Wilcoxon matched-pairs signed rank test (for non-normal distributed, matched data). For more than two groups with one variable only, one-way ANOVA with Tukey's post-hoc test (for normal distributed data) or Kruskal-Wallis test with Dunn's post-hoc test (for non-

normal distributed data) were used. Matched data with more than two groups (or time points) was analized by Friedman test and FDR-correction was performed via Benjamini-Hochberg procedure. For more than two groups with three variables three-way ANOVA with Benjamini-Hochberg FDR-correction was performed. Relationship between normal distributed data sets was determined by Pearson correlation and linear regression analysis. Relationship between non-normal distributed data sets was assessed by Spearman correlation and linear regression analysis. Exact statistical tests used are described in the respective figure legends. Respective p-values were depicted in the figures. After FDR-correction, q-values were reported.

Statistical analysis of the gene expression data (Figure 12) was performed by Dr. Sofia Forslund. A nested model test, treating salt status as covariate, was performed for the gene expression data. Furthermore, Kruskal–Wallis test with Mann-Whitney *U* post-hoc test, comparing NS to HS to each time point for each activation group, was performed. FDR-correction was done via Benjamini-Hochberg procedure.

IV. Results

Based on the early functional impact on macrophage function described by Neubert *et al.* and the importance of metabolic reprogramming for macrophage activation we asked whether HS affects early macrophage metabolism. We hypothesized that HS has an impact on early macrophage CCM and thereby induces the differential gene expression and boosted bacterial killing capacity. In order to test our hypothesis, we generated and activated BMDM as indicated in Figure 10. Murine bone marrow cells (BMC) were differentiated into BMDM (also named unstimulated M0 macrophages) for 9 to 10 days with colony-stimulating factor 1 (CSF-1) in Teflon®-coated bags. BMDM were then activated with LPS or IL4 and IL13 to *classic* M1 (in green) or *altenative* M2 (in blue) macrophages, under NS conditions or under the addition of 40mM NaCl.

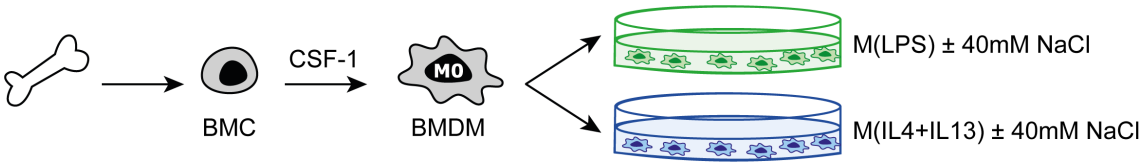

Figure 10: Generation and activation of bone marrow-derived macrophages. Murine bone marrow cells (BMC) were incubated for 9 to 10 days with colony-stimulating factor 1 (CSF-1) in Teflon®-coated bags, differentiating them into bone marrow-derived macrophages (BMDM or M0 macrophages). These were then activated with LPS or IL4 and IL13, in order to polarize them towards M1 (in green) or M2 (in blue) macrophages. Macrophage activation was performed under normal salt conditions or under the addition of 40mM NaCl.

To get an impression of the dynamics of macrophage activation, as well as the differential impact of HS on this activation, we analyzed the gene expression of known M1 and M2 markers to different time points. As indicated in Figure 11 BMDM were activated for 1h, 3h, 6h, and 24h and the expression of *Ccl5* (Figure 11a), *Tnf* (Figure 11b), *Irf5* (Figure 11c), *Cox2* (Figure 11d), *Nos2* (Figure 11e), *Slamf1* (Figure 11f), *Nlrp3* (Figure 11g), *Arg1* (Figure 11h), *Irf4* (Figure 11i), *Chil3* (Figure 11j), *Retnla1* (Figure 11k), *Mgl2* (Figure 11l), and *Mrc1* (Figure 11m) (all normalized to the house-keeping gene *18S*) was analyzed by qPCR. Statistical analysis and data interpretation was done in Figure 12.

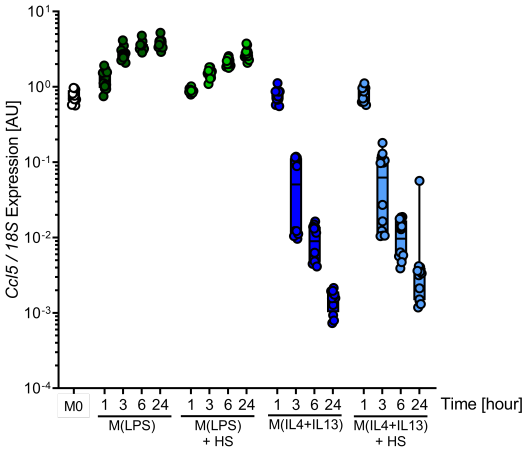

(a) Relative gene expression *Ccl5/18S*

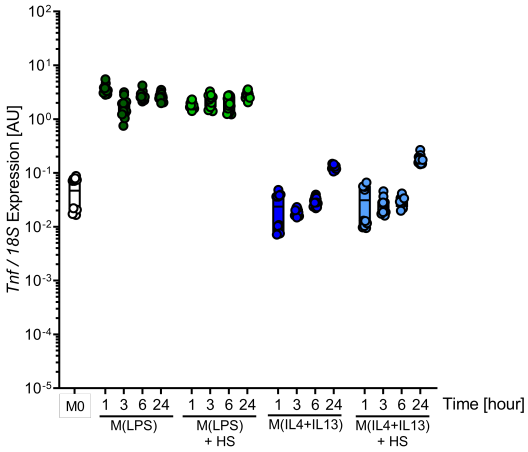

(b) Relative gene expression *Tnf/18S*

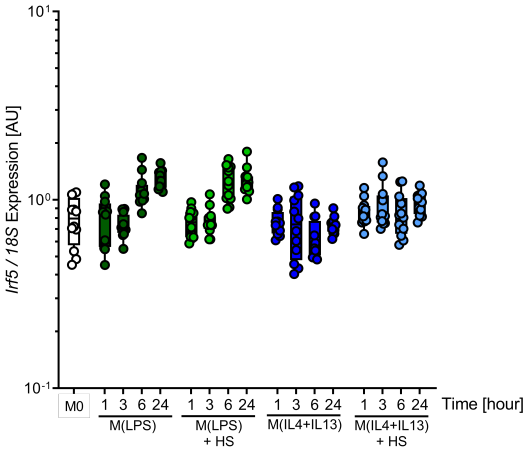

(c) Relative gene expression *Irf5/18S*

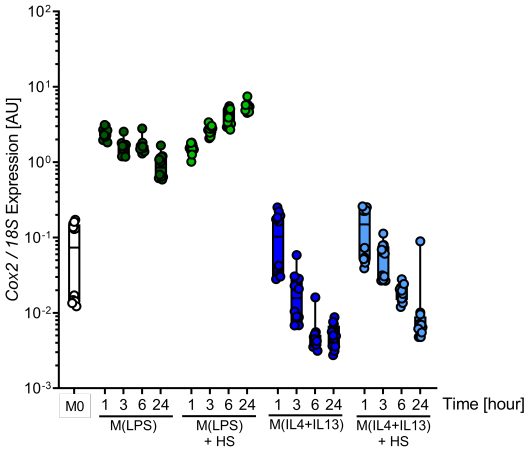

(d) Relative gene expression *Cox2/18S*

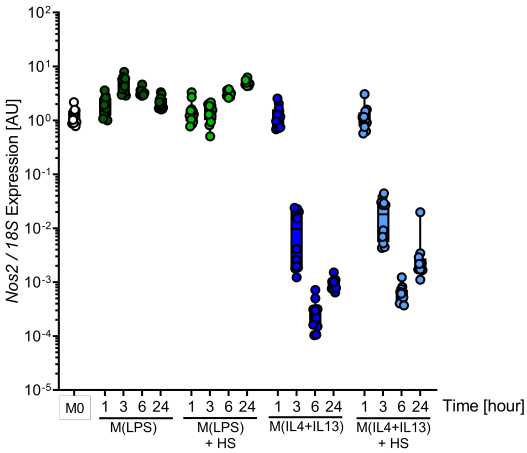

(e) Relative gene expression *Nos2/18S*

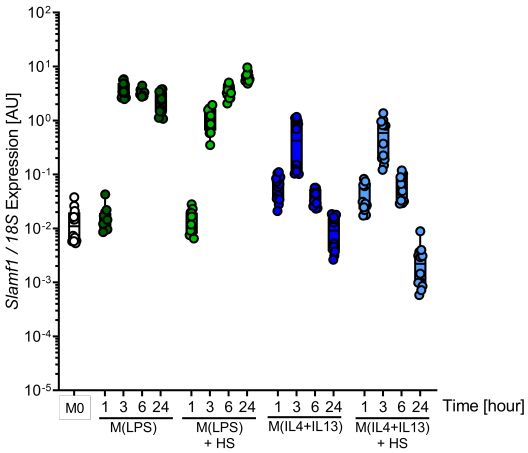

(f) Relative gene expression *Slamf1/18S*

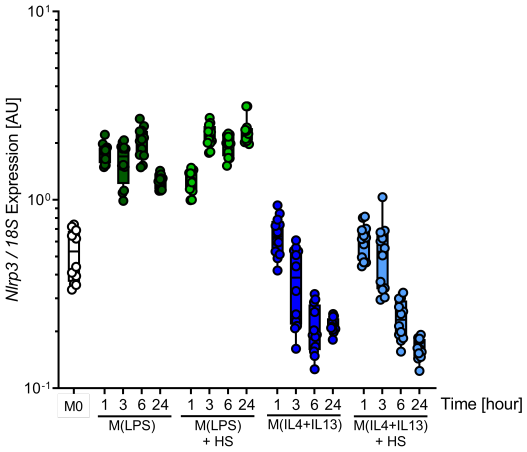

(g) Relative gene expression *Nlrp3/18S*

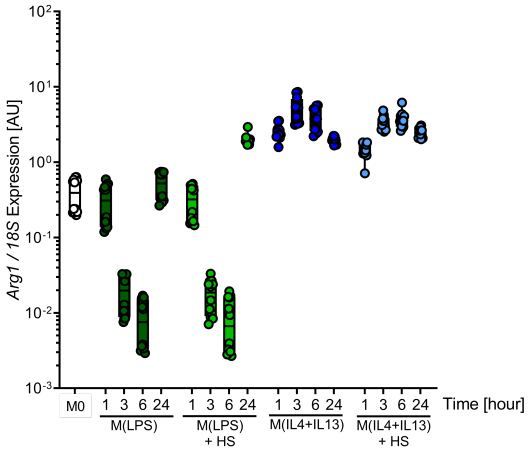

(h) Relative gene expression *Arg1/18S*

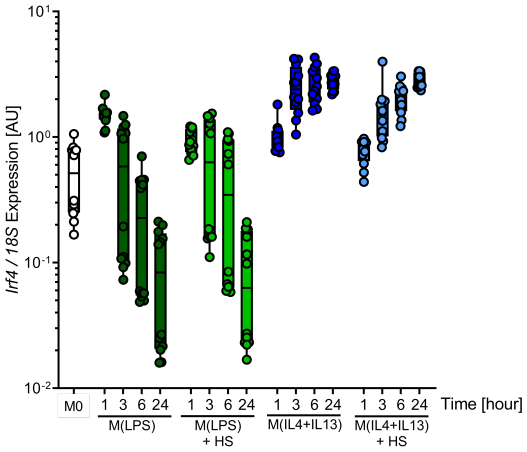

(i) Relative gene expression *Irf4/18S*

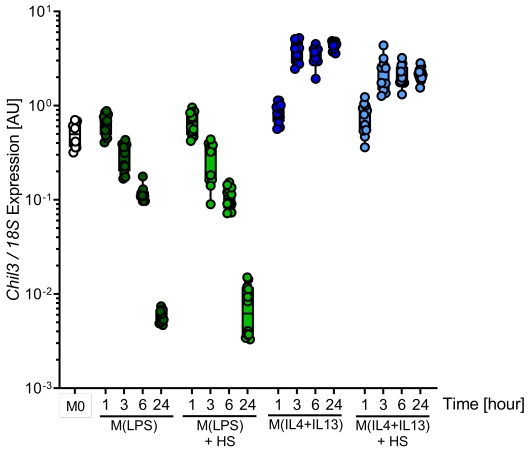

(j) Relative gene expression *Chil3/18S*

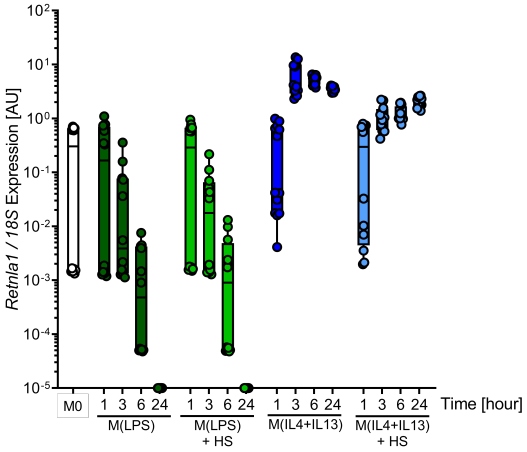

(k) Relative gene expression *Retnla1/18S*

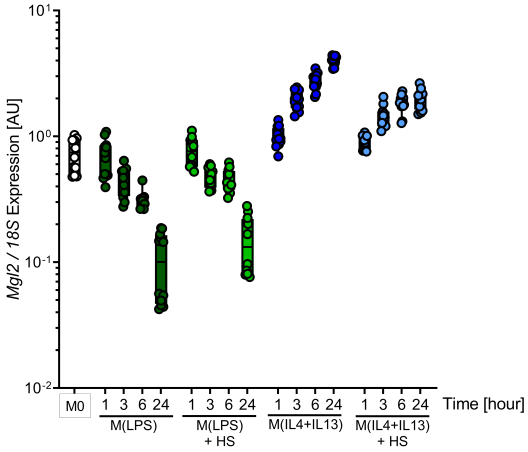

(l) Relative gene expression *Mgl2/18S*

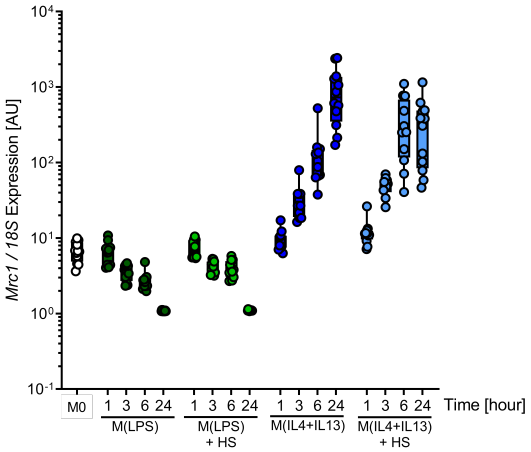

(m) Relative gene expression *Mrc1/18S*

Figure 11: Relative gene expression of pro-inflammatory M1 marker genes *Ccl5* (a), *Tnf* (b), *Irf5* (c), *Cox2* (d), *Nos2* (e), *Slamf1* (f), *Nlrp3* (g) and anti-inflammatory M2 marker genes *Arg1* (h), *Irf4* (i), *Chil3* (j), *Retnla1* (k), *Mgl2* (l), *Mrc1* (m) normalized to the house-keeping gene *18S*. Represented groups are unstimulated M0 (in white) as well as M(LPS) (in green) and M(IL4+IL13) (in blue) macrophages activated for 1h, 3h, 6h and 24h under normal salt (dark green and dark blue) or high salt (HS) (light green and light blue) conditions. Two pooled experiments with a total of n=12 replicates per group and time point are shown. Data is depicted as mean ±SEM in boxplots with individual data points.

Figure 12a illustrates the impact of LPS and IL4+IL13 treatment over the course of time. The heat map displays the fold change induction and inhibition of macrophage marker genes compared to unstimulated M0 macrophages. M(LPS) macrophages show a significantly induced expression of *Ccl5*, *Tnf*, *Cox2*, *Nos2*, *Nlrp3*, and *Irf4* after only 1 h. Similarly, M(IL4+IL13) macrophages have a significantly higher expression of *Arg1*, *Irf4*, *Chil3*, *Mgl2*, *Mrc1*, and, interestingly, pro-inflammatory *Tnf*, *Slamf1*, and *Nlrp3* compared to M0 macrophages after only 1h. After only 3h, transcriptional commitment to a pro- or anti-inflammatory phenotype is complete, with significant induction of most pro-inflammatory markers and inhibition of anti-inflammatory markers in M(LPS) and vice versa in M(IL4+IL13). Besides *Irf5*, the induction of the respective markers did not change any further after 6h and 24h.

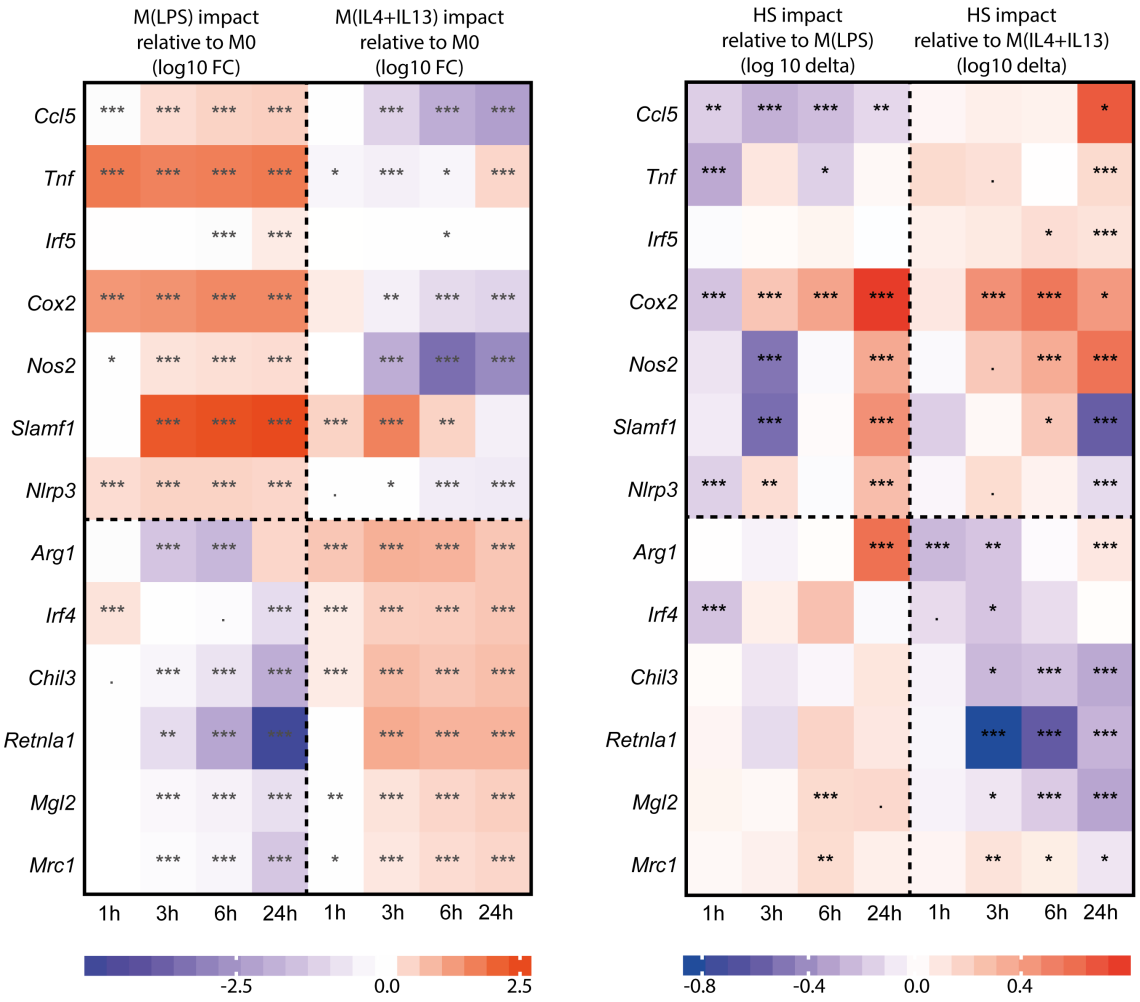

(a) Activation impact relative to M0

(b) High salt impact relative to NS

Figure 12: Relative gene expression of pro-inflammatory M1 marker genes *Ccl5*, *Tnf*, *Irf5*, *Cox2*, *Nos2*, *Slamf1*, *Nlrp3* and anti-inflammatory M2 marker genes *Arg1*, *Irf4*, *Chil3*, *Retnla1*, *Mgl2*, *Mrc1* normalized to the house-keeping gene *18S* in M0, M(LPS) and M(IL4+IL13) macrophages over time. Two pooled experiments with a total of n=12 replicates per group and time point are shown. Heat map in (a) depicts the impact of LPS or IL4 and IL13 activation over time relative to unstimulated M0 macrophages (logarithmic fold change (FC) is shown). A nested model test, treating HS treatment as covariate, was performed. Heat map in (b) depicts the HS impact relative to the NS equivalent to the same time point (logarithmic delta is shown). Kruskal–Wallis test with Mann-Whitney *U* post-hoc test, comparing NS to HS to each time point separately for each activation group was performed. FDR-correction was performed via Benjamini-Hochberg procedure. Significance symbols are defined as . for q<0.1, * for q<0.05, ** for q<0.01, and *** for q<0.001.

Figure 12b illustrates the impact of HS treatment in the respective groups over the course of time. The heat map displays the delta between NS and HS in M(LPS) and M(IL4+IL13) to each time point. In M(IL4+IL13) HS leads to an inmediate down-regulation of M2 marker genes. After only 3h, except for *Mrc1*, all M2 markers are significantly down-regulated. This confirms the inhibition of M(IL4+IL13) under

HS reported previously for the 24h post-stimulation time point [87]. Interestingly, they display a simultaneous induction of pro-inflammatory markers. Specially, *Tnf*, *Cox2*, *Nos2*, and *Nlrp3* are significantly up-regulated after only 3h compared to NS M(IL4+IL13). M(LPS) macrophages are reported to be boosted by HS after 24h [80, 86]. We confirm this data, showing a significant induction of *Cox2*, *Nos2*, *Slamf1*, and *Nlrp3* after 24h compared to NS M(LPS). During the early activation, by contrast, most pro-inflammatory markers are significantly decreased compared to the NS situation. Taken together, transcriptional macrophage activation is not only induced, but fully engaged after only 3h of stimulation. The impact of HS, however, is very variable over time, specially in M(LPS) macrophages.

Our main hypothesis was that HS had an impact on early macrophage metabolism. Based on the boosted bacterial killing capacity reported by Neubert *et al.* after 4h of stimulation and our gene expression analysis, showing full macrophage transcriptional activation and differential impact of HS after only 3h of stimulation, we decided to analyze the central carbon metabolism at this time point during macrophage activation. Via isotope tracing, it is possible to follow the break-down of such labelled metabolites in respective metabolic pathways. In mass spectrometry, a metabolite can be identified by the mass spectrum of it's fragments, i.e. the intensity of the fragment's peaks at a defined mass-to-charge ratio (m/z). The incorporation of isotopes into a metabolite changes the atomic composition of this intermediate. It induces a shift in the respective fragment's GC-MS spectrum, as the m/z increases. The induced mass shift (indicated as m+X) depends on the substrates used (e.g. sugars, amino acids or fatty acids) and the type of isotopic label (e.g. carbon-13, nitrogen-15, etc) as these determine the position of isotope incorporation and thereby the number of additional neutrons. By incubating BMDM with carbon-13 (13C) labelled glucose (13C-Glc) or 13C labelled glutamine (13C-Gln), we could trace glucose catabolism within glycolysis as well as glutamine incorporation and (glycolysis independent) TCA cycling.

As stated before, most research has been performed in end-phase macrophages. Metabolic tracing experiments, however, have been done not after 24h but during the

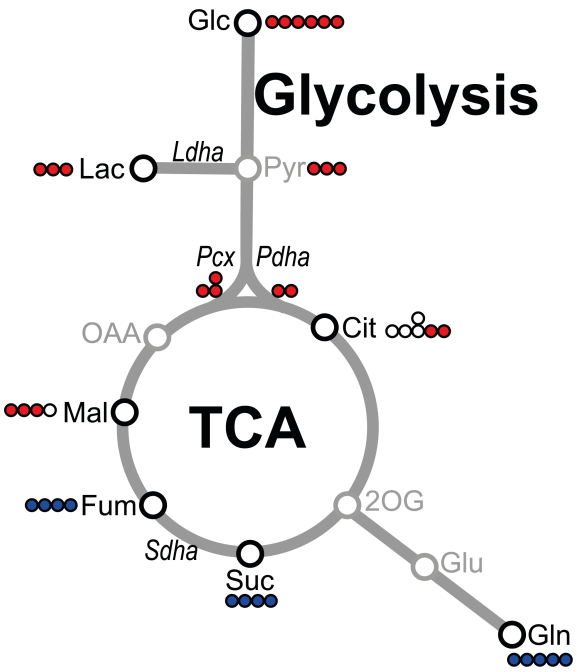

Figure 13: Pictogram of the central carbon metabolism, showing the routing of glucose- and glutamine-derived carbons. Glucose (Glc) can be catabolized within glycolysis to pyruvate (Pyr). Pyr can subsequently be metabolized by lactate dehydrogenase (encoded by *Ldha*) to lactate (Lac), by pyruvate dehydrogenase (encoded by *Pdha*) to citrate (Cit) or by pyruvate decarboxylase (encoded by *Pcx*) to malate (Mal) via oxaloacetate (OAA). Glutamine (Gln) can enter the TCA cycle via glutamic acid (Glu) into 2-oxo-glutaric acid (2OG). 2OG is then metabolized to succinate (Suc), further oxidized to fumarate (Fum) by succinate dehydrogenase (encoded by *Sdha*). By labeling with U-13C6-Glc or U-13C5-Gln, a different mass shift in each metabolite can be detected, depending on the metabolic route followed. Pyruvate dehydrogenase activity induces a mass shift of m+2 in Cit, whereas pyruvate carboxylase leads to a mass shift of m+3 in Mal. Gln-derived 13C incorporation into Suc and Fum induces a mass shift of m+4, respectively. Red and blue circles represent glucose- and glutamine-derived 13C atoms, respectively. White circles represent 12C atoms.

entire activation. Thus, BMDM were activated and simultaneously glucose or glutamine traced [3]. The resulting data is therefore a sum of all metabolic pathways engaged over the course of activation. In contrast, we performed pulsed stable isotope-resolved metabolomics (pSIRM). BMDM were therefore activated in regular glucose and glutamine containing medium for 3h. Only during the last hour of activation, medium was replaced by 13C-Glc or 13C-Gln containing medium, keeping the formulation identical. This relatively short ”pulse” of isotope labelled metabolites allows for a much better resolution of glucose and glutamine metabolization regarding the direction and velocity of label incorporation. Figure 13 illustrates the break down of 13C-Glc and 13C-Gln within glycolysis and TCA cycle. The red and blue circles represent the 13C-Glc and 13C-Gln derived 13C atoms, respectively. After metabolization into pyruvate (Pyr), glucose-derived 13C atoms can be detected in lactate (Lac), citrate (Cit) and malate (Mal). Glucose-derived 13C atoms incorporated into Lac induce a mass shift of m+3, as all carbon atoms have one neutron more than 12C-Lac. PDHA activity leads to an incorporation of two 13C atoms into Cit, inducing a mass shift of m+2. PC activity induces the incorporation of three 13C atoms into Mal and therefore a mass shift of m+3. Subsequent TCA cycling would increase the mass shifts even further, leading to m+4 in Cit and Mal, for example. However, we only focused on the first ”wave” of

glucose entry into the TCA cycle. Equally, glutamine entry into the TCA cycle can be followed by label incorporation in succinate (Suc) and fumarate (Fum) and subsequent mass shifts of m+4 (Figure 13).

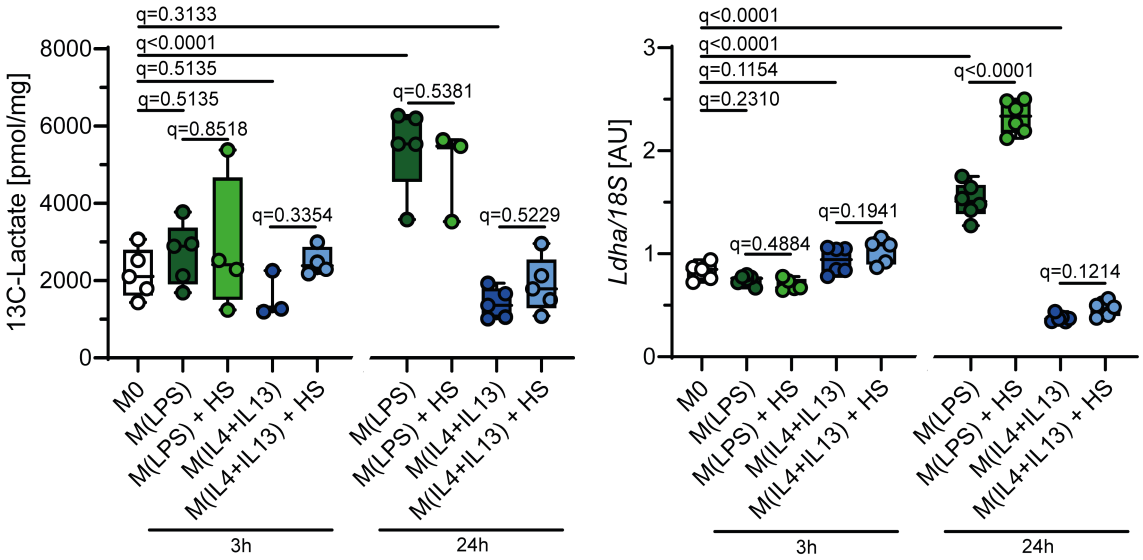

Figure 14: 13C-Glucose derived lactate with the respective *Ldha* relative gene expression. BMDM were activated for 3h and 24h with LPS or IL4 and IL13, under normal salt and high salt (HS) conditions. For pSIRM analyses, during the last hour of activation, medium was replaced to 13C-Glc containing medium (formulation was kept identical). PSIRM experiments were performed with n=5, gene expression with n=6 replicates. Data is depicted as mean ±SEM in boxplots with individual data points. Significance was analyzed by three-way ANOVA with Benjamini-Hochberg FDR-correction.

As mentioned above, we activated BMDM for 3h towards M(LPS) and M(IL4+IL13) under NS and HS conditions. During the last hour of activation, glucose in the medium was replaced by 13C-Glc. As shown in Figure 14 13C-Lactate levels were similar among all, unstimulated, M(LPS) and M(IL4+IL13) macrophages at this time point. Furthermore, HS did not induce any change in 13C-Lactate levels. When performing the same pSIRM experiment after 24h (i.e. 23h of activation followed by 1h of activation and 13C-tracing), 13C-Lactate was significantly increased in M(LPS) ($q<0.0001$ compared to M0), but not in M(IL4+IL13) macrophages. This confirms previous data, reporting an induction of anaerobic glycolysis in pro-inflammatory macrophages after 24h as their major energetic source. HS, in contrast, did not change anaerobic glycolysis in either group. Analysis of relative *Ldha* gene expression at the same time points

showed similar results. *Ldha* was equally expressed among all groups at 3h, but significantly up-regulated in M(LPS) macrophages after 24h (q<0.0001 compared to M0). Interestingly, *Ldha* expression was significantly down-regulated in M(IL4+IL13) macrophages after 24h (q<0.0001 compared to M0). This supports the notion of aerobic glucose utilization via TCA cycle and OXPHOS in M2 macrophages. HS further increased the up-regulation of *Ldha* in M(LPS) macrophages (q<0.0001 compared to M(LPS)), while not affecting the gene expression in M(IL4+IL13). With glycolysis being the major metabolic pathway engaged in late-phase M1 macrophages, this induction could support M(LPS) activation under HS conditions. However, there was no induction of 13C-Lactate or *Ldha* expression at 3h post-stimulation, suggesting that this might be a later mechanism for the HS impact on macrophage activation, not relevant at this stage.

As anaerobic glycolysis was not induced after 3h by HS, we wondered if glucose entry in TCA cycle was affected. Figure 15 and 16 display glucose-derived 13C-Citrate (m+2) and 13C-Malate (m+3) with their respective *Pdha* and *Pcx* relative gene expression in M(LPS) and M(IL4+IL13) under NS and HS conditions.

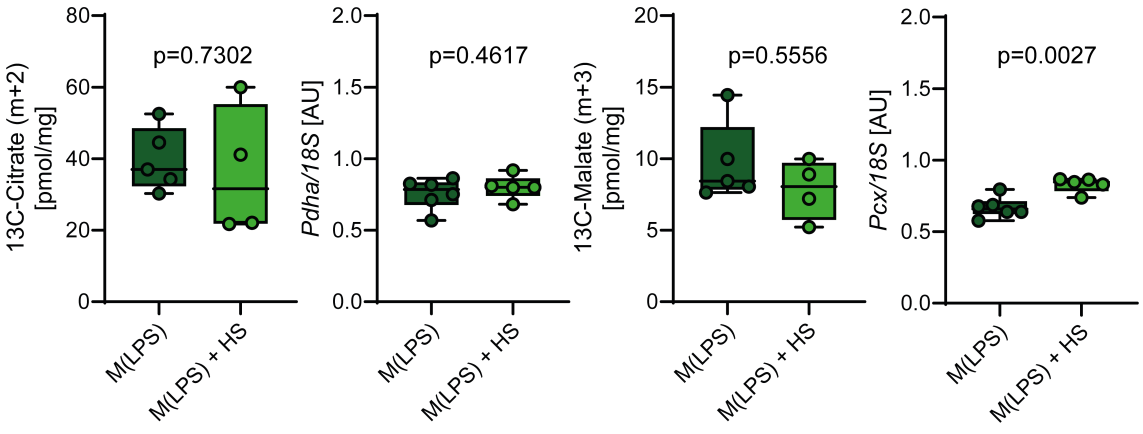

Figure 15: 13C-Glucose derived citrate (m+2) and malate (m+3) with the respective *Pdha* and *Pcx* relative gene expression. BMDM were activated for 3h with LPS or LPS +40mM NaCl (HS). For pSIRM analyses, during the last hour of activation, medium was replaced to 13C-Glc containing medium (formulation was kept identical). PSIRM experiments were performed with n=5, gene expression with n=6 replicates. Data is depicted as mean ±SEM in boxplots with individual data points. Normality was determined by Kolmogorov-Smirnov test. PSIRM data were analyzed by two-tailed Mann-Whitney test. Gene expression data by unpaired, two-tailed *t*-test.

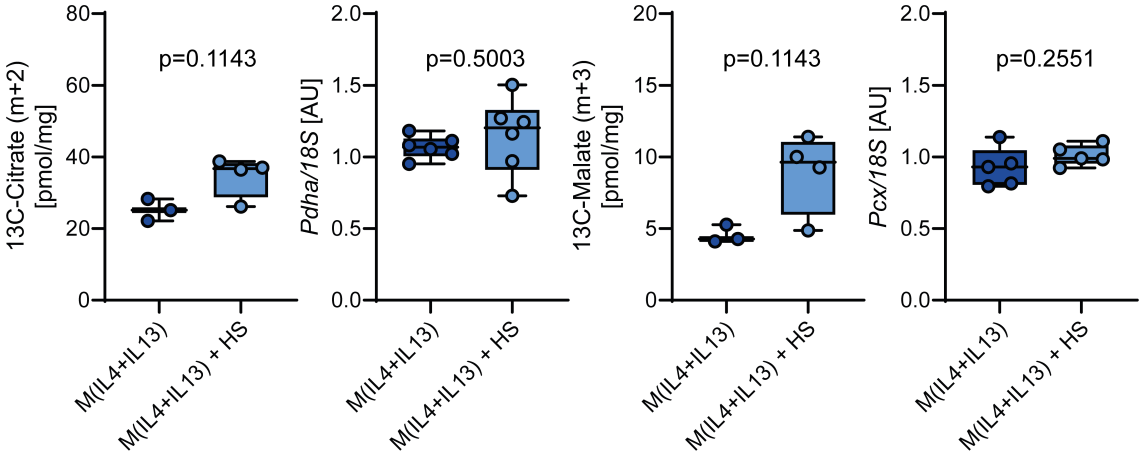

Figure 16: 13C-Glucose derived citrate (m+2) and malate (m+3) with the respective *Pdha* and *Pcx* relative gene expression. BMDM were activated for 3h with IL4 and IL13 or IL4 and IL13 +40mM NaCl (HS). For pSIRM analyses, during the last hour of activation, medium was replaced to 13C-Glc containing medium (formulation was kept identical). PSIRM experiments were performed with n=5, gene expression with n=6 replicates. Data is depicted as mean ±SEM in boxplots with individual data points. Normality was determined by Kolmogorov-Smirnov test. PSIRM data were analyzed by two-tailed Mann-Whitney test. Gene expression data by unpaired, two-tailed *t*-test.

Glucose-derived 13C-Citrate and 13C-Malate levels were unchanged in both M(LPS) (Figure 15) and M(IL4+IL13) (Figure 16) under HS treatment. Glucose-derived input into the TCA cycle was thus not affected by HS. Equally, *Pdha* expression was unchanged. Only *Pcx* expression was up-regulated in M(LPS) under HS conditions (p=0.0027 compared to M(LPS)). Taken together, neither anaerobic glycolysis nor glucose utilization as fuel for TCA cycle were affected by HS after 3h of activation.

In order to analyze TCA cycling independently of glycolytic influx, we performed 13C-Gln tracing experiments. As for the previous pSIRM experiments, BMDM were activated for 3h and glutamine was replaced by 13C-Gln during the last hour of activation only. Figure 17 and 18 display 13C-Gln derived 13C-Succinate and 13C-Fumarate in M(LPS) and M(IL4+IL13) macrophages. Oxidation of succinate to fumarate is mediated by SDHA. SDHA activity can thus be calculated based on the ratio of fumarate to succinate. Lastly, parallel RNA isolation was used to analyze *Sdha* gene expression at the same time point. As shown in Figure 17 and 18 levels of 13C-Succinate were not affected by HS. Glutamine-derived entry into the TCA cycle was thus unchanged upon HS. In

contrast, 13C-Fumarate levels were reduced by trend under HS conditions in both M(LPS) (p=0.0556) and M(IL4+IL13) (p=0.0714) compared to their NS controls. This results in a significantly inhibited SDHA activity in M(LPS) (p=0.0079) and M(IL4+IL13) (p=0.0357) upon HS treatment. *Sdha* expression, however, was unaffected in M(LPS) or even induced by trend in M(IL4+IL13) under HS (p=0.0645). In summary, our pSIRM data suggests that anaerobic glycolysis as well as TCA influx (both glycolytic and glutaminolytic) are not affected by HS after 3h of macrophage activation. However, TCA cycling seems to be inhibited at CII, as SDHA activity is decreased under HS.

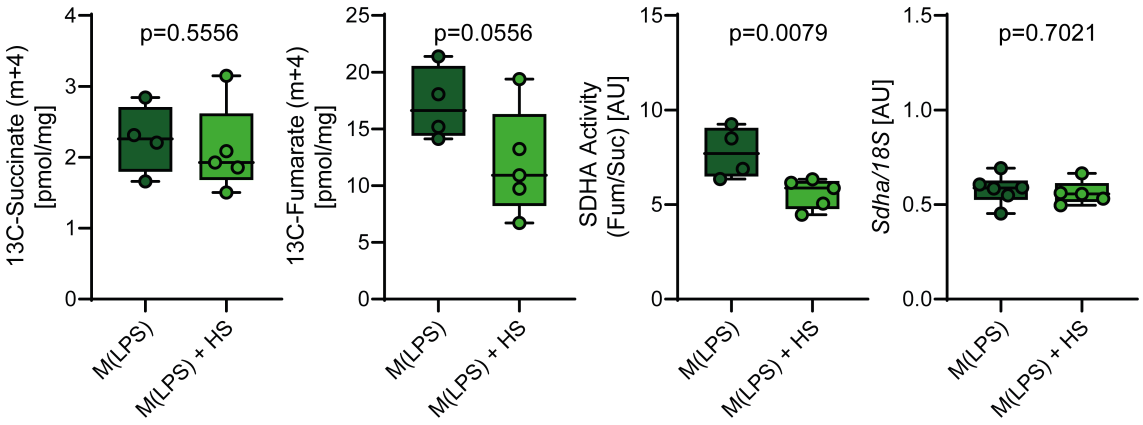

Figure 17: 13C-Glutamine derived succinate and fumarate (m+4), SDHA activity and *Sdha* relative gene expression. BMDM were activated for 3h with LPS or LPS +40mM NaCl (HS). For pSIRM analyses, during the last hour of activation, medium was replaced to 13C-Gln containing medium (formulation was kept identical). PSIRM experiments were performed with n=5, gene expression with n=6 replicates. SDHA activity was defined as the ratio of fumarate to succinate. Data is depicted as mean ±SEM in boxplots with individual data points. Normality was determined by Kolmogorov-Smirnov test. Succinate significance was analyzed by two-tailed Mann-Whitney test. Fumarate and SDHA activity significance was analyzed by one-tailed Mann-Whitney test. Gene expression data by unpaired, two-tailed *t*-test.

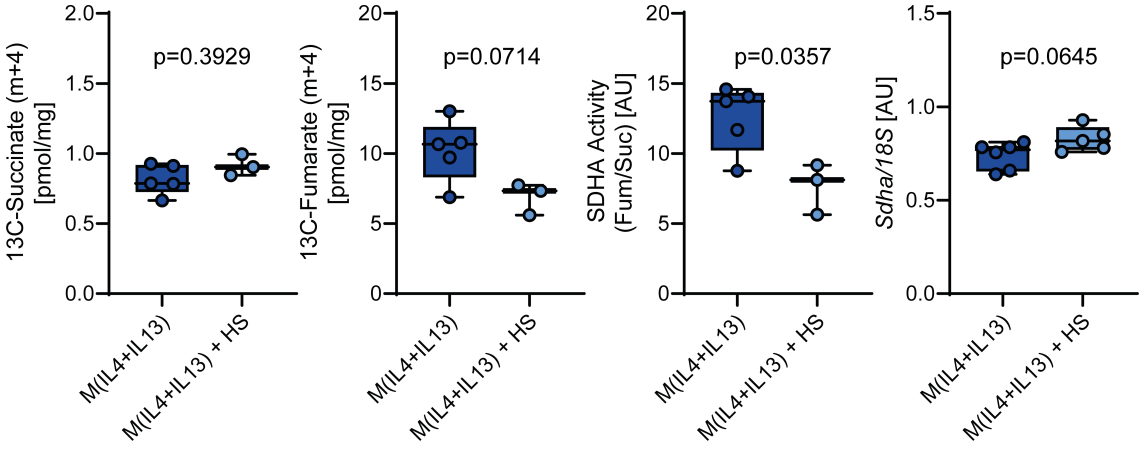

Figure 18: 13C-Glutamine derived succinate and fumarate (m+4), SDHA activity and *Sdha* relative gene expression. BMDM were activated for 3h with IL4 and IL13 or IL4 and IL13 +40mM NaCl (HS). For pSIRM analyses, during the last hour of activation, medium was replaced to 13C-Gln containing medium (formulation was kept identical). PSIRM experiments were performed with n=5, gene expression with n=6 replicates. SDHA activity was defined as the ratio of fumarate to succinate. Data is depicted as mean ±SEM in boxplots with individual data points. Normality was determined by Kolmogorov-Smirnov test. Succinate significance was analyzed by two-tailed Mann-Whitney test. Fumarate and SDHA activity significance was analyzed by one-tailed Mann-Whitney test. Gene expression data by unpaired, two-tailed *t*-test.

In an attempt to understand TCA-fueled OXPHOS, we analyzed mitochondrial oxygen consumption rate (OCR) via Seahorse technology. BMDM were activated for 3h to M(LPS) and M(IL4+IL13) under normal or high salt conditions. As for the pSIRM experiments, during the last hour of activation the medium needed to be changed. For Seahorse measurements the use of an unbuffered medium is crucial. The formulation (as well as glucose and glutamine content) was nonetheless kept identical to the standard cultivation and pSIRM media.

As shown in Figure 19, during a so-called mitochondrial stress test first basal OCR is measured. This parameter serves as a surrogate parameter for OXPHOS. Subsequent injection of 2µM of oligomycin inhibits mitochondrial ATPase and leads to a decrease in OCR. Injection of FCCP dissipates the proton gradient accros the inner mitochondrial membrane, leading to a maximally increased oxygen consumption. This parameter represents the maximal OXPHOS the respective cells are able to carry out. Injection of rotenone and antimycin A (Rot+AA) inhibit ETC CI and CIII and thereby all mitochondrial oxygen consumption. Remaining OCR is minimal and accounts for enzymatic

reactions and oxygenases. The difference between this non-mitochondrial respiration and post-oligomycin OCR constitutes proton leak-associated OCR (H+ leak). H+ leak is high when the inner mitochondrial membrane is structurally impaired or when the ETC is uncoupled from ATP synthesis at CV (e.g. in brown adipose tissue in order to generate heat).

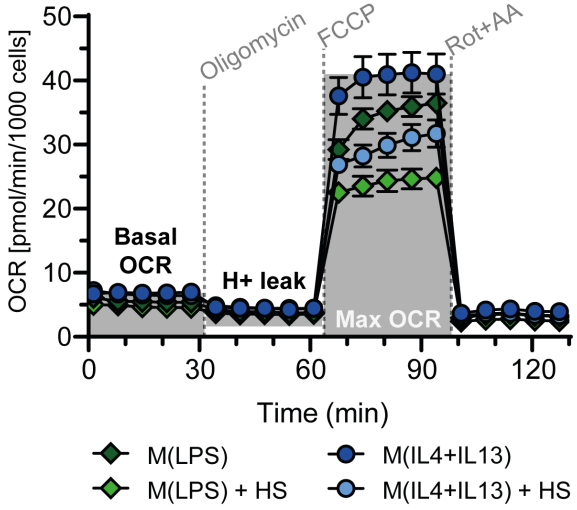

Figure 19: Representative real-time measurement of mitochondrial oxygen consumption rate (OCR) with Seahorse technology. BMDM were stimulated with LPS or IL4 and IL13 under normal or high salt (HS) conditions for 2h prior the first measurement, in order to analyse the third hour of activation. First, basal OCR is measured. Subsequent injection of 2µM oligomycin inhibits mitochondrial ATPase and leads to a decrease in OCR (representing the ATP-coupled respiration). Injection of FCCP dissipates mitochondrial proton gradient, leading to a maximally increased oxygen consumption. Injection of rotenone and antimycin A (Rot+AA) inhibit mitochondrial respiration maximally, leaving residual non-mitochondrial respiration. The difference between non-mitochondrial respiration and post-oligomycin OCR constitutes proton leak-associated OCR (H+ leak).

As depicted in Figure 20, basal OCR was significantly reduced under HS treatment in both M(LPS) (p=0.0317 compared to NS) and M(IL4+IL13) (p=0.0117 compared to NS) macrophages after 3h of activation. Furthermore, as shown in Figure 21, also maximal OCR was reduced under HS stimulation by trend in M(LPS) (p=0.0683 compared to NS) and significantly in M(IL4+IL13) (p=0.0232 compared to NS). This data contrasts to the unchanged TCA influx shown by our pSIRM experiments. Whereas there was no difference in glucose- and glutamine-derived input into the TCA cycle, the outcome at the ETC in the form of OXPHOS was significantly inhibited under HS. This suggests a metabolic uncoupling of TCA cycle and OXPHOS. As SDHA activity (part of CII at the ETC) and OCR were decreased, we hypothesized an inhibition of the ETC under HS. Nevertheless, this inhibition was not accompanied by an increase in H+ leak under HS, as shown in Figure 22. The metabolic uncoupling suggested is therefore not comparable to known pharmacologic mitochondrial uncoupling, where a dissipation of the

proton gradient is induced. Thus, we hypothesized that the mechanism of mitochondrial inhibition upon HS treatment was very distinct and presumably not a dissipation of the proton gradient.

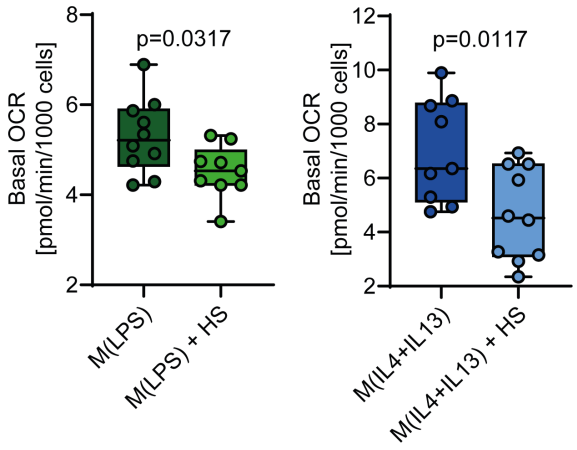

Figure 20: Basal OCR during the third hour of activation in M(LPS), M(LPS)+HS, M(IL4+IL13) and M(IL4+IL13)+HS macrophages. Three experiments with n=3-4 replicates per experiment were pooled. Data is depicted as mean ±SEM in boxplots with individual data points. Normality was determined by Kolmogorov-Smirnov test. Significance was analyzed by unpaired, two-tailed *t*-test.

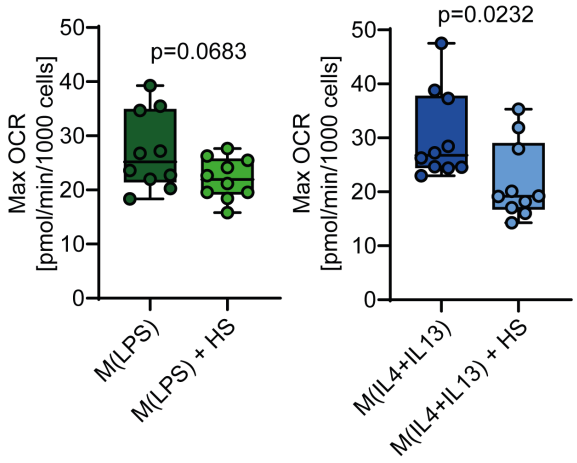

Figure 21: Maximal OCR during the third hour of activation in M(LPS), M(LPS)+HS, M(IL4+IL13) and M(IL4+IL13)+HS macrophages. Three experiments with n=3-4 replicates per experiment were pooled. Data is depicted as mean ±SEM in boxplots with individual data points. Normality was determined by Kolmogorov-Smirnov test. Significance of M(LPS) groups was analyzed by unpaired, two-tailed *t*-test. Significance of M(IL4+IL13) groups was analyzed by two-tailed Mann-Whitney test.

One major regulator of ETC function and thus mitochondrial respiration is the morphology and ultrastructure of mitochondria. There is a wide range of mitochondrial lengths, from short and rounded structures to long, interconnected mitochondrial networks. These different states mitochondria can be found in are determined by fission and fusion processes, accomplished by large guanosine triphosphatases (GTPases) from the dynamin family [91]. Fission is mediated by cytosolic Dynamin related protein 1 (DRP1), which is recruited by accessory proteins mitochondrial dynamics proteins of 49 and 51 kDa (MID49 and 51) and mitochondrial fission factor (MFF). Once recruited, DRP1

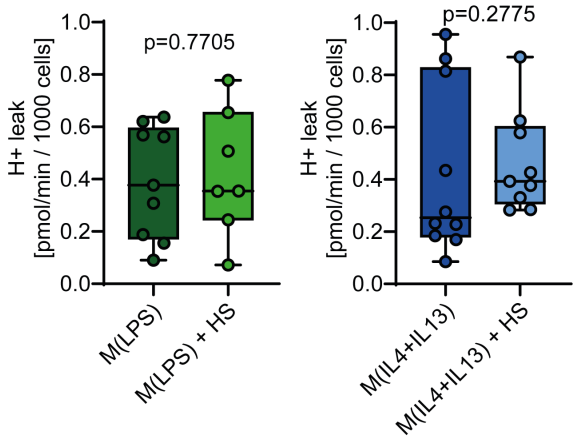

Figure 22: H+ leak during the third hour of activation in M(LPS), M(LPS)+HS, M(IL4+IL13) and M(IL4+IL13)+HS macrophages. Three experiments with n=3-4 replicates per experiment were pooled. Data is depicted as mean ±SEM in boxplots with individual data points. Normality was determined by Kolmogorov-Smirnov test. Significance of M(LPS) groups was analyzed by unpaired, two-tailed *t*-test. Significance of M(IL4+IL13) groups was analyzed by two-tailed Mann-Whitney test.

forms spirals around mitochondria, constricting both the inner and outer mitochondrial membrane. Fission is essential for proliferating cells, in order to produce new organelles and control the quality of mitochondria [91]. Fusion is mediated by mitofusin (MFN) 1 and 2 (anchored in the outer mitochondrial membrane) and optic atrophy 1 (OPA1) (in the inner mitochondrial membrane). High energetic demand stimulates mitochondrial fusion, as mitochondrial networks display higher OXPHOS rates than fissed mitochondria. Furthermore, fusion can reduce the effect of environmental stress and mitochondrial genetic mutations via the exchange of proteins and lipids among fused mitochondria [91]. With regards to immune cells, the group around Erika Pearce demonstrated that mitochondrial dynamics control T cell differentiation into effector or memory T cells. They suggested that mitochondrial fusion induces a reorganization and association of ETC complexes within mitochondrial cristae (i.e. the invaginations of the inner mitochondrial membrane) that favors OXPHOS. Thereby, mitochondrial fusion appeared to be crucial for long-lifed, OXPHOS-dependent memory T cell development [92].

As HS induced a significant inhibition of SDHA activity and decrease in mitochondrial respiration, while affecting macrophage activation, we asked whether mitochondrial morphology could play a role in this process. We speculated that mitochondrial fission/-fusion processes or cristae ultrastructure might be interfered with upon HS. In order to evaluate the impact of HS on mitochondrial morphology we performed TEM imaging in

collaboration with Prof. Dr. Thomas Bartolomaeus from the Institute for Evolutionary Biology and Ecology (IEZ) at the university of Bonn. We activated M(LPS) macrophages for 3h under NS or HS conditions. Subsequent cell washing, detaching and fixation was performed under equal tonicity with adjusted NS or HS buffers in order to minimize stress-induced artifacts. Figure 23 displays electron micrographs of two entire cells, as well as representative single mitochondria from NS and HS M(LPS) macrophages. Sequential imaging allowed three-dimensional (3D) reconstruction of mitochondrial distribution within cells, visualized in yellow in Figure 23. Interestingly, there were no visual signs of HS treatment, with both groups displaying similar mitochondrial morphology, ultrastructure and distribution. Based on this result, we concluded that HS impact on macrophage metabolism was not imposed by a change in mitochondrial dynamics.

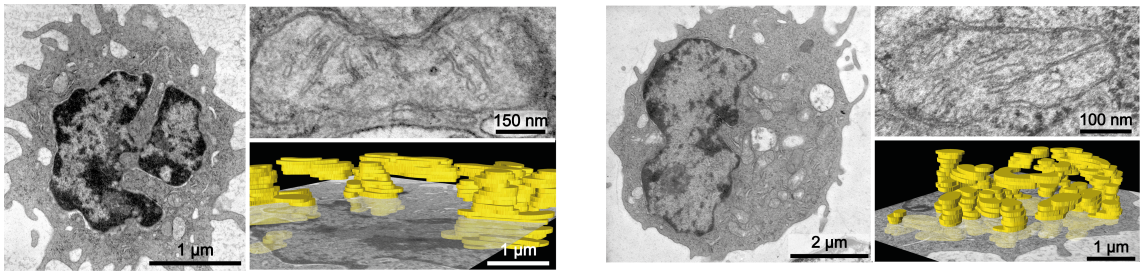

(a) Normal Salt **(b)** High Salt

Figure 23: Representative TEM images from M(LPS) activated for 3h under normal salt or high salt conditions. Electron micrographs depict an entire cell and a respective, representative mitochondrium. In yellow, a 3D reconstruction of the mitochondrial network in a representative section of the cell is shown.

As mitochondrial morphology was not affected by HS treatment, we wanted to dissect where at the ETC HS was affecting mitochondrial respiration. As a functional read-out and to confirm our Seahorse experiments, we evaluated ATP content of BMDM. We activated them to M(LPS) or M(IL4+IL13) for 3h under NS or HS conditions. Furthermore, as a positive control for ATP decrease, we treated M(LPS) and M(IL4+IL13) macrophages with the ATPase inhibitor oligomycin. As shown in Figure 24, HS induced a significant decay in ATP production, comparable to oligomycin treatment. This indicates a substantial metabolic obstruction and energetic collapse in macrophages activated under HS conditions.

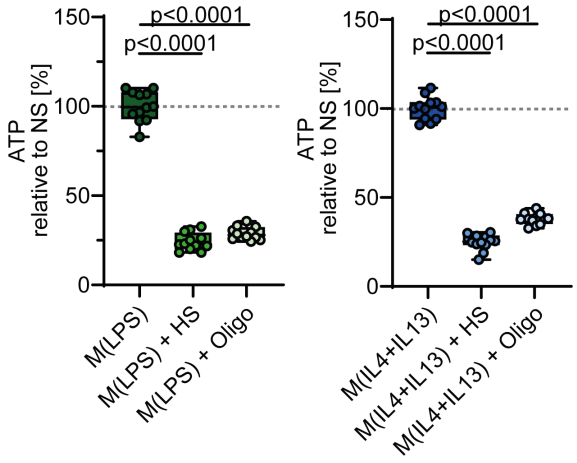

Figure 24: ATP content after three hours of activation in M(LPS) and M(IL4+IL13) macrophages, activated under normal or high salt (HS) conditions. Data is shown as percentage relative to the normal salt (NS) groups. As positive control for ATP decrease cells were treated with 10 µM oligomycin (Oligo). DMSO was used in all non-oligomycin groups as solvent control. Two experiments with n=6 replicates per experiment were pooled. Data is depicted as mean ±SEM in boxplots with individual data points. Normality was determined by Kolmogorov-Smirnov test. Significance was analyzed by one-way ANOVA and Tukey's post-hoc test.

Besides oxygen consumption and ultimately ATP production, another important parameter of intact ETC function is the membrane potential across the inner mitochondrial membrane. ETC complexes I, III and IV translocate protons from the mitochondrial matrix into the intermembrane space. This induces an electrochemical force, used at CV for ATP production. The net negative charge across a healthy mitochondrion is approximately -180mV, which can be detected by staining cells or mitochondria with positively charged dyes, such as TMRE. They intercalate in active mitochondria and emit red fluorescence. The fluorescence intensity is dependent on the proton content within the intermembrane space and thereby indicates whether a cell has a high or low transmembrane potential. In order to analyze the membrane potential and thus the proton-moving force of ETC CI, CIII and IV under high extracellular salt, we activated macrophages with LPS or IL4 and IL13 under NS and HS conditions for 3h. As positive control we used FCCP. The uncoupler dissipates the proton gradient and thereby induces mitochondrial depolarization. During the last hour of activation, MitoTracker Green staining was performed to normalize TMRE staining to total mitochondrial content. Figure 25 shows a representative flow cytometric histogram of TMRE in MitoTracker Green positive M(LPS) and M(IL4+IL13) macrophages. Mean fluorescence intensity (MFI) was calculated relative to NS controls (Figure 25). HS induced a significant decrease of TMRE fluorescence compared to NS in both M(LPS) ($p<0.0001$) and M(IL4+IL13) ($p=0.0028$).

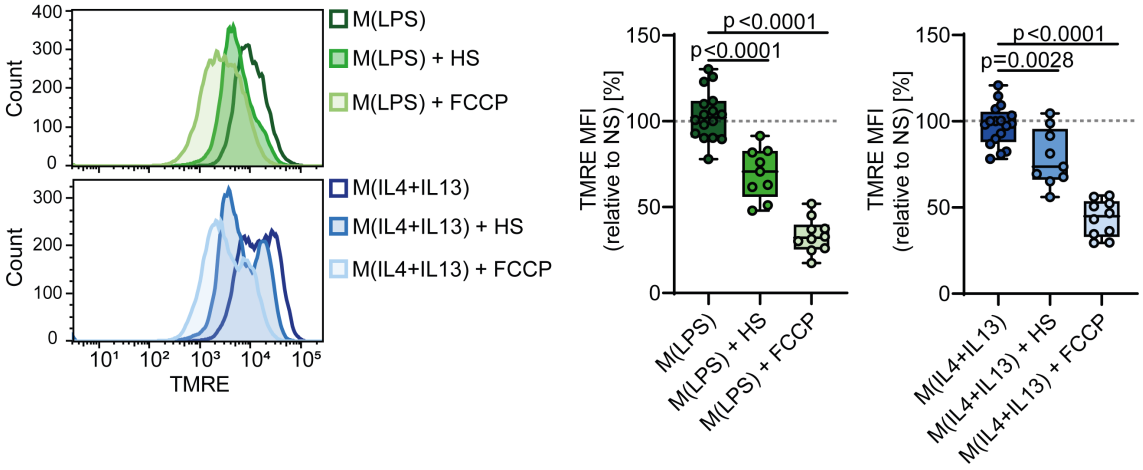

Figure 25: Mitochondrial membrane potential after 3h of activation in M(LPS) and M(IL4+IL13) macrophages, activated under normal or high salt (HS) conditions. Mitochondrial membrane potential was determined by flow cytometric analysis of TMRE mean fluorescence intensity (MFI). Representative histograms are depicted on the left. On the right, MFI is shown as percentage relative to normal salt (NS) groups. As positive control for mitochondrial depolarization cells were treated with 10 µM FCCP. DMSO was used in all non-FCCP groups as solvent control. Two experiments with n=5-10 replicates per experiment were pooled. Data is depicted as mean ±SEM in boxplots with individual data points. Normality was determined by Kolmogorov-Smirnov test. Significance was analyzed by one-way ANOVA and Tukey's post-hoc test.

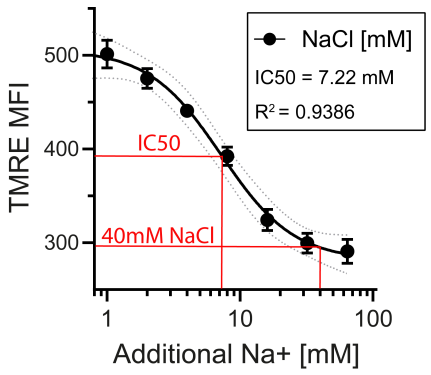

Figure 26: Mitochondrial membrane potential in isolated macrophage mitochondria, incubated with increasing concentrations of NaCl (serial dilutions from 64mM to 1mM NaCl). Mitochondrial membrane potential was determined by flow cytometric analysis of TMRE mean fluorescence intensity (MFI) with n=4 replicates per concentration. Mean ±SEM is shown for every NaCl concentration.

In order to validate this strong decrease of TMRE MFI seen in stimulated BMDM, we isolated mitochondria from BMDM and analyzed mitochondrial membrane potential under different concentrations of NaCl. Freshly isolated mitochondria were stained for 1h with MitoTracker Green (at 37° in respiration buffer, see chapter III.11) and for 20 min with TMRE. During the staining 64mM, 32mM, 16mM, 8mM, 4mM, 2mM, and 1mM of NaCl were added to the respiration buffer to mimic a respective increase in cytosolic Na^+ content. Figure 26 illustrates the TMRE MFI of isolated mitochondria in dependence of the additional Na^+ present in the respiration buffer. There was a sigmoidal relationship between TMRE MFI and added Na^+

(R^2=0.9386), where increasing amounts of NaCl induced a decrease of TMRE MFI. Taken together, these data demonstrate that HS treatment induces a depolarization of the inner mitochondrial membrane. This led us to speculate, that one or more of the proton-pumping complexes from the ETC are inhibited under HS conditions.

NADH is an electron carrier, connecting the TCA cycle and the ETC. NAD^+ is reduced to NADH during the conversion of citrate to 2-oxo-glutaric acid, of 2-oxo-glutaric acid to succinate, and of malate to oxaloacetate within the TCA cycle. Subsequently, NADH is oxidized at CI from the ETC. Based on our pSIRM data, showing intact TCA input (Figure 15 and Figure 16) and cycling until succinate (Figure 17 and Figure 18), we hypothesized that NADH production and CI function would not be affected by HS. To prove this concept, we quantified total NAD and NADH from BMDM activated for 3h to M(LPS) and M(IL4+IL13) under NS and HS conditions. Oxidized NAD^+ content can be calculated as the difference between total NAD and NADH. Rotenone inhibits CI, leading to an accumulation of NADH and a decrease in NAD^+-to-NADH ratio. Rotenone treatment was therefore included as positive control for CI inhibition. Figure 27 shows the ratio of NAD^+ to NADH. Whereas rotenone treatment induced a significant decrease in NAD^+-to-NADH ratio in both M(LPS) (p=0.0393) and M(IL4+IL13) (p=0.0133), HS treatment had no effect.

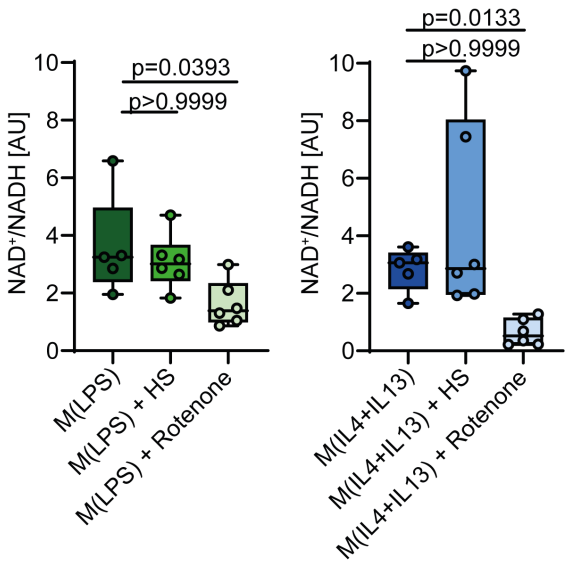

Figure 27: NAD^+/NADH ratio after three hours of activation in M(LPS) and M(IL4+IL13) macrophages, activated under normal or high salt (HS) conditions. As positive control for NADH accumulation and thus decrease in NAD^+/NADH ratio cells were treated with 10 µM rotenone. DMSO was used in all non-rotenone groups as solvent control. Each group was examined in n=5 replicates. Data is depicted as mean ±SEM in boxplots with individual data points. Normality was determined by Kolmogorov-Smirnov test. Significance was analyzed by Kruskal-Wallis test and Dunn's post-hoc test.

In order to corroborate this data, we performed a CI activity assay. BMDM lysate was used to immunocapture CI, followed by incubation with NADH and increasing concentrations of NaCl. The oxidation of NADH could then be detected and CI activity calculated relative to the NS control (Figure 28, grey dashed line represents NS). As shown in Figure 28, the addition of 0.0625mM, 0.125mM, 0.250mM, 0.5mM, 1mM, 2mM, 4mM, 8mM, 16mM, 32mM, and 64mM of NaCl did not inhibit CI activity compared to NS. Taken together these data demonstrate that HS has no effect on CI function in M(LPS) and M(IL4+IL13). Therefore, we concluded that the reduction in mitochondrial respiration seen under HS (Figure 20 and Figure 21) had to be originated by other means.

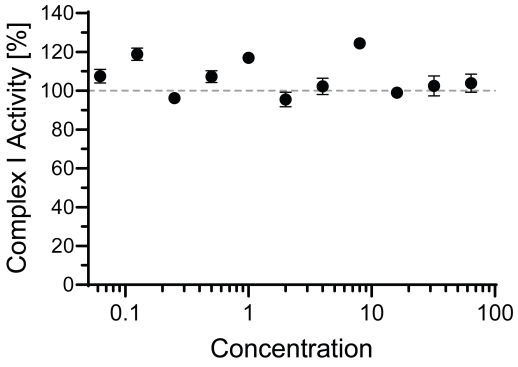

Figure 28: Complex I Assay. BMDM were lysed, complex I immunocaptured, and oxidation of NADH to NAD^+ measured under increasing concentrations of NaCl (serial dilutions from 64mM to 0.0625mM NaCl). Complex I activity was calculated relative to the normal salt condition (grey dashed line). Three replicates per group are shown as mean ±SEM.

Mitochondrial oxygen consumption takes place to the greatest extent at CIV. Proton translocation from the mitochondrial matrix to the intermembrane space is mostly conducted at CI, CIII and CIV. By excluding an HS-effect on CI and based on our pSIRM (Figure 15-18), Seahorse (Figure 20 and Figure 21) and mitochondrial membrane potential data (Figure 25 and Figure 26), we speculated, that HS inhibited the function of CIII or CIV. To test our hypothesis we performed a CII+CIII assay. Supplied mitochondria were incubated with succinate, cytochrome c, rotenone and potassium cyanide (KCN) under different NaCl conditions. Added succinate is oxidized to fumarate and electrons are subsequently transferred to cytochrome c by CIII. By adding rotenone, CI was inhibited and thus all cytochrome c reduction was performed by CII and CIII, not CI and CIII. The addition of KCN allowed the detection of increasing concentrations of reduced cytochrome c, as re-oxidation at CIV was inhibited. As positive control, increasing concentrations of CIII inhibitor AA were added. Figure 29 depicts CII+CIII

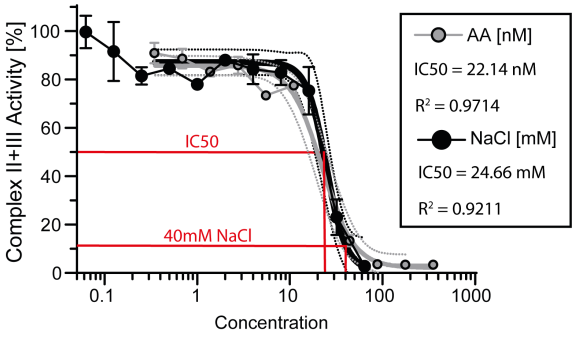

Figure 29: Complex II+III Assay. Bovine heart mitochondria were incubated with increasing concentrations of NaCl (serial dilutions from 64mM to 0.0625mM NaCl), succinate and oxidized cytochrome c. Complex II activity induces the oxidation of succinate to fumarate and complex III activity the subsequent reduction of cytochrome c. As positive control for complex III inhibition, antimycin A was used (in serial dilutions from 352nM to 0.3438nM). Complex II+III activity was calculated relative to the solvent control (water or DMSO, respectively). Each concentration was performed with n=3 replicates, shown as mean ±SEM.

activity relative to controls (DMSO for AA and NS for NaCl) in dependence of the added AA or NaCl. As shown, there was a sigmoidal relationship between CII+CIII activity and added Na^+ (R^2=0.9), where increasing amounts of NaCl induced a decrease of CII+CIII activity. The addition of only 0.125mM of NaCl led to a 10% and 0.250mM of NaCl to a 20% decrease in CII+CIII activity.

Our pSIRM data showed a significant decrease in SDHA activity (Figure 17 and Figure 18). The NaCl-dependent decrease in CII+CIII activity could thus lead to the conclusion, that HS might inhibit CII. However, proton translocation into the intermembrane space was also inhibited under HS, as shown by our TMRE data (Figure 25 and Figure 26). We thus hypothesized, that HS was having an inhibitory effect on CIII, leading to decreased mitochondrial membrane potential, decreased oxygen consumption at posterior CIV and (via an electron oversaturation of the ETC) decreased succinate to fumarate oxidation at anterior SDHA/CII. To test whether this CIII inhibition could mediate differential macrophage activation, we tested the effect of pharmacologic inhibtion of CIII (under NS) on macrophage marker gene expression. BMDM were activated towards M(LPS) and M(IL4+IL13) for 3h under NS and HS conditions, as well as CIII inhibition with AA. We performed TMRE staining and gene expression analysis in order to evaluate the effect of AA treatment on mitochondrial membrane potential and macrophage transcriptional activation. As shown in Figure 30, as for HS, AA treatment led to a significant decrease in TMRE MFI ($p<0.0001$ compared to NS in both M(LPS) and M(IL4+IL13)). More interestingly, relative gene expression of pro-inflammatory marker *Nos2* and anti-inflammatory marker *Retnla1* were down-regulated to a similar degree

than upon HS treatment (p<0.0001 compared to NS in both M(LPS) and M(IL4+IL13)). This data indicates that HS-induced inhibition of CIII is responsible for differential macrophage activation.

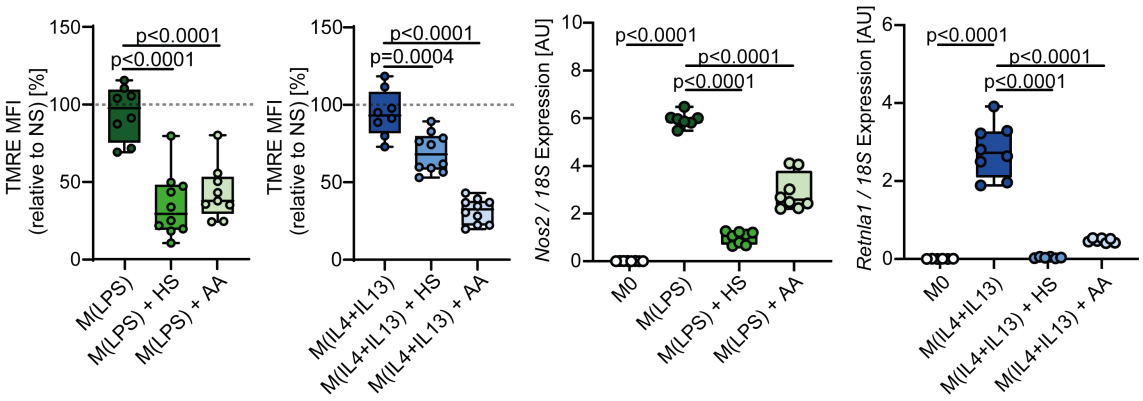

Figure 30: Mitochondrial membrane potential and macrophage marker gene expression under pharmacologic complex III inhibition. BMDM were activated for 3h into M(LPS) or M(IL4+IL13) under normal salt or high salt (HS) conditions. Pharmacologic complex III inhibition was performed by treatment with 10 µM antimycin A (AA). Mitochondrial membrane potential was determined by flow cytometric analysis of TMRE mean fluorescence intensity (MFI) and data are shown as percentage relative to normal salt (NS) groups. Two experiments with n=5 replicates per experiment were pooled. Normality was determined by Kolmogorov-Smirnov test. Significance was analyzed by Kruskal-Wallis test and Dunn's post-hoc test. For gene expression analyses, BMDM were treated equally, but unstimulated M0 macrophages were included. Expression of M1 marker *Nos2* and M2 marker *Rentla1* was normalized to 18S. Two experiments with n=4 replicates per experiment were pooled. Data is depicted as mean ±SEM in boxplots with individual data points. Normality was determined by Kolmogorov-Smirnov test. Significance was analyzed by one-way ANOVA and Tukey's post-hoc test.

As described earlier, HS induced a metabolic uncoupling, with intact TCA input (Figure 15 and Figure 16) and cycling until succinate (Figure 17 and Figure 18) but decreased mitochondrial respiration (Figure 20 and Figure 21) and ATP production (Figure 24). We thus asked, whether an uncoupling of ETC and TCA cycle would mediate the HS-effect on macrophage activation. To test this hypothesis we activated BMDM for 3h under NS and HS conditions, as well as pharmacologic uncoupling with BAM15. BAM15 dissipates proton gradient across the inner mitochondrial membrane, as does FCCP. It has been shown, however, that compared to FCCP BAM15 is more specific towards mitochondrial membrane depolarization. Based on our Seahorse data showing that proton leak was not increased by HS (Figure 22), we speculated that the uncoupling mechanism of BAM15 would be different from HS. However, we believed that the functional effect of metabolic uncoupling would be similar. As before, we performed

TMRE staining and gene expression analysis in order to evaluate the effect of BAM15 uncoupling on mitochondrial membrane potential and macrophage transcriptional activation. As shown in Figure 31, as for HS and FCCP (Figure 25), BAM15 treatment led to a significant mitochondrial depolarization ($p<0.0001$ compared to NS in both M(LPS) and M(IL4+IL13)). Furthermore, relative gene expression of *Nos2* and *Retnla1* were significantly down-regulated ($p<0.0001$ compared to NS in both M(LPS) and M(IL4+IL13)).

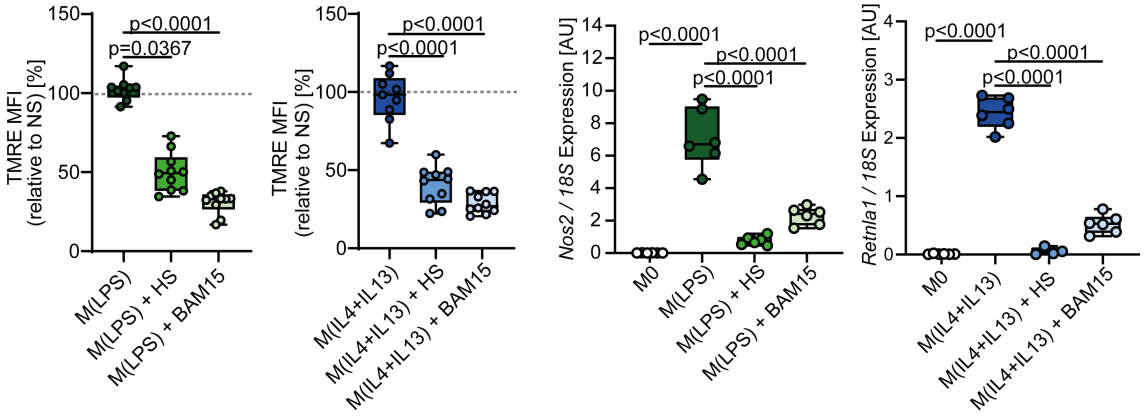

Figure 31: Mitochondrial membrane potential and macrophage marker gene expression under pharmacologic mitochondrial uncoupling. BMDM were activated for 3h into M(LPS) or M(IL4+IL13) under normal salt or high salt (HS) conditions. Pharmacologic uncoupling was performed by treatment with 10 µM BAM15. Mitochondrial membrane potential was determined by flow cytometric analysis of TMRE mean fluorescence intensity (MFI) and data are shown as percentage relative to normal salt (NS) groups. Two experiments with n=5 replicates per experiment were pooled. Data is depicted as mean ±SEM in boxplots with individual data points. Normality was determined by Kolmogorov-Smirnov test. Significance for M(LPS) groups was analyzed by Kruskal-Wallis test and Dunn's post-hoc test. M(IL4+IL13) groups were analyzed by one-way ANOVA and Tukey's post-hoc test. For gene expression analyses, BMDM were treated equally, but unstimulated M0 macrophages were included. Expression of M1 marker *Nos2* and M2 marker *Rentla1* was normalized to 18S. Two experiments with n=3 replicates per experiment were pooled. Normality was determined by Kolmogorov-Smirnov test. Significance was analyzed by one-way ANOVA and Tukey's post-hoc test.

In order to validate the impact of metabolic uncoupling on macrophage activation, we wanted to investigate the effect of BAM15 treatment on macrophage bacterial killing capacity. For this, in cooperation with Prof. Dr. Jonathan Jantsch from the Institute for Microbiology and Hygiene at the University of Regensburg (IMHR) we analyzed macrophage defense against *E.coli* bacteria after 3h of activation. Figure 32 represents the number of colony-forming units (CFU), determined 24h after macrophage lysis, i.e. the number of bacteria that had not been killed by activated M(LPS). Data is shown

relative to NS control. We confirmed previous data [86], showing that under HS the number of CFU was significantly lower (p=0.0041) than under NS conditions. Thus, HS increased bacterial killing capacity of M(LPS) macrophages. Interestingly, BAM15 treatment (under NS conditions) also boosted bacterial killing significantly (p=0.0054 compared to NS).

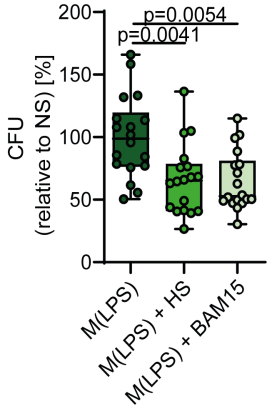

Figure 32: Bacterial killing capacity under pharmacologic mitochondrial uncoupling. BMDM were activated for 3h into M(LPS) under normal salt or high salt (HS) conditions. Pharmacologic uncoupling was performed by treatment with 10 µM BAM15. Simultaneously, cells were infected with *E. coli* bacteria. During the last 2h of activation, extracellular bacteria were killed with gentamycin treatment. Bacterial survival was assessed after lysis of macrophages and determination of colony-forming units (CFU). Three experiments with n=6 replicates per experiment were pooled and data shown as percentage relative to the normal salt (NS) group. Data is depicted as mean ±SEM in boxplots with individual data points. Normality was determined by Kolmogorov-Smirnov test. Significance was analyzed by Kruskal-Wallis test and Dunn's post-hoc test.

Taken together, we could demonstrate that HS treatment led to a significant mitochondrial dysfunction during early macrophage activation, with decreased mitochondrial respiration, mitochondrial membrane potential and ATP production. Glycolysis and TCA cycle, by contrast, were unaffected until the stage of succinate oxidation under HS. HS is thereby inducing an uncoupling of TCA cycle and OXPHOS. Pharmacologic inhibition of CIII as well as chemical mitochondrial uncoupling led to a similar effect on macrophage activation and function as HS treatment. Based on this data, we conclude that mitochondrial dysfunction and the resulting metabolic uncoupling might be a new mechanism by which HS differentially regulates macrophage phenotype.

In order to translate this finding into humans, we wondered if human monocytes would also show a mitochondrial dysfunction upon HS. Therefore, we isolated blood-derived monocytes from eight healthy volunteers. We treated freshly isolated monocytes with +40mM NaCl for 3h and measured OCR via Seahorse technology. Figure 33 shows basal OCR from HS-stimulated monocytes normalized to each donor's untreated monocytes. HS lead to a significant reduction in basal OCR (p=0.0078 compared to NS). This led us to conclude that *in vitro* HS treatment induced a mitochondrial dysfunction

species-independently in both, murine and human mononuclear phagocyte cells.

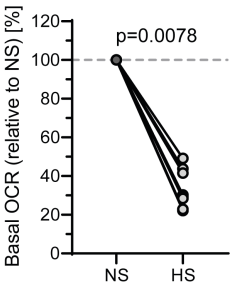

Figure 33: Basal OCR in human blood-derived monocytes stimulated with 40mM of NaCl. Monocytes were isolated out of PBMCs, treated for 3h with additional 40mM of NaCl (HS) and mitochondrial respiration analyzed by Seahorse technology. Data of eight healthy donors is shown as percentage, relative to each donor's normal salt (NS) monocytes. Normality was determined by Kolmogorov-Smirnov test. Significance was analyzed by two-tailed Wilcoxon matched-pairs signed rank test.

In order to evaluate whether HS also had an effect on monocytic mitochondrial function *in vivo* we re-evaluated a salt-intervention study previously performed in our laboratory. Dr. Nicola Wilck, in cooperation with Dr. Michael Boschmann and Dr. Anja Mähler from the Experimental & Clinical Research Center Berlin-Buch, recruited 14 participants to study the effects of an increased salt intake on metabolic, cardiovascular and immunoregulatory functions in healthy men (see Clinical Trials entry NCT02509962). From these 14 participants, PBMC samples from 8 participants could be analyzed within this thesis. During the study, participants ingested additional 6g of NaCl daily for 14 days. At baseline, after 3 and 14 days of salt-intervention and at day 28 (i.e. after 14 days of recovery), blood was collected to perform immunophenotyping and analyse salt-induced differences in immune cell subsets. Furthermore, at each time point postprandial energy expenditure after a defined meal was measured by indirect calorimetry (respiratory chamber) to evaluate HS-induced metabolic effects. From the remaining 8 participants we determined plasma Na^+, in order to investigate if a HS diet would increase Na^+ concentration in the blood. Furthermore, we isolated monocytes from PBMC samples and measured mitochondrial respiration by Seahorse technology. As shown in Figure 34, plasma Na^+ concentration increased significantly from baseline to day 3 by on average 2.125mM $\pm$SD=1.457mM (p=0.0050) and from baseline to day 14 by on average 1.25mM $\pm$SD=1.832mM (p=0.0155). At day 28, plasma Na^+ displayed a partial recovery with no significant change compared to baseline (p=0.0814). Basal OCR was determined for all time points and is represented as percentage relative to each participant's baseline. As shown in Figure 34, basal OCR decreased in all participants except for one during the high salt challenge. At

day 28, however, basal OCR showed a partial recovery as well. When analysing the relationship between the fold change in basal OCR and the delta in plasma Na^+ from each visit to baseline, we could show a significant negative correlation between both factors (r=-0.4709 and p=0.0382). All participants that exhibited an increase in plasma Na^+ displayed a decrease in their monocytic mitochondrial respiration, although to distinct degrees of course. Taken together, these data show that diet-induced increased in plasma Na^+ have an inhibitory effect on monocytic mitochondrial function.

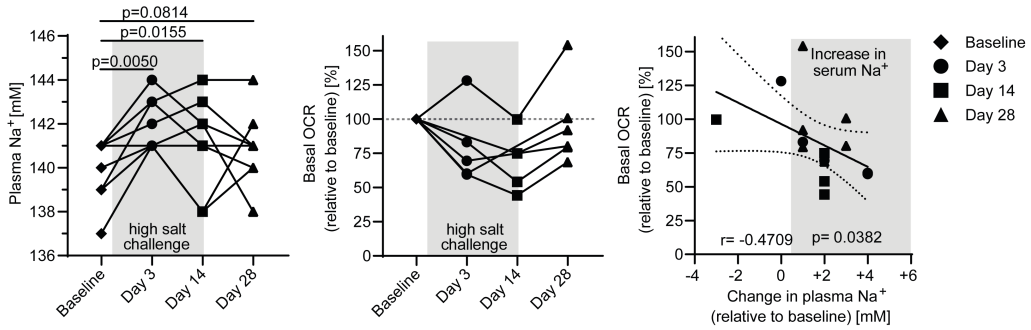

Figure 34: Plasma sodium (Na^+) and monocytic basal oxygen consumption rate (OCR) of a salt intervention study. Eight healthy volunteers underwent a high salt challenge with additional 6 g of NaCl daily during 14 days. Plasma Na^+ as well as basal OCR of blood-derived monocytes were assessed at baseline (prior the high salt challenge), at day 3 and 14 of the high salt challenge, and at day 28 (14 days post high salt challenge). Normality was determined by Kolmogorov-Smirnov test. Significance of plasma Na^+ was analyzed by Friedman test and FDR-correction was performed via Benjamini-Hochberg procedure. Relationship between the change in plasma Na^+ and the change in basal OCR (of all days compared to baseline) was determined by Pearson correlation and linear regression analysis.

As described above, plasma Na^+ increased from baseline to day 3 by on average 2.125mM, ranging from 0mM (in one participant) to 4mM. In order to validate that such small increases in extracellular Na^+ would induce a mitochondrial dysfunction in human monocytes, we isolated blood-derived monocytes from 20 healthy volunteers, 10 male and 10 female. Freshly isolated monocytes were treated with 2mM and 4mM of NaCl to mimic the diet-induced differences seen in our salt-intervention study. We then performed TMRE stainings to evaluate mitochondrial membrane potential, Seahorse assays to determine mitochondrial respiration, and intracellular ATP quantification. Figure 35, Figure 36 and Figure 37 depict TMRE MFI, basal OCR and ATP content, respectively, as percentage relative to NS monocytes in dependence of additional ex-

tracellular Na^+ for both male (in blue) and female (in red) participants. As shown in Figure 35, TMRE MFI correlated with additional Na^+ in both male (r=-0.5815 and p=0.0008) and female (r=-0.5334 and p=0.0024) donors. As shown in Figure 36, also basal OCR showed a significant negative correlation to added Na^+ in both male (r=-0.8266 and p<0.0001) and female (r=-0.6392 and p=0.0001) participants. Finally, ATP content further correlated with added Na^+ in both male (r=-0.5334 and p=0.0024) and female (r=-0.7351 and p<0.0001) donors. Taken together, these data demonstrate that a HS diet can induce changes in plasma Na^+. These small increases, although within the physiological range, can induce a mitochondrial dysfunction, with significant mitochondrial depolarization, decrease in mitochondrial respiration and decay in ATP production. Based on these results, we hypothesize that the mitochondrial dysfunction with subsequent metabolic uncoupling and impact on cell activation and function seen in murine macrophages under HS might also be true for human monocytes. Further we believe that dietary NaCl intake might thereby modulate monocyte metabolism and function.

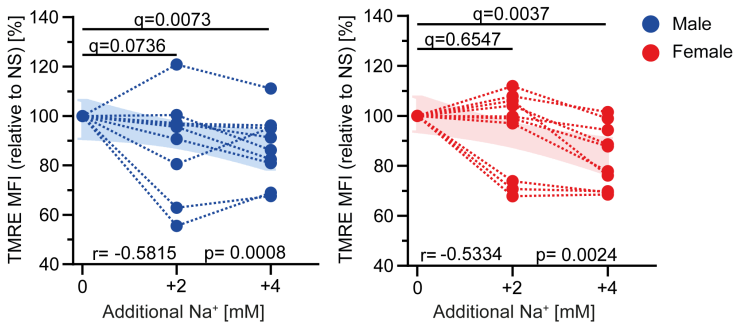

Figure 35: Mitochondrial membrane potential in human blood-derived monocytes stimulated for 3h with 2mM and 4mM of NaCl. Monocytes were isolated from blood-derived PBMCs from 10 healthy male and 10 healthy female volunteers. Mitochondrial membrane potential was determined by flow cytometric analysis of TMRE mean fluorescence intensity (MFI). Data is shown as percentage relative to normal salt (NS) controls. Normality was determined by Kolmogorov-Smirnov test. Relationship between the added Na^+ and TMRE MFI was assessed by Spearman correlation and linear regression analysis. Significance between the salt statuses was analyzed by Friedman test and FDR-correction was performed via Benjamini-Hochberg procedure.

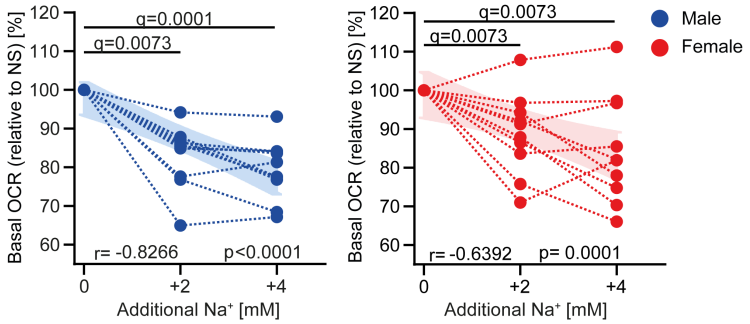

Figure 36: Mitochondrial oxygen consumption rate (OCR) in blood-derived monocytes stimulated for 3h with 2mM and 4mM of NaCl. Monocytes were isolated from blood-derived PBMCs from 10 healthy male and 10 healthy female volunteers. Data is shown as percentage relative to normal salt (NS) controls. Normality was determined by Kolmogorov-Smirnov test. Relationship between the added Na^+ and TMRE MFI was assessed by Spearman correlation and linear regression analysis. Significance between the salt statuses was analyzed by Friedman test and FDR-correction was performed via Benjamini-Hochberg procedure.

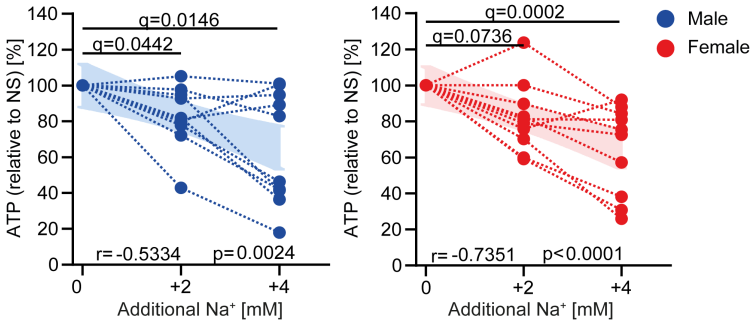

Figure 37: ATP content in blood-derived monocytes stimulated for 3h with 2mM and 4mM of NaCl. Monocytes were isolated from blood-derived PBMCs from 10 healthy male and 10 healthy female volunteers. Data is shown as percentage relative to normal salt (NS) controls. Normality was determined by Kolmogorov-Smirnov test. Relationship between the added Na^+ and TMRE MFI was assessed by Spearman correlation and linear regression analysis. Significance between the salt statuses was analyzed by Friedman test and FDR-correction was performed via Benjamini-Hochberg procedure.

V. Discussion

Sodium is the most important extracellular cation [71]. As previously described, sodium can accumulate in the extracellular space without commensurate water retention [73–81], leading to a hypertonic saline compartment. Immune cells activated under these hypertonic saline conditions show a differentially regulated gene expression, activation and function compared to normal salt (NS) controls [80, 82–87]. In detail, late-phase (i.e. 24h post activation) M(LPS) macrophages show higher expression of pro-inflammatory markers (such as *Nos2*), increased production of nitric oxide and enhanced parasitic killing capacity [80]. M(IL4+IL13) macrophages, on the other hand, display a reduced expression of anti-inflammatory markers (such as *Retnla1*) and inhibited T cell suppression capacity compared to their NS counterparts [87]. Interestingly, Neubert *et al.* could demonstrate that high salt (HS) affects macrophage activation to a much earlier time point already. M(LPS) macrophages activated under HS conditions exhibit boosted bacterial killing capacity after only 4h of activation [86]. While the at 24h sodium-boosted defense against protozoan parasite *Leishmania major* is mediated by an p38 mitogen-activated protein kinase (p38/MAPK) and nuclear factor of activated T cells 5 (NFAT5) dependent induction of *Nos2* expression and increased production of nitric oxide [80], this mechanism could not explain the early boosted bacterial killing. Production of bactericidal ROS was not induced at this early time point either [86], suggesting further mechanisms of macrophage regulation and function. Neubert *et al.* found that bacterial defense was associated with an induction of autophagy and autolysosomal targeting against *E.coli*. These were dependent on HIF1α activation and NFAT5 expression. Furthermore, they confirmed earlier results [87], showing that HS blunts AKT/mechanistic Target of Rapamycin (mTOR) signaling. However, the molecular mechanism for this differential signaling upon HS still remains elusive.

As in detail outlined before, one major impact factor on macrophage activation is the metabolic pathway they engage [2]. Previous work has shown that classic M1

macrophages are highly glycolytic after 24h of activation. Their TCA cycle and ETC are repurposed, away from energy production and towards the generation of pro-inflammatory mediators, nitric oxide and ROS. By contrast, alternative M2 macrophages were shown to depend on TCA cycling and mitochondrial respiration (fueled by glycolysis, glutaminolysis and FAO) for their ATP production. These, however, are 24h-data, where macrophage activation, cellular adaptation and metabolic reprogramming are already very advanced. Tan *et al*. were one of the first questioning this paradigm. They analyzed M(LPS) and M(IL4) macrophages after 6 h of activation and suggested a dynamic reliance of macrophages on different energy sources, depending on the activation phase they are in [43].

Therefore, we analyzed early macrophage transcriptional activation and could show that after only 3h most *classic* and *alternative* macrophage markers were significantly upregulated in M(LPS) and M(IL4+IL13), respectively, compared to unstimulated M0 macrophages. Also at only 3h we found a significant effect of HS on macrophage marker gene expression. Interestingly, in M(IL4+IL13) macrophages the effect of HS was identical to 24h data previously reported [87], with a significant downregulation of *alternative* marker genes compared to the NS situation. In M(LPS) macrophages, however, the situation was more complex. We confirmed the late-phase upregulation of *classic* markers reported elsewhere [80]. At 3h, by contrast, some M1 markers were upregulated, whereas others were downregulated. This made us curious to further investigate this early time point during macrophage activation. We hypothesized that HS was affecting the dynamics in macrophage activation by interfering with the metabolic rewiring ocurring at early stages of polarization. As not much is known about early macrophage metabolism, not even under NS conditions, we performed diverse metabolic analyses in order to evaluate different functional aspects. By pulse labelling with 13C-Glc and 13C-Gln we could evaluate the direction of 13C incorporation in more detail compared to cumulative labelling (e.g. PDHA versus PC activity). Furthermore, by using both 13C-Glc and 13C-Gln we could distinguish between glycolytic flux-dependent and independent TCA cycling. For the investigation of OXPHOS, fueled by the TCA cycle, we performed real-time analysis of OCR via Seahorse technology. We

complemented this analysis with the quantification of intracellular ATP (as energetic output of OXPHOS) and determination of mitochondrial membrane potential (as read-out for functioning proton translocation within the ETC). By adapting all protocols, we could perform all experiments under exact same conditions. This is often not taken into account for. Specially changes of medium and medium type with subsequent changes in metabolite availability is a problem when comparing different experimental read-outs. The adaptation of all of our protocols allowed us to compare the different aspects of macrophage metabolism without media composition or time-dependent influences.

By tracing with 13C-Glc we could follow the break-down of glucose into lactate or it's entry into the TCA cycle via citrate and malate. We could not detect any differences in lactate production after 3h among all groups. Only after 24h we observed a significant increase in 13C-Lactate in M(LPS), but not in M(IL4+IL13) macrophages. HS did not change this phenotype compared to the NS situation. This contrasts a very recent report in the *Journal of Immunology*, where Rodríguez-Prados *et al.* compared glucose consumption and lactate production after 1 to 4h and 4 to 12h between seven different macrophage stimulations. They could show an increase in lactate production during the first 4h of activation in LPS-stimulated compared to unstimulated macrophages. However, this data is difficult to compare to other literature as well as to our situation, as they did not differentiate macrophages from bone-marrow cells but rather isolated peritoneal macrophages. The latter have been shown to be much more diverse and inhomogeneous compared to BMDM. There exist small and large peritoneal macrophages (SPM and LPM, respectively), with very different surface markers, cytokine expression and *in vivo* function [93]. Whereas SPMs display a pro-inflammatory functional profile, LPMs play a role in the maintenance of physiological conditions of the peritoneal cavity [93]. It is important to note that besides using peritoneal macrophages, the group injected thioglycollate 4 days prior the isolation of macrophages. Thioglycollate injection is known to yield primarily SPMs and inflammatory monocytes [93, 94]. The macrophages used for the study of Rodríguez-Prados *et al.* were thus pre-primed towards pro-inflammatory macrophages. A much faster reaction and metabolic adaptation upon LPS stimulation compared to unstimulated BMDM is therefore not surprising.

Besides lactate, we also analysed glucose-derived 13C incorporation into the TCA cycle. M1 macrophages are known to accumulate citrate after 24h, as it is used for the production of pro-inflammatory mediators [51], described in detail in chapter I.2. As HS boosted early M(LPS) *E.coli* killing as well as M1 marker gene expression in M(IL4+IL13), one could speculate that the induction of citrate could mediate this pro-inflammatory phenotype. We could show, however, that this was not the case in the first hours of activation, as glycolytic input into the TCA cycle was not changed by HS, neither in M(LPS) nor in M(IL4+IL13).

In order to analyze TCA cycling independently of glycolytic influx, we performed 13C-Gln tracing experiments. As described above, succinate accumulation is – similar to citrate accumulation – an important feature of 24h activated *classic* macrophages, as it serves as a pro-inflammatory mediator [42]. Furthermore, succinate supports HIF1α activation, which in turn Neubert *et al.* showed to be boosted under HS. It was therefore tempting to speculate, that HS could induce an accumulation of succinate, thereby activate HIF1α and modulate macrophage activation. However, as shown in Figure 17 and Figure 18, succinate levels were unchanged after 3h under HS compared to NS conditions. Interestingly, both M(LPS) and M(IL4+IL13) macrophages displayed decreased levels of 13C-Fumarate and a significantly inhibited SDHA activity. Taken together, our metabolomic analyses suggest that anaerobic glycolysis as well as TCA influx (both glycolytic and glutaminolytic) are not affected by HS after 3h of macrophage activation. By contrast, with a significantly decreased SDHA activity, we hypothesized that ETC might be inhibited by HS at CII or beyond. To test this hypothesis we analyzed mitochondrial respiration via Seahorse technology. OXPHOS has been shown to be the major energetic pathway in *alternative* macrophages after 24h. Huang *et al.* compared OCR and ECAR in M(LPS+IFNγ) and M(IL4) macrophages. They demonstrated that while ECAR was higher in M(LPS+IFNγ), OCR to ECAR ratio was 9-fold higher in M(IL4) after 24h [44]. Surprisingly enough, we detected similar levels of both basal and maximal OCR in M(LPS) and M(IL4+IL13) at 3h. As for our pSIRM data, this indicates that macrophage metabolic reprogramming is a dynamic process, dependent of activation time and cytokines. Pathways important at 24h in one subset or the other

are most probably not exclusive, but rather important at different stages of activation. With regards to the salt status, we could determine significant decreases in basal and maximal OCR upon HS treatment in both groups. We confirmed this data by measuring intracellular ATP and mitochondrial membrane potential. In both M(LPS) and M(IL4+IL13) macrophages HS led to a significant decrease in ATP production and TMRE MFI. Together, these data demonstrate a severe mitochondrial dysfunction and energetic collapse under HS. Interestingly, reduced mitochondrial respiration in HS macrophages has previously been reported by Ip *et al.*, although at much higher concentrations of NaCl [95]. They detected higher numbers of MitoTracker Green^{+} MitoTracker DeepRed^{low} macrophages under HS treatment. Whereas MitoTracker Green stains all mitochondria and thus serves as internal normalization, MitoTracker DeepRed only stains respiring mitochondria. Hence, an increase in MitoTracker Green^{+} MitoTracker DeepRed^{low} cells translates into reduced mitochondrial respiration. Our data is in agreement with Ip *et al.*, although they used 2.5-times our NaCl concentration. Interestingly, they used unstimulated M0 macrophages. This raises the question whether we would also see a functional impact of HS on M0 macrophages, knowing that Ip *et al.* reported similar metabolic features.

Moreover, our Seahorse, ATP and TMRE results contrast to the previously described unaffected TCA influx, shown by our pSIRM experiments. Whereas there was no difference in glucose- and glutamine-derived input into the TCA cycle, the outcome at the ETC in the form of OXPHOS was significantly inhibited under HS. In other words, HS induced a metabolic uncoupling of TCA cycle and OXPHOS. OXPHOS uncoupling in macrophages was also described by Mills *et al.* as a pro-inflammatory mechanism. They found that succinate was converted to fumarate without subsequent ATP production, as electrons released during this process were used at CI for the production of ROS and HIF1α activation [64]. However, this process was accompanied by increased mitochondrial membrane potential, which we did not detect under HS. Furthermore, as described by Neubert *et al.*, HS does not induce ROS after 4h. The presented mechanism might thus not overlap with HS-induced mitochondrial uncoupling. Sanin *et al.*, on the other hand, analyzed mitochondrial membrane potential in prostaglandin

E-stimulated M(IL4) [96] and found similar results to ours. They reported decreased OCR, mitochondrial membrane potential, and ATP production [96]. These parameters correlated with decreased expression of *Retnla1*, as we showed too, but were independent of mitochondrial ROS production, as Neubert *et al.* reported. However, TCA cycle intermediates (including citrate, malate and succinate), by contrast to our HS-induced phenotype, were also decreased in their setting. Prostaglandin E did therefore induce a mitochondrial dysfunction in M(IL4) but without mitochondrial uncoupling as HS treatment did [96]. Nevertheless, there seems to be a mitochondrial membrane potential-dependent nuclear gene expression, regulating macrophage activation accordingly. Sanin *et al.* suggested the name *voltage-dependent genes*. Finally, they found the transcription factor E twenty-six (ETS) variant 1 (ETV1) to play a role in sensing mitochondrial membrane potential and regulating a big subset of these *voltage-dependent genes* in M(IL4) [96]. Analysing this transcription factor in the HS situation in both M(LPS) and M(IL4+IL13) could therefore be very promissing.

In order to find out where exactly HS was inhibiting the ETC we conducted different ETC complex activity assays. As we had anticipated, CI activity was not affected by HS (Figure 28). We confirmed this data by determining intracellular NAD^+ and NADH. Under CI inhibition, NAD^+ to NADH ratio decreases, as CI cannot use NADH. This was however not the case for M(LPS) and M(IL4+IL13) macrophages activated under HS. CII+CIII activity assay in isolated (bovine) mitochondria, by contrast, showed a dependency of CII+CIII activity on NaCl concentration. Taking into consideration that mitochondria depolarized upon HS treatment, i.e. proton translocation from the matrix into the intermembrane space was inhibited, we hypothesized that CII-inhibition could not be the site of HS-impact. To corroborate this hypothesis, oxidation of $FADH_2$ to FAD at CII will be monitored in the future under increasing concentrations of NaCl. Still, when activating macrophages under pharmacologic CIII inhibition with AA, we could mimic HS-induced gene expression of *Nos2* and *Retnla1*. Similarly, AA treatment of RAW264.7 cells (a monocyte/macrophage cell line) increased phagocytosis of *C. albicans* without boosted production of nitric oxide [97], supporting the idea of increased pro-inflammatory macrophage function under CIII inhibition. Based on these

data, we deduce that mitochondrial dysfunction and the resulting metabolic uncoupling of TCA cycle and OXPHOS might be a new mechanism by which HS differentially regulates early macrophage activation and function.

In a translational approach we re-analysed a salt-intervention study, in which participants were exposed a high salt challenge of additional 6g of NaCl daily for 14 days. By isolating blood-derived monocytes from before, during and after the high salt challenge we could investigate the effect of a high salt diet on monocytic mitochondrial respiration. We found a significant increase in plasma Na^+ levels at day 3 and day 14 of the high salt challenge compared to baseline. Furthermore, 14 days after the high salt challenge, plasma Na^+ had returned to baseline. Strikingly, changes in basal OCR in isolated monocytes over the course of the study displayed a significant negative correlation with the differences detected in plasma Na^+. Diet-induced increase in plasma Na^+ has been reported previously [98, 99]. Suckling *et al.* performed a study in which healthy volunteers ingested a soup with or without 6g of NaCl. Changes in plasma Na^+ were measured every 15 min over the course of 4h. During the first hour after soup intake, there was a continuous increase in plasma Na^+ in the salty soup group which then plateaued and only slowly decreased after 3h. Mean plasma Na^+ increase after 2h was of 2.12mM $\pm$SEM=0.46mM and thus very similar to our results [98]. Yi *et al.*, on the other hand, reported a study with fixed sodium intake of 12g, 9g, and 6g daily over 30 to 60 days each [100]. They performed peripheral leukocyte phenotyping during each phase and interestingly found a decrease in monocytic anti-inflammatory, but an increase in pro-inflammatory cytokine release with increasing salt intake [100]. Taken together, these data suggest that dietary salt intake can lead to small but significant increases in plasma Na^+. These in turn affect mitochondrial metabolism and might modulate monocyte function *in vivo*. Based on this hypothesis we are planning to investigate monocyte metabolism and function upon a high salt meal challenge. We want to evaluate monocytic mitochondrial respiration, membrane potential and ATP production, as well as pro- and anti-inflammatory cytokine release before, 3h and 8h after a salty meal in ten male and ten female participants (ClinicalTrials entry NCT04175249). These data will give us insight into how fast nutrition might modulate

short-term monocyte metabolism and function.

V.1. Limitations and Outlook

Besides monocytes and macrophages, the question arises whether other immune cells display a mitochondrial dysfunction and metabolic uncoupling upon HS as well. As outlined in chapter I.3, also T_H-17 cells, T_H-2 cells and FOXP3$^+$ regulatory T cells were shown to be regulated by HS. It would thus be intriguing to investigate if a common mechanism underlies these HS-induced phenotypes. Supporting this idea are reports showing decreased mitochondrial function upon increased intracellular Na^+ in totally different settings. Iwai *et al.* reported that, upon ischemia, rat myocardium displayed higher intracelullar Na^+ content which correlated with decreased mitochondrial function [101]. Furthermore, they could show that isolated cardiac mitochondria incubated at different NaCl concentrations exhibited decreased oxygen consumption, ATP production and mitochondrial membrane potential [101]. In a later study, the same group reported that the increase in intracellular Na^+ was dependent on ischemia duration. Additionally, they could demonstrate that Na^+ not only entered the cells, but also a significant increase in intramitochondrial Na^+ was detectable. The latter could be prevented with the mitochondrial Na^+/Ca^{2+} exchanger inhibitor CGP37157 [102]. These data raise several questions:

First, if mitochondrial salinization might be a mechanism by which cells regulate their mitochondrial metabolism. From an evolutionary perspective, human dietary salt intake has changed dramatically in relatively short time. Similar to all species, contemporary humans are genetically adapted to the environment of their ancestors and therefore programmed for a very restricted salt intake [103]. With the introduction of agriculture and animal husbandry approximately 10000 years ago, by contrast, salt intake steadily increased to the point that a typical contemporary western diet includes almost 10g of NaCl daily. About 75% of the latter are derived from food processing and only

10% come from the actual foodstuffs [103]. Naturally, salt content is the highest in animal products [103]. Hence, the development of a strategic response upon this rare stimulus, specially an immune response, might be possible. If overall this response is beneficial or not, however, remains elusive. On one hand, salt seems to be boosting pro-inflammatory cells and therefore host defense against pathogens. On the other hand, increased salt intake correlates with cardiovascular and metabolic diseases [103]. Further investigation into the impact of salt, if any, on other cell types is therefore needed.

This leads to the second question, as to what cell types and tissues display an HS-impact on mitochondrial metabolism. In relation to diet-induced increase in plasma Na^+ one could not only think about other immune cells, but also endothelial cells. These are, as shown elsewhere [99, 104–106], highly sensitive to extracellular Na^+ concentration. Upon increasing Na^+ (within the physiological range) endothelial cells release less nitric oxide and become more stiff [99, 104, 106]. Thereby they can control local tissue perfusion and are important players in ischemia and cardiovascular diseases [104, 106]. Additionally, pro-inflammatory mediators (such as vascular cell adhesion protein 1 (VCAM1), E-selectin and the chemoattractant C-C motif chemokine ligand 2 (CCL2)) are up-regulated in endothelial cells cultivated under HS conditions, threby promoting atherosclerosis [105]. In this context, the degree of salt-sensitivity is an interesting aspekt. Maybe first line defense cells, such as monocytes, display a greater sensitivity against increasing concentrations of salt. We could show that already 2mM of NaCl inhibited monocytic mitochondrial function. Endothelial cells or cells from the adaptive immune system, however, might only react to longer or higher exposure to salt.

Finally, the question arises as to how and how much Na^+ enters a cell and, even further, a mitochondrium. Measuring Na^+ entry was beyond the scope of this dissertation, which is why we used increasing concentrations for our experiments in isolated mitochondria, for example. However, this will be of future interest in order to better disect salt-sensitivity of cells. Furthermore, we want to analyse if inhibition of different Na^+ transporters (both at the plasma and at the inner mitochondrial membrane) could

reverse metabolic, transcriptional and functional impact of HS on macrophages and monocytes.

Last but not least and coming back to Neubert *et al.*, we have not adressed the question as to if and how the mitochondrial dysfunction identified by us might be associated with the induction of autophagy identified by them under HS [86]. Mitochondria are recycled by autophagic processes (namely, mitophagy) and mitochondrial function highly depends on correct and balanced biogenesis and degradation [107]. Interestingly, also *vice versa* mitochondria regulate autophagic induction. The central autophagy-regulating pathways, AMPK and mTOR, are controlled by energy levels. Loss of mitochondrial ATP production can thus induce autophagy in an mTOR/AMPK-dependent manner [107–111]. Also autophagosomal membranes, whose origins remain under debate, might be regulated by mitochondrial function. Hailey *et al.* revealed that during starvation the membranes of autophagosomes and mitochondria are in continuity, allowing the transfer of a mitochondrial outer membrane marker into nascent autophagosomes [107, 112]. Strappazzon *et al.* identified activating molecule in Beclin-1 regulated autophagy (AMBRA-1) as a potential candidate regulating this process. They found that under nutrient-rich conditions autophagy-regulating Beclin-2 interacts simultaneously with AMBRA-1 at the mitochondrial surface and Beclin-1 at the endoplasmic reticulum and inhibits autophagy. Upon starvation, however, Beclin-2 dissociated from AMBRA-1, leading to AMBRA-1/Beclin-1 complex formation and autophagosomal biogenesis from mitochondrial membranes [107, 113]. Analysing AMPKA and AMBRA-1 signaling might therefore be of future interest in order to better understand intracellular HS cascade.

List of Abbreviations

2OG	2-oxo-glutaric acid
3D	three-dimensional
13C	carbon-13 isotope
18S	18 Svedberg units ribosomal RNA, gene
A2R	A2 adenosine receptor
AA	antimycin A
ACLY	ATP-citrate lyase
ACOD1	aconitate decarboxylase 1
ADP	adenosine diphosphate
AMBRA-1	activating molecule in Beclin-1 regulated autophagy
AMP	adenosine monophosphate
AMPK	AMP-activated protein kinase
AP	activator protein
ARG1	arginase 1, protein
Arg1	arginase 1, gene
ATP	adenosine triphosphate
BAM15	N^5,N^6-bis(2-fluorophenyl)-[1,2,5]oxadiazolo[3,4-b]pyrazine-5,6-diamine
BMC	bone marrow cells
BMDM	bone marrow-derived macrophages, also M0 macrophages
BSALT	salt-intervention study
CI	ETC complex I
CII	ETC complex II
CIII	ETC complex III
CIV	ETC complex IV
CV	ETC complex V
Ccl5	C-C motif chemokine ligand 5, gene
CCL2	C-C motif chemokine ligand 2

CCM	central carbon metabolism
CD	cluster of differentiation
cDNA	complementary DNA
CFU	colony-forming units
Chil3	chitinase-like protein 3, gene
CIC	citrate carrier
Cit	citrate
CoA	coenzyme A
CoQ	coenzyme Q, also ubiquinone
Cox2	Cyclooxygenase 2, gene
CPT1	carnitine palmitoyltransferase 1
CSF-1	colony stimulating factor 1
DNA	deoxyribonucleic acid
DRP1	dynamin related protein 1
ECAR	extracellular acidification rate
EGF	endothelial growth factor
ETC	electron transport chain
ETS	E twenty-six
ETV1	ETS variant 1
FAD	oxidized flavin adenine dinucleotide
$FADH_2$	reduced flavin adenine dinucleotide
FAO	fatty acid oxidation
FBS	fetal bovine serum
FC	fold change
FCCP	carbonyl cyanide 4-(trifluoromethoxy)phenylhydrazone
FeS	iron sulfur
FOXP3	forkhead box P3
Fum	Fumarate
Glc	glucose
Gln	glutamine
Glu	glutamic acid

GLUT1	glucose transporter 1
GPR91	G-protein-coupled receptor 91
GTP	guanosine triphosphate
HEPES	2-(4-(2-Hydroxyethyl)-1-piperazinyl)-ethansulfonsäure
HIF1α	hypoxia-inducible factor 1 α, protein
Hif1α	hypoxia-inducible factor 1 α, gene
HS	high salt
IDH	isocitrate dehydrogenase
IFNγ	interferon γ
IGF	insulin-like growth factor
IL	interleukin
IMS	intermembrane space
iNOS	inducible nitric oxide synthase
Irf4	interferon regulatory factor 4, gene
Irf5	interferon regulatory factor 5, gene
IRG	immune-responsive gene 1
JAK	Janus kinase
KEGG	Kyoto Encyclopedia of Genes and Genomes
Lac	lactate
LDHA	lactate dehydrogenase, protein
Ldha	lactate dehydrogenase, gene
LPM	large peritoneal macrophage
LPS	lipopolysaccharide
M(LPS)	LPS-activated macrophages
M(IL4)	IL4-activated macrophages
M(IL4+IL13)	IL4- and IL13-activated macrophages
m/z	mass-to-charge ratio
M0	unstimulated macrophage, also BMDM
M1	pro-inflammatory classic macrophages
M2	anti-inflammatory / pro-resolving macrophages
Mal	malate

MFF	mitochondrial fission factor
MFI	mean fluorescence intensity
MFN	mitofusion
Mgl2	macrophage galactose N-acetyl-galactosamine specific lectin 2, gene
MID49	mitochondrial dynamics protein 49 kDa
MMP	matrix metalloprotease
Mrc1	mannose receptor C-type 1, gene
mRNA	messenger ribonucleic acid
MRI	magnetic resonance imaging
MSTFA	N-methyl-N-[trimethylsilyl]trifluoroacetamide
mTOR	mechanistic target of Rapamycin
mTORC1	mTOR complex 1
NAD	nicotinamide adenine dinucleotide
NAD+	oxidized nicotinamide adenine dinucleotide
NADH	reduced nicotinamide adenine dinucleotide
NADPH	nicotinamide adenine dinucleotide phosphate
NFAT5	nuclear factor of activated T-cells 5, also TonEBP
NFκB	nuclear factor kappa-light-chain enhancer of B-cells
Nlrp3	NLR Family Pyrin Domain Containing 3, gene
NO	nitric oxide
Nos2	nitric oxide synthase 2, gene
NS	normal salt
OAA	oxaloacetate
OCR	oxygen consumption rate
Oligo	oligomycin A
OPA1	optic atrophy 1
OXPHOS	oxidative phosphorylation
p38/MAPK	p38 mitogen-activated protein kinase
PBMC	peripheral blood mononucleated cell
PC	pyruvate carboxylase, protein

Pcx	pyruvate decarboxylase, gene
PCR	polymerase chain reaction
PDGF	platelet-derived growth factor
PDHA	pyruvate dehydrogenase, protein
Pdha	pyruvate dehydrogenase, gene
PDK1	pyruvate dehydrogenase kinase 1
PKB	protein kinase B, also Akt
PPAR	peroxisome proliferator-activated receptor
PPARGC1B / PGC-1beta	PPAR gamma coactivator 1-beta
PPP	pentose phosphate pathway
PRR	pattern recognition receptor
pSIRM	pulsed stable isotope-resolved metabolomics
Pyr	pyruvate
QH2	ubiquinol
qPCR	quantitative real-time PCR
RET	reverse electron flow
Retnla1	resistin like α, gene
RNA	ribonucleic acid
ROS	reactive oxygen species
Rot	rotenone
SDHA	succinate dehydrogenase, protein
Sdha	succinate dehydrogenase, gene
SEM	standard error of the mean
SGK1	serum glucocorticoid-regulated kinase 1
Slamf1	signaling lymphocytic activation molecule family member 1, gene
SLC25A10	solute carrier family 25 member 10
SPM	small peritoneal macrophage
SRC	spare respiratory capacity
STAT	signal transducer and activator of transcription
Suc	succinate

TEM	transmission electron microscopy
TCA	tricarboxylic acid
TF	transcription factor
TGF	transforming growth factor
T_H	T helper cell
TLR	Toll-like receptor
TMRE	tetramethylrhodamine ethyl ester perchlorate
TNF	tumor necrosis factor, protein
Tnf	tumor necrosis factor, gene
TonEBP	tonicity enhancer binding protein, also NFAT5
VCAM1	vascular cell adhesion protein 1
VEGF-A	vascular endothelial growth factor A

List of Figures

References

1. Tauber, A. I. Immunity: How Elie Metchnikoff Changed the Course of Modern Medicine by Luba Vikhanski. *Bulletin of the History of Medicine* **91,** 140–142 (2017).

2. Viola, A., Munari, F., Sánchez-Rodríguez, R., Scolaro, T. & Castegna, A. The Metabolic Signature of Macrophage Responses. *Frontiers in Immunology*. doi:`https://doi.org/10.3389/fimmu.2019.01462` (2019).

3. Jha, A. K., Huang, S. C.-C., Sergushichev, A., Lampropoulou, V., Ivanova, Y., Loginicheva, E., Chmielewski, K., Stewart, K. M., Ashall, J., Everts, B., Pearce, E. J., Driggers, E. M. & Artyomov, M. N. Network Integration of Parallel Metabolic and Transcriptional Data Reveals Metabolic Modules that Regulate Macrophage Polarization. *Immunity* **42,** 419–430 (Mar. 2015).

4. Martinez, F. O. & Gordon, S. The M1 and M2 paradigm of macrophage activation: time for reassessment. *F1000Prime Reports* **6.** doi:`10.12703/p6-13` (Mar. 2014).

5. McGettrick, A. F. & O'Neill, L. A. J. How Metabolism Generates Signals during Innate Immunity and Inflammation. *Journal of Biological Chemistry* **288,** 22893–22898 (June 2013).

6. Xue, J., Schmidt, S. V., Sander, J., Draffehn, A., Krebs, W., Quester, I., Nardo, D. D., Gohel, T. D., Emde, M., Schmidleithner, L., Ganesan, H., Nino-Castro, A., Mallmann, M. R., Labzin, L., Theis, H., Kraut, M., Beyer, M., Latz, E., Freeman, T. C., Ulas, T. & Schultze, J. L. Transcriptome-Based Network Analysis Reveals a Spectrum Model of Human Macrophage Activation. *Immunity* **40,** 274–288 (Feb. 2014).

7. Zhu, L., Zhao, Q., Yang, T. & Ding, W. Cellular Metabolism and Macrophage Functional Polarization. *International Reviews of Immunology*. doi:`https://doi.org/10.3109/08830185.2014.969421` (2014).

8. Mosser, D. M. & Edwards, J. P. Exploring the full spectrum of macrophage activation. *Nature Reviews Immunology* **8,** 958–969 (Dec. 2008).

9. Hashimoto, D., Chow, A., Noizat, C., Teo, P., Beasley, M. B., Leboeuf, M., Becker, C. D., See, P., Price, J., Lucas, D., Greter, M., Mortha, A., Boyer, S. W., Forsberg, E. C., Tanaka, M., van Rooijen, N., Garcia-Sastre, A., Stanley, E. R., Ginhoux, F., Frenette, P. S. & Merad, M. Tissue-Resident Macrophages Self-Maintain Locally throughout Adult Life with Minimal Contribution from Circulating Monocytes. *Immunity* **38,** 792–804 (Apr. 2013).

10. Hoeffel, G., Wang, Y., Greter, M., See, P., Teo, P., Malleret, B., Leboeuf, M., Low, D., Oller, G., Almeida, F., Choy, S. H. Y., Grisotto, M., Renia, L., Conway, S. J., Stanley, E. R., Chan, J. K. Y., Ng, L. G., Samokhvalov, I. M., Merad, M. & Ginhoux, F. Adult Langerhans cells derive predominantly from embryonic fetal liver monocytes with a minor contribution of yolk sac–derived macrophages. *The Journal of Experimental Medicine* **209,** 1167–1181 (May 2012).

11. Pace, J. L., Russell, S. W., Schreiber, R. D., Altman, A. & Katz, D. H. Macrophage activation: priming activity from a T-cell hybridoma is attributable to interferon-gamma. *Proceedings of the National Academy of Sciences* **80,** 3782–3786 (June 1983).

12. Nathan, C. F., Murray, H. W., Wiebe, M. E. & Rubin, B. Y. Identification of interferon-gamma as the lymphokine that activates human macrophage oxidative metabolism and antimicrobial activity. *The Journal of Experimental Medicine* **158,** 670–689 (Sept. 1983).

13. Stein, M., Keshav, S., Harris, N. & Gordon, S. Interleukin 4 potently enhances murine macrophage mannose receptor activity: a marker of alternative immunologic macrophage activation. *The Journal of Experimental Medicine* **176,** 287–292 (July 1992).

14. Doyle, A. G., Herbein, G., Montaner, L. J., Minty, A. J., Caput, D., Ferrara, P. & Gordon, S. Interleukin-13 alters the activation state of murine macrophagesin vitro: Comparison with interleukin-4 and interferon-γ. *European Journal of Immunology* **24,** 1441–1445 (June 1994).

15. Chen, Z., Hagler, J., Palombella, V. J., Melandri, F., Scherer, D., Ballard, D. & Maniatis, T. Signal-induced site-specific phosphorylation targets I kappa B alpha

to the ubiquitin-proteasome pathway. *Genes & Development* **9,** 1586–1597 (July 1995).

16. Chen, Z. J., Parent, L. & Maniatis, T. Site-Specific Phosphorylation of IκBα by a Novel Ubiquitination-Dependent Protein Kinase Activity. *Cell* **84,** 853–862 (Mar. 1996).

17. Darnell, J., Kerr, I. & Stark, G. Jak-STAT pathways and transcriptional activation in response to IFNs and other extracellular signaling proteins. *Science* **264,** 1415–1421 (June 1994).

18. Shuai, K., Ziemiecki, A., Wilks, A. F., Harpur, A. G., Sadowski, H. B., Gilman, M. Z. & Darnell, J. E. Polypeptide signalling to the nucleus through tyrosine phosphorylation of Jak and Stat proteins. *Nature* **366,** 580–583 (Dec. 1993).

19. Bode, J. G., Ehlting, C. & Häussinger, D. The macrophage response towards LPS and its control through the p38MAPK–STAT3 axis. *Cellular Signalling* **24,** 1185–1194 (June 2012).

20. Huang, S. C.-C., Smith, A. M., Everts, B., Colonna, M., Pearce, E. L., Schilling, J. D. & Pearce, E. J. Metabolic Reprogramming Mediated by the mTORC2-IRF4 Signaling Axis Is Essential for Macrophage Alternative Activation. *Immunity* **45,** 817–830 (Oct. 2016).

21. Von Knethen, A., Callsen, D. & Brüne, B. NF-κB and AP-1 Activation by Nitric Oxide Attenuated Apoptotic Cell Death in RAW 264.7 Macrophages. *Molecular Biology of the Cell* **10** (ed Raff, M.) 361–372 (Feb. 1999).

22. Mantovani, A., Biswas, S. K., Galdiero, M. R., Sica, A. & Locati, M. Macrophage plasticity and polarization in tissue repair and remodelling. *The Journal of Pathology* **229,** 176–185 (Nov. 2012).

23. De Groot, A. E. & Pienta, K. J. Epigenetic control of macrophage polarization: implications for targeting tumor-associated macrophages. *Oncotarget* **9.** doi:10.18632/oncotarget.24556 (Feb. 2018).

24. Corliss, B. A., Azimi, M. S., Munson, J. M., Peirce, S. M. & Murfee, W. L. Macrophages: An Inflammatory Link Between Angiogenesis and Lymphangiogenesis. *Microcirculation* **23,** 95–121 (Feb. 2016).

25. Rőszer, T. Understanding the Mysterious M2 Macrophage through Activation Markers and Effector Mechanisms. *Mediators of Inflammation* **2015,** 1–16 (2015).

26. Murray, P. J., Allen, J. E., Biswas, S. K., Fisher, E. A., Gilroy, D. W., Goerdt, S., Gordon, S., Hamilton, J. A., Ivashkiv, L. B., Lawrence, T., Locati, M., Mantovani, A., Martinez, F. O., Mege, J.-L., Mosser, D. M., Natoli, G., Saeij, J. P., Schultze, J. L., Shirey, K. A., Sica, A., Suttles, J., Udalova, I., van Ginderachter, J. A., Vogel, S. N. & Wynn, T. A. Macrophage Activation and Polarization: Nomenclature and Experimental Guidelines. *Immunity* **41,** 14–20 (July 2014).

27. Den Bossche, J. V., O'Neill, L. A. & Menon, D. Macrophage Immunometabolism: Where Are We (Going)? *Trends in Immunology* **38,** 395–406 (June 2017).

28. Freemerman, A. J., Johnson, A. R., Sacks, G. N., Milner, J. J., Kirk, E. L., Troester, M. A., Macintyre, A. N., Goraksha-Hicks, P., Rathmell, J. C. & Makowski, L. Metabolic Reprogramming of Macrophages. *Journal of Biological Chemistry* **289,** 7884–7896 (Feb. 2014).

29. KEGG. *Carbon metabolism* <https://www.genome.jp/kegg-bin/show_pathway?map=map01200&show_description=show>.

30. Loeffler, G., Petrides, P. & Heinrich, P. *Biochemie & Pathobiochemie* 8th ed. ISBN: 9783540326809 (Springer, 2006).

31. Garaude, J., Acín-Pérez, R., Martínez-Cano, S., Enamorado, M., Ugolini, M., Nistal-Villán, E., Hervás-Stubbs, S., Pelegrín, P., Sander, L. E., Enríquez, J. A. & Sancho, D. Mitochondrial respiratory-chain adaptations in macrophages contribute to antibacterial host defense. *nature immunology.* doi:10.1038/ni.3509 (2016).

32. Tugal, D., Liao, X. & Jain, M. K. Transcriptional Control of Macrophage Polarization. *Arteriosclerosis, Thrombosis, and Vascular Biology* **33,** 1135–1144 (June 2013).

33. Weintz, G., Olsen, J. V., Frühauf, K., Niedzielska, M., Amit, I., Jantsch, J., Mages, J., Frech, C., Doelken, L., Mann, M. & Lang, R. The phosphoproteome of toll-like receptor-activated macrophages. *Molecular Systems Biology* **6,** 371 (Jan. 2010).

34. Rius, J., Guma, M., Schachtrup, C., Akassoglou, K., Zinkernagel, A. S., Nizet, V., Johnson, R. S., Haddad, G. G. & Karin, M. NF-κB links innate immunity to the hypoxic response through transcriptional regulation of HIF-1α. *Nature* **453,** 807–811 (Apr. 2008).

35. Blouin, C. C., Page, E. L., Soucy, G. M. & Richard, D. E. Hypoxic gene activation by lipopolysaccharide in macrophages: implication of hypoxia-inducible factor 1α. *Blood* **103,** 1124–1130 (Feb. 2004).

36. Wang, T., Liu, H., Lian, G., Zhang, S.-Y., Wang, X. & Jiang, C. HIF1α-Induced Glycolysis Metabolism Is Essential to the Activation of Inflammatory Macrophages. *Mediators of Inflammation* **2017,** 1–10 (2017).

37. Van Uden, P., Kenneth, N. S. & Rocha, S. Regulation of hypoxia-inducible factor-1α by NF-κB. *Biochemical Journal* **412,** 477–484 (May 2008).

38. Semenza, G. L., Jiang, B.-H., Leung, S. W., Passantino, R., Concordet, J.-P., Maire, P. & Giallongo, A. Hypoxia Response Elements in the Aldolase A, Enolase 1, and Lactate Dehydrogenase A Gene Promoters Contain Essential Binding Sites for Hypoxia-inducible Factor 1. *Journal of Biological Chemistry* **271,** 32529–32537 (Dec. 1996).

39. Kim, J.-w., Tchernyshyov, I., Semenza, G. L. & Dang, C. V. HIF-1-mediated expression of pyruvate dehydrogenase kinase: A metabolic switch required for cellular adaptation to hypoxia. *Cell Metabolism* **3,** 177–185 (Mar. 2006).

40. Palsson-McDermott, E. M., Curtis, A. M., Goel, G., Lauterbach, M. A. R., Sheedy, F. J., Gleeson, L. E., van den Bosch, M. W. M., Quinn, S. R., Domingo-Fernandez, R., Johnston, D. G. W., Jiang, J.-k., Israelsen, W. J., Keane, J., Thomas, C., Clish, C., Heiden, M. V., Xavier, R. J. & O'Neill, L. A. J. Pyruvate Kinase M2 Regulates Hif-1α Activity and IL-1β Induction and Is a Critical Determinant of the Warburg Effect in LPS-Activated Macrophages. *Cell Metabolism* **21,** 65–80 (Jan. 2015).

41. Gene Cards The Human Gene Database. *PDK1 Gene* <https://www.genecards.org/cgi-bin/carddisp.pl?gene=PDK1>.

42. Mills, E. L., Kelly, B. & ONeill, L. A. J. Mitochondria are the powerhouses of immunity. *Nature Immunology* **18,** 488–498 (May 2017).

43. Tan, Z., Xie, N., Cui, H., Moellering, D. R., Abraham, E., Thannickal, V. J. & Liu, G. Pyruvate Dehydrogenase Kinase 1 Participates in Macrophage Polarization via Regulating Glucose Metabolism. *The Journal of Immunology* **194,** 6082–6089 (May 2015).

44. Huang, S. C.-C., Everts, B., Ivanova, Y., O'Sullivan, D., Nascimento, M., Smith, A. M., Beatty, W., Love-Gregory, L., Wing Y. Lam, W. Y., O'Neill, C. M., Yan, C., Du, H., Abumrad, N. A., Urban Jr, J. F., Artyomov, M. N., Pearce, E. L. & Pearce, E. J. Cell-intrinsic lysosomal lipolysis is essential for alternative activation of macrophages. *nature immunology.* doi:10.1038/ni.2956 (2014).

45. Wang, F., Zhang, S., Vuckovic, I., Jeon, R., Lerman, A., Folmes, C. D., Dzeja, P. P. & Herrmann, J. Glycolytic Stimulation Is Not a Requirement for M2 Macrophage Differentiation. *Cell Metabolism* **28,** 463–475.e4 (Sept. 2018).

46. Rich, P. The molecular machinery of Keilin's respiratory chain. *Biochemical Society Transactions* **31,** 1095–1105 (Dec. 2003).

47. Zhao, R., Jiang, S., Zhang, L. & Yu, Z. Mitochondrial electron transport chain, ROS generation and uncoupling (Review). *International Journal of Molecular Medicine.* doi:10.3892/ijmm.2019.4188. <https://doi.org/10.3892/ijmm.2019.4188> (May 2019).

48. Venter, G., Oerlemans, F. T. J. J., Wijers, M., Willemse, M., Fransen, J. A. M. & Wieringa, B. Glucose Controls Morphodynamics of LPS-Stimulated Macrophages. *PLoS ONE* **9** (ed Singh, P. K.) e96786 (May 2014).

49. Bulua, A. C., Simon, A., Maddipati, R., Pelletier, M., Park, H., Kim, K.-Y., Sack, M. N., Kastner, D. L. & Siegel, R. M. Mitochondrial reactive oxygen species promote production of proinflammatory cytokines and are elevated in TNFR1-

associated periodic syndrome (TRAPS). *The Journal of Experimental Medicine* **208,** 519–533 (Jan. 2011).

50. Kietzmann, T. & Görlach, A. Reactive oxygen species in the control of hypoxia-inducible factor-mediated gene expression. *Seminars in Cell & Developmental Biology* **16,** 474–486 (Aug. 2005).

51. Williams, N. C. & O'Neill, L. A. J. A Role for the Krebs Cycle Intermediate Citrate in Metabolic Reprogramming in Innate Immunity and Inflammation. *Frontiers in Immunology* **9.** doi:10.3389/fimmu.2018.00141 (Feb. 2018).

52. Infantino, V., Iacobazzi, V., Menga, A., Avantaggiati, M. L. & Palmieri, F. A key role of the mitochondrial citrate carrier (SLC25A1) in TNFα- and IFNγ-triggered inflammation. *Biochimica et Biophysica Acta (BBA) - Gene Regulatory Mechanisms* **1839,** 1217–1225 (Nov. 2014).

53. Infantino, V., Iacobazzi, V., Palmieri, F. & Menga, A. ATP-citrate lyase is essential for macrophage inflammatory response. *Biochemical and Biophysical Research Communications* **440,** 105–111 (Oct. 2013).

54. Infantino, V., Convertini, P., Cucci, L., Panaro, M. A., Noia, M. A. D., Calvello, R., Palmieri, F. & Iacobazzi, V. The mitochondrial citrate carrier: a new player in inflammation. *Biochemical Journal* **438,** 433–436 (Aug. 2011).

55. Wellen, K. E., Hatzivassiliou, G., Sachdeva, U. M., Bui, T. V., Cross, J. R. & Thompson, C. B. ATP-Citrate Lyase Links Cellular Metabolism to Histone Acetylation. *Science* **324,** 1076–1080 (May 2009).

56. Wang, Q., Zhang, Y., Yang, C., Xiong, H., Lin, Y., Yao, J., Li, H., Xie, L., Zhao, W., Yao, Y., Ning, Z.-B., Zeng, R., Xiong, Y., Guan, K.-L., Zhao, S. & Zhao, G.-P. Acetylation of Metabolic Enzymes Coordinates Carbon Source Utilization and Metabolic Flux. *Science* **327,** 1004–1007 (Feb. 2010).

57. Michelucci, A., Cordes, T., Ghelfi, J., Pailot, A., Reiling, N., Goldmann, O., Binz, T., Wegner, A., Tallam, A., Rausell, A., Buttini, M., Linster, C. L., Medina, E., Balling, R. & Hiller, K. Immune-responsive gene 1 protein links metabolism to immunity

by catalyzing itaconic acid production. *Proceedings of the National Academy of Sciences* **110,** 7820–7825 (Apr. 2013).

58. McFadden, B. & Purohit, S. Itaconate, an isocitrate lyase-directed inhibitor in Pseudomonas indigofera. *Journal of Bacteriology* (1977).

59. Lampropoulou, V., Sergushichev, A., Bambouskova, M., Nair, S., Vincent, E. E., Loginicheva, E., Cervantes-Barragan, L., Ma, X., Huang, S. C.-C., Griss, T., Weinheimer, C. J., Khader, S., Randolph, G. J., Pearce, E. J., Jones, R. G., Diwan, A., Diamond, M. S. & Artyomov, M. N. Itaconate Links Inhibition of Succinate Dehydrogenase with Macrophage Metabolic Remodeling and Regulation of Inflammation. *Cell Metabolism* **24,** 158–166 (July 2016).

60. Palmieri, F. The mitochondrial transporter family (SLC25): physiological and pathological implications. *Pfligers Archiv European Journal of Physiology* **447,** 689–709 (Feb. 2004).

61. Tannahill, G. M., Curtis, A. M., Adamik, J., Palsson-McDermott, E. M., McGettrick, A. F., Goel, G., Frezza, C., Bernard, N. J., Kelly, B., Foley, N. H., Zheng, L., Gardet, A., Tong, Z., Jany, S. S., Corr, S. C., Haneklaus, M., Caffrey, B. E., Pierce, K., Walmsley, S., Beasley, F. C., Cummins, E., Nizet, V., Whyte, M., Taylor, C. T., Lin, H., Masters, S. L., Gottlieb, E., Kelly, V. P., Clish, C., Auron, P. E., Xavier, R. J. & O'Neill, L. A. J. Succinate is an inflammatory signal that induces IL-1β through HIF-1α. *Nature* **496,** 238–242 (Mar. 2013).

62. Rubic, T., Lametschwandtner, G., Jost, S., Hinteregger, S., Kund, J., Carballido-Perrig, N., Schwärzler, C., Junt, T., Voshol, H., Meingassner, J. G., Mao, X., Werner, G., Rot, A. & Carballido, J. M. Triggering the succinate receptor GPR91 on dendritic cells enhances immunity. *Nature Immunology* **9,** 1261–1269 (Sept. 2008).

63. Littlewood-Evans, A., Sarret, S., Apfel, V., Loesle, P., Dawson, J., Zhang, J., Muller, A., Tigani, B., Kneuer, R., Patel, S., Valeaux, S., Gommermann, N., Rubic-Schneider, T., Junt, T. & Carballido, J. M. GPR91 senses extracellular succinate released from inflammatory macrophages and exacerbates rheumatoid arthritis. *The Journal of Experimental Medicine* **213,** 1655–1662 (Aug. 2016).

64. Mills, E. L., Kelly, B., Logan, A., Costa, A. S. H., Varma, M., Bryant, C. E., Tourlomousis, P., Däbritz, J. H. M., Gottlieb, E., Latorre, I., Corr, S. C., McManus, G., Ryan, D., Jacobs, H. T., Szibor, M., Xavier, R. J., Braun, T., Frezza, C., Murphy, M. P. & O'Neill, L. A. Succinate Dehydrogenase Supports Metabolic Repurposing of Mitochondria to Drive Inflammatory Macrophages. *Cell* **167,** 457–470.e13 (Oct. 2016).

65. Covarrubias, A. J., Aksoylar, H. I., Jiujiu, Y., Snyder, N. W., Worth, A. J., Iyer, S. S., Wang, J., Ben-Sahra, I., Byles, V., Polynne-Stapornkul, T., Espinosa, E. C., Lamming, D., Manning, B. D., Zhang, Y., Blair, I. A. & Horng, T. Akt-mTORC1 signaling regulates Acly to integrate metabolic input to control of macrophage activation. *eLIFE*. doi:DOI:10.7554/eLife.11612.001 (2016).

66. Gordon, S. & Martinez, F. O. Alternative Activation of Macrophages: Mechanism and Functions. *Immunity* **32,** 593–604 (May 2010).

67. Martinez, F. O., Helming, L. & Gordon, S. Alternative Activation of Macrophages: An Immunologic Functional Perspective. *Annual Review of Immunology* **27,** 451–483 (Apr. 2009).

68. Takeda, K., Tanaka, T., Shi, W., Matsumoto, M., Minami, M., Kashiwamura, S.-i., Nakanishi, K., Yoshida, N., Kishimoto, T. & Akira, S. Essential role of Stat6 in IL-4 signalling. *Nature* **380,** 627–630 (Apr. 1996).

69. Varin, A. & Gordon, S. Alternative activation of macrophages: Immune function and cellular biology. *Immunobiology* **214,** 630–641 (July 2009).

70. Odegaard, J. I., Ricardo-Gonzalez, R. R., Goforth, M. H., Morel, C. R., Subramanian, V., Mukundan, L., Eagle, A. R., Vats, D., Brombacher, F., Ferrante, A. W. & Chawla, A. Macrophage-specific PPARγ controls alternative activation and improves insulin resistance. *Nature* **447,** 1116–1120 (May 2007).

71. J, T. The major electrolytes: sodium, potassium, and chloride. *J Intraven Nurs.* **17(5),** 240–7 (1994).

72. Lang, F. in *Nestlé Nutrition Institute Workshop Series* 115–130 (KARGER, 2012). doi:10.1159/000329290. <https://doi.org/10.1159/000329290>.

73. Titze, J. Sodium balance is not just a renal affair. *Current Opinion in Nephrology and Hypertension* **23,** 101–105 (Mar. 2014).

74. Rakova, N., Jüttner, K., Dahlmann, A., Schröder, A., Linz, P., Kopp, C., Rauh, M., Goller, U., Beck, L., Agureev, A., Vassilieva, G., Lenkova, L., Johannes, B., Wabel, P., Moissl, U., Vienken, J., Gerzer, R., Eckardt, K.-U., Müller, D., Kirsch, K., Morukov, B., Luft, F. & Titze, J. Long-Term Space Flight Simulation Reveals Infradian Rhythmicity in Human Na+ Balance. *Cell Metabolism* **17,** 125–131 (Jan. 2013).

75. Titze, J., Maillet, A., Lang, R., Gunga, H. C., Johannes, B., Gauquelin-Koch, G., Kihm, E., Larina, I., Gharib, C. & Kirsch, K. A. Long-term sodium balance in humans in a terrestrial space station simulation study. *American Journal of Kidney Diseases* **40,** 508–516 (Sept. 2002).

76. Inglese, M., Madelin, G., Oesingmann, N., Babb, J. S., Wu, W., Stoeckel, B., Herbert, J. & Johnson, G. Brain tissue sodium concentration in multiple sclerosis: a sodium imaging study at 3 tesla. *Brain* **133,** 847–857 (Jan. 2010).

77. Petracca, M., Vancea, R. O., Fleysher, L., Jonkman, L. E., Oesingmann, N. & Inglese, M. Brain intra- and extracellular sodium concentration in multiple sclerosis: a 7 T MRI study. *Brain* **139,** 795–806 (Jan. 2016).

78. Kopp, C., Linz, P., Wachsmuth, L., Dahlmann, A., Horbach, T., Schöfl, C., Renz, W., Santoro, D., Niendorf, T., Müller, D. N., Neininger, M., Cavallaro, A., Eckardt, K.-U., Schmieder, R. E., Luft, F. C., Uder, M. & Titze, J. 23 Na Magnetic Resonance Imaging of Tissue Sodium. *Hypertension* **59,** 167–172 (Jan. 2012).

79. Kopp, C., Linz, P., Dahlmann, A., Hammon, M., Jantsch, J., Müller, D. N., Schmieder, R. E., Cavallaro, A., Eckardt, K.-U., Uder, M., Luft, F. C. & Titze, J. 23 Na Magnetic Resonance Imaging-Determined Tissue Sodium in Healthy Subjects and Hypertensive Patients. *Hypertension* **61,** 635–640 (Mar. 2013).

80. Jantsch, J., Schatz, V., Friedrich, D., Schroder, A., Kopp, C., Siegert, I., Maronna, A., Wendelborn, D., Linz, P., Binger, K. J., Gebhardt, M., Heinig, M., Neubert, P., Fischer, F., Teufel, S., David, J.-P., Neufert, C., Cavallaro, A., Rakova, N., Kuper, C., Beck, F.-X., Neuhofer, W., Muller, D. N., Schuler, G., Uder, M., Bogdan, C.,

Luft, F. C. & Titze, J. Cutaneous Na+ storage strengthens the antimicrobial barrier function of the skin and boosts macrophage-driven host defense. eng. *Cell metabolism* **21,** 493–501 (3 Mar. 2015).

81. Huhn, K., Mennecke, A., Linz, P., Tschunko, F., Kästle, N., Nagel, A. M., Uder, M., Dörfler, A., Linker, R. A. & Engelhorn, T. 23 Na MRI reveals persistent sodium accumulation in tumefactive MS lesions. *Journal of the Neurological Sciences* **379,** 163–166 (Aug. 2017).

82. Kleinewietfeld, M., Manzel, A., Titze, J., Kvakan, H., Yosef, N., Linker, R. A., Muller, D. N. & Hafler, D. A. Sodium chloride drives autoimmune disease by the induction of pathogenic TH17 cells. *Nature Letter* **496,** 518–522 (Mar. 2013).

83. Dar, H. Y., Singh, A., Shukla, P., Anupam, R., Mondal, R. K., Mishra, P. K. & Srivastava, R. K. High dietary salt intake correlates with modulated Th17-Treg cell balance resulting in enhanced bone loss and impaired bone-microarchitecture in male mice. *Scientific Reports* **8.** doi:10.1038/s41598-018-20896-y. <https://doi.org/10.1038/s41598-018-20896-y> (Feb. 2018).

84. Matthias, J., Maul, J., Noster, R., Meinl, H., Chao, Y.-Y., Gerstenberg, H., Jeschke, F., Gasparoni, G., Welle, A., Walter, J., Nordström, K., Eberhardt, K., Renisch, D., Donakonda, S., Knolle, P., Soll, D., Grabbe, S., Garzorz-Stark, N., Eyerich, K., Biedermann, T., Baumjohann, D. & Zielinski, C. E. Sodium chloride is an ionic checkpoint for human TH2 cells and shapes the atopic skin microenvironment. *Science Translational Medicine* **11,** eaau0683 (Feb. 2019).

85. Hernandez, A. L., Kitz, A., Wu, C., Lowther, D. E., Rodriguez, D. M., Vudattu, N., Deng, S., Herold, K. C., Kuchroo, V. K., Kleinewietfeld, M. & Hafler, D. A. Sodium chloride inhibits the suppressive function of FOXP3^{+} regulatory T cells. *Journal of Clinical Investigation* **125,** 4212–4222 (Oct. 2015).

86. Neubert, P., Weichselbaum, A., Reitinger, C., Schatz, V., Schröder, A., Ferdinand, J. R., Simon, M., Bär, A.-L., Brochhausen, C., Gerlach, R. G., Tomiuk, S., Hammer, K., Wagner, S., van Zandbergen, G., Binger, K. J., Müller, D. N., Kitada, K., Clatworthy, M. R., Kurts, C., Titze, J., Abdullah, Z. & Jantsch, J. HIF1A and

NFAT5 coordinate Na^+-boosted antibacterial defense via enhanced autophagy and autolysosomal targeting. *Autophagy* **15,** 1899–1916 (Apr. 2019).

87. Binger, K. J., Gebhardt, M., Heinig, M., Rintisch, C., Schroeder, A., Neuhofer, W., Hilgers, K., Manzel, A., Schwartz, C., Kleinewietfeld, M., Voelkl, J., Schatz, V., Linker, R. A., Lang, F., Voehringer, D., Wright, M. D., Hubner, N., Dechend, R., Jantsch, J., Titze, J. & Müller, D. N. High salt reduces the activation of IL-4– and IL-13–stimulated macrophages. *Journal of Clinical Investigation* **125,** 4223–4238 (Oct. 2015).

88. Marko, L., Kvakan, H., Park, J.-K., Qadri, F., Spallek, B., Binger, K. J., Bowman, E. P., Kleinewietfeld, M., Fokuhl, V., Dechend, R. & Muller, D. N. Interferon-gamma signaling inhibition ameliorates angiotensin II-induced cardiac damage. eng. *Hypertension (Dallas, Tex. : 1979)* **60,** 1430–6 (6 Dec. 2012).

89. Kuich, P. H. J. L., Hoffmann, N. & Kempa, S. Maui-VIA: A User-Friendly Software for Visual Identification, Alignment, Correction, and Quantification of Gas Chromatography-Mass Spectrometry Data. *Frontiers in Bioengineering and Biotechnology* **2.** doi:10.3389/fbioe.2014.00084 (Jan. 2015).

90. Zasada, C. *Experimental and mathematical analysis of the central carbon metabolism in cancer and stem cells* Dissertation (Lebenswissenschaftliche Fakultät der Humboldt-Universität zu Berlin, 2017). doi:10.18452/18309.

91. Youle, R. J. & van der Bliek, A. M. Mitochondrial Fission, Fusion, and Stress. *Science* **337,** 1062–1065 (Aug. 2012).

92. Buck, M., O'Sullivan, D., Klein Geltink, R., Curtis, J., Chang, C.-H., Sanin, D., Qiu, J., Kretz, O., Braas, D., van der Windt, G., Chen, Q., Huang, S.-C., O'Neill, C., Edelson, B., Pearce, E., Sesaki, H., Huber, T., Rambold, A. & Pearce, E. Mitochondrial Dynamics Controls T Cell Fate through Metabolic Programming. *Cell* **166,** 63–76 (June 2016).

93. Dos Anjos Cassado, A., Lima, M. R. D. & Bortoluci, K. R. Revisiting Mouse Peritoneal Macrophages: Heterogeneity, Development, and Function. *Frontiers in Immunology* **6.** doi:10.3389/fimmu.2015.00225 (May 2015).

94. Ghosn, E. E. B., Cassado, A. A., Govoni, G. R., Fukuhara, T., Yang, Y., Monack, D. M., Bortoluci, K. R., Almeida, S. R., Herzenberg, L. A. & Herzenberg, L. A. Two physically, functionally, and developmentally distinct peritoneal macrophage subsets. *Proceedings of the National Academy of Sciences* **107,** 2568–2573 (Jan. 2010).

95. Ip, W. K. E. & Medzhitov, R. Macrophages monitor tissue osmolarity and induce inflammatory response through NLRP3 and NLRC4 inflammasome activation. *Nature Communications* **6.** doi:10.1038/ncomms7931. <https://doi.org/10.1038/ncomms7931> (May 2015).

96. Sanin, D. E., Matsushita, M., Geltink, R. I. K., Grzes, K. M., van Teijlingen Bakker, N., Corrado, M., Kabat, A. M., Buck, M. D., Qiu, J., Lawless, S. J., Cameron, A. M., Villa, M., Baixauli, F., Patterson, A. E., Hässler, F., Curtis, J. D., O'Neill, C. M., O'Sullivan, D., Wu, D., Mittler, G., Huang, S. C.-C., Pearce, E. L. & Pearce, E. J. Mitochondrial Membrane Potential Regulates Nuclear Gene Expression in Macrophages Exposed to Prostaglandin E2. *Immunity* **49,** 1021–1033.e6 (Dec. 2018).

97. Shu-Na, C., Jing, Q. & Ping, B. Effect of mitochondrial complex III inhibitor antimycin A on immune function of macrophages. *CJPT* **29,** 573–577 (4 2015).

98. Suckling, R. J., He, F. J., Markandu, N. D. & MacGregor, G. A. Dietary salt influences postprandial plasma sodium concentration and systolic blood pressure. *Kidney International*. doi:10.1038/ki.2011.369 (2012).

99. Dickinson, K. M., Clifton, P. M., Burrell, L. M., Barrett, P. H. R. & Keogh, J. B. Postprandial effects of a high salt meal on serum sodium, arterial stiffness, markers of nitric oxide production and markers of endothelial function. *Atherosclerosis* **232,** 211–216 (Jan. 2014).

100. Yi, B., Titze, J., Rykova, M., Feuerecker, M., Vassilieva, G., Nichiporuk, I., Schelling, G., Morukov, B. & Choukèr, A. Effects of dietary salt levels on monocytic cells and immune responses in healthy human subjects: a longitudinal study. *Translational Research* **166,** 103–110 (July 2015).

101. Iwai, T., Tanonaka, K., Inoue, R., Kasahara, S., Motegi, K., Nagaya, S. & Takeo, S. Sodium accumulation during ischemia induces mitochondrial damage in perfused rat hearts. *Cardiovascular Research* (2001).

102. Tanonaka, K., Motegi, K., Arino, T., Marunouchi, T., Takagi, N. & Takeo, S. Possible Pathway of Na Flux into Mitochondria in Ischemic Heart. *Biological and Pharmaceutical Bulletin* (2012).

103. Cordain, L., Eaton, S. B., Sebastian, A., Mann, N., Lindeberg, S., Watkins, B. A., O'Keefe, J. H. & Brand-Miller, J. Origins and evolution of the Western diet: health implications for the 21st century. *The American Journal of Clinical Nutrition* **81,** 341–354 (Feb. 2005).

104. Oberleithner, H., Riethmuller, C., Schillers, H., MacGregor, G. A., de Wardener, H. E. & Hausberg, M. Plasma sodium stiffens vascular endothelium and reduces nitric oxide release. *Proceedings of the National Academy of Sciences* **104,** 16281–16286 (Oct. 2007).

105. Dmitrieva, N. I. & Burg, M. B. Elevated Sodium and Dehydration Stimulate Inflammatory Signaling in Endothelial Cells and Promote Atherosclerosis. *PLOS ONE* **10** (ed Norata, G. D.) e0128870 (June 2015).

106. Oberleithner, H., Kusche-Vihrog, K. & Schillers, H. Endothelial cells as vascular salt sensors. *Kidney International.* doi:10.1038/ki.2009.490 (2017).

107. Rambold, A. S. & Lippincott-Schwartz, J. Mechanisms of mitochondria and autophagy crosstalk. *Cell Cycle* **10,** 4032–4038 (Dec. 2011).

108. Egan, D., Kim, J., Shaw, R. J. & Guan, K.-L. The autophagy initiating kinase ULK1 is regulated via opposing phosphorylation by AMPK and mTOR. *Autophagy* **7,** 643–644 (June 2011).

109. Egan, D. F., Shackelford, D. B., Mihaylova, M. M., Gelino, S., Kohnz, R. A., Mair, W., Vasquez, D. S., Joshi, A., Gwinn, D. M., Taylor, R., Asara, J. M., Fitzpatrick, J., Dillin, A., Viollet, B., Kundu, M., Hansen, M. & Shaw, R. J. Phosphorylation of ULK1 (hATG1) by AMP-Activated Protein Kinase Connects Energy Sensing to Mitophagy. *Science* **331,** 456–461 (Dec. 2010).

110. Kim, J., Kundu, M., Viollet, B. & Guan, K.-L. AMPK and mTOR regulate autophagy through direct phosphorylation of Ulk1. *Nature Cell Biology* **13,** 132–141 (Jan. 2011).

111. Shang, L., Chen, S., Du, F., Li, S., Zhao, L. & Wang, X. Nutrient starvation elicits an acute autophagic response mediated by Ulk1 dephosphorylation and its subsequent dissociation from AMPK. *Proceedings of the National Academy of Sciences* **108,** 4788–4793 (Mar. 2011).

112. Hailey, D. W., Rambold, A. S., Satpute-Krishnan, P., Mitra, K., Sougrat, R., Kim, P. K. & Lippincott-Schwartz, J. Mitochondria Supply Membranes for Autophagosome Biogenesis during Starvation. *Cell* **141,** 656–667 (May 2010).

113. Strappazzon, F., Vietri-Rudan, M., Campello, S., Nazio, F., Florenzano, F., Fimia, G. M., Piacentini, M., Levine, B. & Cecconi, F. Mitochondrial BCL-2 inhibits AMBRA1-induced autophagy. *The EMBO Journal* **30,** 1195–1208 (Feb. 2011).

Declaration

Herewith, I declare

Ich erkläre hiermit, dass ich

- to have completed this Dissertation autonomously and without any ilegitimate means,

  die eingereichte Dissertation selbständig und ohne unerlaubte Hilfsmittel angefertigt habe,

- to have given due acknowledgement to material obtained from references, designating the version (edition and year of publication), and to have not used any other references or means besides the ones indicated in the bibliography,

  außer den im Schrifttumsverzeichnis angegebenen Quellen und Hilfsmitteln keine weiteren benutzt und alle Stellen, die aus dem Schrifttum ganz oder annähernd entnommen sind, als solche kenntlich gemacht und einzeln nach ihrer Herkunft unter Bezeichnung der Ausgabe (Auflage und Jahr des Erscheinens) des benützten Werkes nachgewiesen habe,

- to have not submitted this Dissertation elsewhere and that it has not served - neither entirely nor partially - any other functions.

  die Dissertation noch keiner anderen Stelle zur Prüfung vorgelegt habe und dass dieselbe noch nicht anderen Zwecken - auch nicht teilweise - gedient hat.

Berlin, 14.01.2020

Sabrina Yasmin Geisberger

Curriculum vitae

This section has been removed for publication.